STUDY ON LITHIUM INSERTION COMPOUNDS AS ELECTRODE MATERIALS FOR LITHIUM SECONDARY BATTERY

1992

NOBUYUKI IMANISHI

Contents

	Page
General Introduction	1
Part I. Cathodic Reaction Mechanisms of Lithium Insertion Compounds	13
Chapter 1. Lithium Diffusion Behaviors in MoS_2 Thin Film Electrode Prepared by CVD Method	13
1.1 Introduction	13
1.2 Experimental	14
1.3 Results and Discussion	17
Chapter 2. Effect of Electrolyte Solvents on Lithium Intercalation into MoS_2	34
2.1 Introduction	34
2.2 Experimental	35
2.3 Results and Discussion	37
2.4 Conclusion	49
Chapter 3. Characteristics of Modified FeOCl Containing Organic Compounds in the Interlayer Space	51
3.1 Introduction	51
3.2 Experimental	51
3.3 Results and Discussion	53

Chapter 4. Characteristics of Defect Thiospinel Compounds Having Three Dimensional Lithium Diffusion Paths 64
4.1 Introduction 64
4.2 Experimental 65
4.3 Results and Discussion 66

Chapter 5. Characteristics of Brannerite-Type $CuV_{2-x}Mo_xO_6$ (0<x<1) Cathodes 77
5.1 Introduction 77
5.2 Experimental 80
5.3 Results and Discussion 81
5.3.1 Relationship between structural characteristics and discharge-charge processes 81
5.3.2 The Li/$CuV_{2-x}Mo_xO_6$ cell performances 90

Part II. Anodic Reaction Mechanisms of Carbon Materials 97

Chapter 1. Carbon-Lithium Composite Anode for Lithium Secondary Battery 97
1.1 Introduction 97
1.2 Experimental 98
1.3 Results and Discussion 99

Chapter 2. Reaction Mechanisms of Lithium and PAN-Based Carbon Fiber 109

2.1 Introduction 109
2.2 Experimental 111
2.3 Results and Discussion 114
2.3.1 Charge-discharge properties of the Li/carbon fiber M46 cells using the solvents with various PC/DME ratios 114
2.3.2 Reaction mechanism of the carbon fiber electrodes using the solvent PC/DME=50/50 120
2.3.3 Lithium-carbon fiber composite anode 130
2.4 Conclusion 135

Chapter 3. Effect of Microtextures of Carbon Materials on Charge-Discharge Characteristics for Mesophase-Pitch-Based Carbon Fiber 140
3.1 Introduction 140
3.2 Experimental 142
3.3 Results and Discussion 146
3.4 Conclusion 158

General Conclusion 161

Acknowledgments 167

General Introduction

The smaller and thinner battery has been strongly required with the development of portable devices over the past 20 years. The lithium battery has been one of the most hopeful candidates, because of its high energy density and high output potential. Therefore, enormous researches on the lithium primary(not rechargeable) battery have been carried out since later in 1960's in the world, and various types of primary batteries have been widely used in small audio-visual devices today. The representatives of these batteries are the combinations of $Li/(CF)_n$(in 1973) and Li/MnO_2(in 1975), whose output potential and energy density are 2.8 V, 220Whkg^{-1} and 3.0 V, 150 Whkg^{-1}, respectively. However, for the use in higher loads or to avoid the frequent exchange of the battery, the rechargeable lithium battery has been strongly desired. From this standpoint, battery researchers have made considerable efforts to search for rechargeable electrode materials. However, even at the present day, the lead-acid battery and Ni-Cd battery are only practically used, and the lithium secondary(rechargeable) battery is on the way of developing. In general, many problems should be solved to realize the lithium secondary battery system compared to the primary battery system.

The lithium secondary battery consist of lithium metal anode, organic solvent containing lithium salt as electrolyte, and various cathode materials. In order to realize the secondary battery, it is important to find good cathode materials, anode

materials, electrolytes, and suitable combinations of these materials. The cathode materials must satisfy the conditions listed below.

1) high reversibility
2) high voltage
3) high energy density
4) high power density
5) safety

The past and present studies have mainly focused on developing the material with high reversibility. The reversibility is directly concerned with the lithium diffusion in the electrode materials, because the most of the electrode reactions bringing the high reversibility is restricted in a case of solid solution formation such as an intercalation reaction. The electrode materials, therefore, must have vacant interstices which facilitate the diffusion of lithium ions and the formation of lithium solid solution by the topochemical reaction without any host structural change. In these respects, the cathode materials having the layered and framework structure characterized by a lot of vacant interstitial sites are specially interesting. Among layered materials, transition metal dichalcogenides, metal oxyhalides, graphite, some kind of oxides, layered silicates, and metal phospho-trisulfides have been examined[1-7]. In 1978, Whittingham used the layered TiS_2 as the reversible cathode material[8]. This material showed lithium intercalation and deintercalation without any destruction of the host structure. In 1987, MoS_2 was applied as the cathode material by Moli Energy

Ltd., and it showed good reversible character[9,10]. This material has some advantages as follows; the initial voltage is higher than that of TiS_2, and the preparation cost is much lower than other compounds. MoS_2 is one of the most promising electrode material among the layered materials.

On the other hand, some materials having two or three dimensional network of vacancies are also interesting. In this field, spinel, ordered rock-salt structure, rutile, ReO_3 type, Chevrel compounds and their related structure have been studied[11-20]. Among them, V_2O_5 has been studied most widely for its high voltage[21-24]. The summary of the electrochemical character of these materials are described in Table 1. As well as these materials, there are many other kind of interesting materials such as defect-type oxides and complex oxides. Some of them have been not yet studied in spite of the hopeful candidates as cathode materials of secondary battery.

In order to develop good cathode materials, it is important not only to select good materials having suitable vacancy, but also to know the reaction mechanism of charge and discharge of lithium in these sulfides or oxides. Especially the structural change induced by the lithium intercalation play an important role on the charge-discharge cycling. These fundamental investigation of lithium insertion into various host structure must be much helpful in order to develop the new cathode materials.

Concerning the anode material, on the other hand, there are only few choices. Because the lithium metal has the lowest redox

Table 1 Electrochemical properties of various cathode materials for lithium secondary battery.

System	cell reaction	Initial voltage (V)	Average voltage (V)	Energy density ($Whkg^{-1}$)
Li/CoO_2	$0.7Li + Li_{0.3}CoO_2 = LiCoO_2$	4.5	4.0	766
Li/PPY	$(C_4H_3N)_n(ClO_4^-)_{0.32}$	3.8	3.0	260
(polypyrrole)	$=(C_4H_3N)_n + 0.32ClO_4^-$			
Li/MnO_2	$0.5Li + MnO_2 = Li_{0.5}MnO_2$	3.5	2.8	415
$Li/a\text{-}V_2O_5$	$1.4Li + a\text{-}Li_{0.6}V_2O_5 = a\text{-}Li_2V_2O_5$	3.6	2.8	541
$Li/c\text{-}V_2O_5$	$Li + c\text{-}V_2O_5 = c\text{-}LiV_2O_5$	3.4	3.2	454
Li/MoV_2O_8	$2Li + LiMoV_2O_8 = Li_3MoV_2O_8$	3.2	2.4	379
Li/V_6O_{13}	$3.6Li + V_6O_{13} = Li_{3.6}V_6O_{13}$	2.8	2.3	412
Li/TiS_2	$Li + TiS_2 = LiTiS_2$	2.7	2.1	473
$Li/NbSe_3$	$3Li + NbSe_3 = Li_3NbSe_3$	2.3	1.9	436
Li/MoS_3	$2Li + a\text{-}LiMoS_3 = a\text{-}Li_3MoS_3$	2.3	1.9	494
Li/MoS_2	$0.8Li + \beta\text{-}Li_{0.2}MoS_2 = \beta\text{-}LiMoS_2$	2.4	1.8	233
$Li/NiPS_3$	$Li + Li_{0.5}NiPS_3 = Li_{1.5}NiPS_3$	2.3	1.8	250

potential(-3.05 vs. NHE) and the highest energy density(4000 $mAhg^{-1}$), it is evident the lithium metal is the best anode material. However, the lithium metal has a significant weak point as the anode for the secondary lithium battery, that is, the side-reaction occurs with electrolyte in the charge process resulting in the prevention of smooth lithium deposition. This phenomenon brings the formation of the extremely active lithium dendrites, which sometimes leads to the short-circuit and ignitions[25,26]. In order to avoid this problem, the selection of the suitable electrolyte, solvent and additives which suppress such phenomenon has been extensively studied[27-29]. The another way is to use the lithium-alloy with other metals[30,31]. After many trials, some kind of carbon materials have found to be outstanding as the anode. The study on the carbon materials as anode showed good reversibility on cycling and no deposition of lithium dendrites[32]. In 1990, Sony Corp. reported the $LiCoO_2$/carbon cell as a practical lithium secondary battery. In this case, the lithium intercalation proceeds on both electrodes, whose system is called as "rocking chair battery"[33]. This was the turning-point to accelerate the studies on the carbon materials. However, the carbon materials have large variety in the texture, structure, crystallinity etc. according to its starting materials and preparation processes, which makes it very difficult to clarify the intercalation mechanisms[34-36]. As in the cathode case, the detailed structural study is much important to find out the best structure of carbon materials.

The aim of this study is to investigate electrochemical lithium intercalation into layered and framework materials as cathode and anode materials. The charge-discharge behaviors for these materials are explained in respect of the starting host structure and structural change on cycling. At the same time, some new oxides are examined as cathode materials. The comparison between three and two-dimensional compounds also gives us some knowledge about the best form of the electrode material of lithium secondary battery. The results from all these studies may lead to get some instructions to produce new electrode materials.

In Part I, cathodic reaction mechanisms of lithium insertion compounds were discussed.

In Chapter 1, the charge-discharge characteristics of 2H-MoS_2 are discussed from the standpoint of a lithium diffusion behavior. In order to investigate the lithium diffusion rate, the cathode system was simplified by using the c-axis oriented MoS_2 thin film prepared by Chemical Vapor Deposition(CVD). The current-time profile in the course of the potentiostatic discharge was measured and a diffusion coefficient could be calculated by assuming the finite one-dimensional diffusion of lithium. The calculated results showed a large increase in a diffusion rate after the phase transformation of the host structure occurred.

In Chapter 2, the effect of electrolyte solvents on a lithium intercalation into 2H-MoS_2 is described. MoS_2 had been

simply believed to transform from 2H to 1T by the lithium intercalation. However, in this study a new Li_xMoS_2 phase having a large expanded c-axis was included in addition to the 1T-Li_xMoS_2 after the discharge of Li/MoS_2 cell. The solvent molecule was found to be co-intercalated with lithium into the interlayer spaces during the first discharge process. The reversibility of the lithium intercalation depended on the kind of the solvent.

In Chapter 3, another type of layered material, FeOCl, is discussed as a cathode material. The lithium intercalated FeOCl is unstable and decomposes into α-Fe, LiCl, and Li_2O during discharge. Therefore FeOCl cannot be used as a cathode material for the lithium secondary battery. However, the stability and discharge characteristics of FeOCl were improved by the intercalation of basic organic compounds.

In Chapter 4, the defect thiospinel compounds, $Cu_xM_2S_4$(M=Ti, Cr) are discussed as a cathode material. In the case of M=Ti, high rate charge-discharging at the current density of more than 1 $mAcm^{-2}$ could be possible, and no solvent intercalation was observed. However, the discharge voltage was not enough high for the use as a cathode material. In the case of M=Cr, the discharge voltage was expected to be higher, but copper ions could not be removed completely from the framework structure. A group of thiospinel compounds show a large variety of characteristics by changing the metal atoms in octahedral sites.

In Chapter 5, structural characteristics and electrochemical behaviors of the brannerite type $CuV_{2-x}Mo_xO_6(0<x<1)$ are discussed

for lithium/$CuV_{2-x}Mo_xO_6$ system. These compounds incorporate Li^+ by expelling copper metal from the lattice on discharge, while Li deintercalation occurs with smooth incorporation of the extracted copper metal into the lattice. Perfect recovery of the crystal structure and crystallinity was observed for Mo rich samples. These cathodes showed fairly large specific capacities and good cycling properties.

In Part II, anodic reaction mechanisms of carbon materials was discussed.

In Chapter 1, the basic behavior of carbon-lithium composite anode is discussed. The PAN-based carbon fiber M46 was mainly investigated as anode, which was proved to be highly reversible in comparison with other carbon materials. Composite anodes of lithium metal and carbon fiber M46 were examined in a cell with Cr_3O_8 cathodes and were found to significantly improve the anode property. From the observation of scanning electron micrographs(SEM), it was shown that the carbon fiber restrains the formation of dendritic lithium metal.

In Chapter 2, the detailed mechanism of charge and discharge of the carbon fiber M46 anodes are described. As shown in chapter 1 of Part II, M46 was found to have high anode performances. The lithium storage mechanism examined by XPS, X-ray diffraction, DTA-TG and electrochemical measurements suggested that the solvated lithium intercalated into the carbon fiber and participated in the highly reversible cell reaction.

In Chapter 3, mesophase-pitch-based carbon fibers heat-

treated at high temperatures(2600 °C or 2800 °C) are studied as anode. Four different types of texture of carbon fibers were used, whose cross-section views are radial texture with wedge(type A), radial texture with fine zig-zag layers(type B), doubly texture(type C), and concentric texture(type D). How carbon texture effects on its cycling performance is discussed. The type A carbon fiber did not show any reversible character even at the first cycle, because the structure of this fiber was destroyed significantly by the lithium intercalation. The other three type of carbon fibers showed good rechargeability. The highest lithium intercalation capacity was observed for the radial oriented carbon fiber(type B).

References

1. M.S.Whittingham, J.Electroanal.Chem., 118, 229(1981).
2. F.A.Trumbore, Pure & Appl.Chem., 52, 119(1979).
3. R.Fong, J.R.Dahn, and C.H.W.Jones, J.Electrochem.Soc., 136, 3206(1989).
4. M.Dohzono, H.Katsuki, and M.Egashira, J.Electrochem.Soc., 136, 1255(1989).
5. T.R.Halbert and J.Scanlon, Mat.Res.Bull., 14, 415(1979).
6. S.Kikkawa, F.Kanamaru, and M.Koizumi, Inorganic Chemistry, 15, 2195(1976).
7. P.G.Dickens and G.J.Reynolds, Solid State Ionics, 5, 331 (1981).

8. M.S.Whittingham, Prog.Solid State Chem., 12, 41(1978).
9. J.A.R.Stiles, New Materials & New Processes, 3, 89(1985).
10. M.A.Py and R.R.Haering, Can.J.Phys., 61, 76(1983).
11. T.Ohzuku, M.Kitagawa, and T.Hirai, J.Electrochem.Soc., 137, 769(1990).
12. M.M.Thackeray, A de Kock, M.Rossouw, and D.Liles, 139, 363 (1992).
13. M.G.S.R.Thomas, P.G.Bruce, and J.B.Goodenough, J.Electrochem. Soc., 132, 1521(1985).
14. J.R.Dahn, U.von Sacken and C.A.Michal, Solid State Ionics, 44, 87(1990).
15. W.Rudorff and H.Kornelson, Revue de Chimie minerale, 6, 137(1969).
16. R.J.Cava, D.W.Murphy, and S.M.Zahurak, J.Electrochem.Soc., 130, 2345(1983).
17. C.Ho, I.D.Raistrick, and R.A.Huggins, J.Electrochem.Soc., 127, 343(1980).
18. S.T.Coleman, W.R.McKinnon, and J.R.Dahn, Physical Review B, 29, 4147(1984)
19. S.Yamamoto, K.Matsui, M.Wakihara, and M.Taniguchi, Mat.Res.Bull., 18, 1311(1983).
20. Y.Takeda, R.Kanno, M.Noda, and O.Yamamoto, Mat.Res.Bull., 20, 71(1985).
21. Y.Sakurai and J.Yamaki, J.Electrochem.Soc., 135, 791(1988).
22. M.Pasquali, G.Pistoia, V.Manev, and R.V.Moshtev, J.Electrochem.Soc., 133, 2455(1986).
23. D.W.Murphy, P.A.Christian, F.J.DiSalvo, and J.N.Carides,

J.Electrochem.Soc., 126, 497(1979).
24. K.M.Abraham, J.L.Goldman, and M.D.Dempsey,J.Electrochem.Soc., 128, 2493(1981).
25. R.Selim and P.Bro, J.Electrochem.Soc., 121, 1467(1974).
26. F.W.Dampier and S.B.Brummer, Electrochimica Acta, 22, 75 (1977).
27. D.Aurbach, Y.Gofer, and JK.Langzam., J.Electrochem.Soc., 136, 3198(1989).
28. R.Fong, M.C.Reid, R.S.McMillan, and J.R.Dahn, J.Electrochem.Soc., 134, 516(1987).
29. V.R.Koch, J.L.Goldman, C.J.Matos, and M.Mulvaney, J.Electrochem.Soc., 129, 1(1982).
30. K.M.Abraham, D.M.Pasquariello, and E.B.Willstaedt, J.Electrochem.Soc., 137, 743(1990).
31. C.J.Wen, B.A.Boukamp, R.A.Huggins, and W.Weppner, J.Electrochem.Soc., 126, 2258(1979).
32. R.Kanno, Y.Takeda, T.Ichikawa, K.Nakanishi, and O.Yamamoto, J.Power Sources, 26, 535(1989).
33. B.Di Pietro, M.Patriarca, and B.Scrosati, J.Power Sources, 8, 289(1982).
34. R.Fong, U.v.Sacken, and J.R.Dahn, J.Electrochem.Soc., 137, 2009(1990).
35. J.R.Dahn, R.Fong, and M.J.Spoon, Phys.Rev.B, 42, 6424(1990).
36. M.Mohri, N.Yanagisawa, Y.Tajima, H.Tanaka, T.Mitate, S.Nakajima, M.Yoshida, Y.Yoshimoto, T.Suzuki, and H.Wada, J.Power Sources, 26, 545(1989).
37. D.Guyomard and J.M.Tarascon, J.Electrochem.Soc., 139, 937 (1992).

Part I

Cathodic Reaction Mechanisms of Lithium Insertion Compounds

Chapter 1. Lithium Diffusion Behaviors in MoS_2 Thin Film Electrode Prepared by CVD Method.

1.1 Introduction

As a cathode of secondary lithium battery, various materials have been investigated. In the case of inorganic materials, the cation often inserts into their interstitial space. The layered materials, especially, have the large interstices, where the alkaline metals can easily intercalate[1,2,3]. MoS_2 also has the layered structure and has been proposed to be a good candidate as the cathode of the lithium secondary battery[4]. However, its discharge and charge characteristics are different from those of TiS_2[5]. The discharge and charge characteristics are sometimes controlled by the lithium diffusion. Therefore, such a difference may be caused by the different behavior of lithium diffusion in each materials. In this study, the diffusion coefficients of lithium in van der Waals gap of MoS_2 were measured in order to understand the relationship between the discharge behavior and the lithium diffusion.

Usually, in the practical cell, the powder of the active material is used. When the diffusion coefficient is measured using the powder sample, a lot of factors must be considered. In order to overcome this disadvantage, the oriented MoS_2 thin film synthesized by chemical vapor deposition (CVD) method is used.

The c-plane of MoS_2 crystals prepared by CVD method oriented in perpendicular to the substrate and the edge of planar crystal is exposed directly to the electrolyte. When this film is discharged, lithium diffuses in one-direction through the van der Waals gap. The mathematical treatment of lithium diffusion can thus be simplified by using this film.

1.2 Experimental

The MoS_2 thin film was prepared by using CVD method. The reaction was carried out in the apparatus as shown in Fig. 1-1.

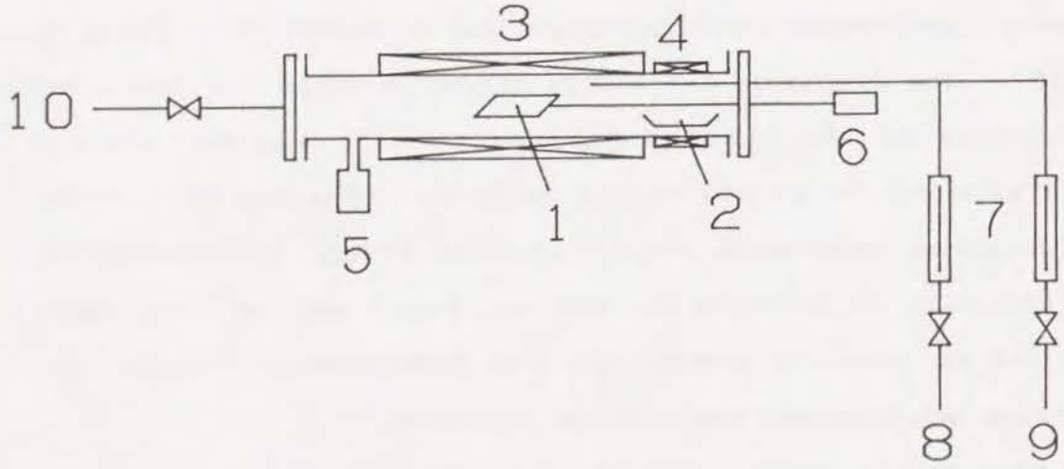

Fig. 1-1 Chemical Vapor Deposition apparatus, 1;carbon plate with thermocouple, 2;$MoCl_5$ powder, 3;electric furnace, 4;ribbon heater for heating of $MoCl_5$, 5;pirani gauge, 6;temperature controller, 7;flow meters, 8;Ar cylinder, 9;H_2S cylinder, 10;vacuum pump

The reaction chamber was made of Pyrex glass. The chamber was evacuated to 10^{-2} Torr before the experiments. The source gas was supplied from the end of the chamber. The carbon plate was placed in the center of a glass tube. The substrate (SUS 306) was put on this plate. The heating was done by the Golden Image furnace(Ulvac type RHL). The carbon plate only could be heated. The temperature was measured by the thermocouple molded in the carbon plate. The pressure was monitored by the pirani gauge(Ulvac style GP-2A). $MoCl_5$ and H_2S were used as Mo and S sources, respectively. The reaction temperature was 723 K. The prepared thin film was examined by using scanning electron microscopy, X-ray diffraction method, and electron spectroscopy for chemical analysis(ESCA).

The current-time transients in the course of the potentiostatic discharge were measured. Lithium metal was used as reference and counter electrodes. The electrolyte was propylene carbonate containing 1.0 M $LiBF_4$. The temperature was controlled in order to estimate the activation energy (E_a) and pre-exponential factor (D_0) for the diffusion of lithium in MoS_2. They were estimated from the Arrhenius plot. After the discharge, the x-ray analysis was carried out. All procedures were carried out under Ar atmosphere.

Model of the One-Dimensional Finite Diffusion of Lithium in MoS_2 Thin Film

The lithium diffusion in the c-axis oriented MoS_2 was assumed to be one-dimensional finite system. The current-time transient curves in the course of the potentiostatic discharge can be calculated according to the Fick's second law. If the electrode reaction of MoS_2 is controlled by the lithium diffusion, the lithium concentration at the surface (C_0) can be assumed to be constant in the course of the potentiostatic discharge. The initial and boundary conditions for one-dimensional finite system are written as follows

$$\frac{\partial C(x,t)}{\partial t} = D \frac{\partial C^2(x,t)}{\partial x^2} \qquad (1)$$

$$C(x,t)=C_0 \qquad t = 0 \qquad 0 < x < l \qquad (2)$$

$$C(x,t)=C^* \qquad t > 1 \qquad x = l \qquad (3)$$

$$\frac{\partial C(x,t)}{\partial x} = 0 \qquad x = 0 \qquad (4)$$

where D is the diffusion coefficient of lithium in MoS_2, l is the thickness of MoS_2 film, C_0 is the initial concentration of lithium in MoS_2, C^* is the concentration of lithium at the film surface during the potential step. The current-time transients can be obtained from the solution of Eq. 1, as follows

$$\frac{i(\tau)}{i_\infty} = \frac{1}{\sqrt{\pi\tau}}\{\sum_{n=1}^{\infty}(-1)^n \exp(-n^2/\tau) + \sum_{n=1}^{\infty}(-1)^{n+1} \exp[-(n+1)^2/\tau]\} \qquad (5)$$

$$i_\infty = \frac{nFAD(C^* - C_0)}{l} \qquad (6)$$

$$\tau = \frac{Dt}{l^2} \qquad (7)$$

where F is the Faraday constant. The change of the concentration profile in the film during the potentiostatic discharge is illustrated in Fig. 1-2. From the comparison between the calculated curve and the observed one, the diffusion coefficient D can be estimated[6].

1.3 Results and Discussion

Figure 1-3 shows the discharge and charge curves of the powder MoS_2. The most interesting feature of the first discharge curve is the large polarization in $0<x<0.1$ region and the plateau

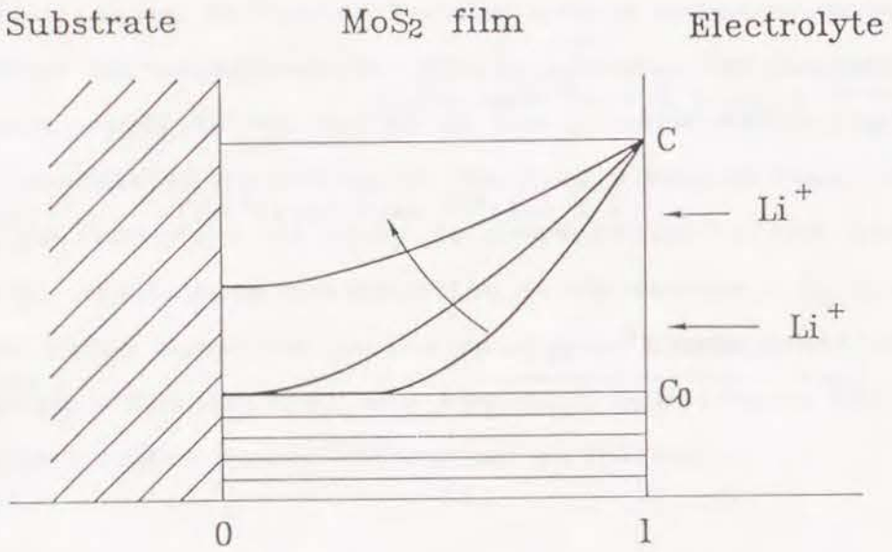

Fig. 1-2 Change of the concentration profile of lithium in the MoS_2 film in the course of the potentiostatic discharge.

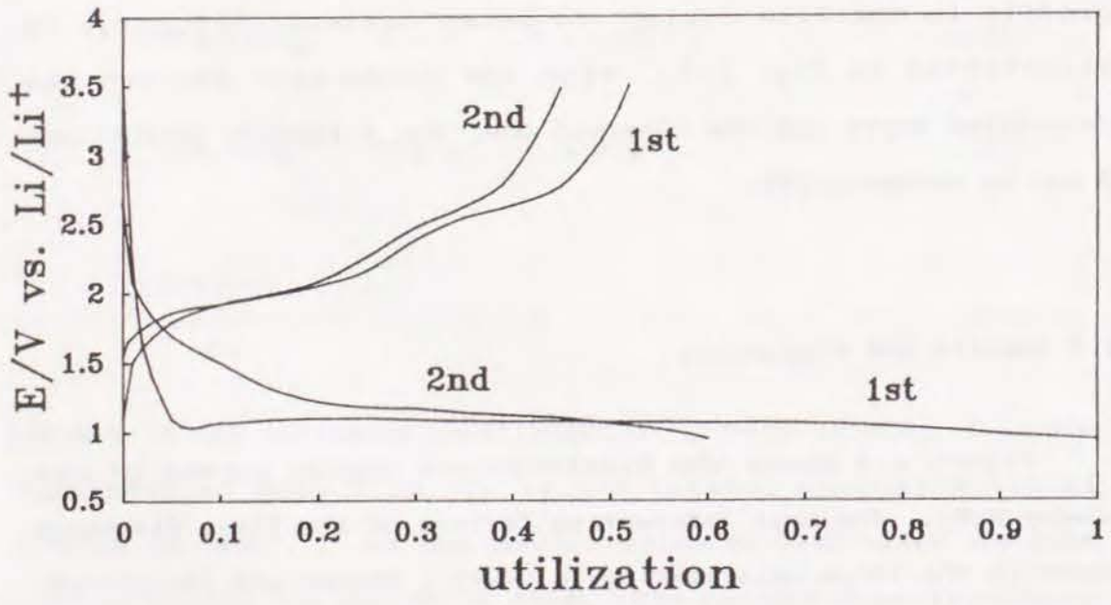

Fig. 1-3 Discharge and charge characteristics of the powder MoS_2.

region appearing in $0.1<x<1.0$, where x indicates the ratio of Li to MoS_2. In general, the discharge curves for the insertion of lithium into other compounds, e.g., TiS_2 and MnO_2, are characterized by the S-shaped curve. From these facts, it can be seen that the first discharge mechanisms of MoS_2 are different from those of TiS_2 and MnO_2. On the other hand, the second charge-discharge behavior was similar to that of other layered compounds. The discharge curves of MoS_2 may be related to the change of physical properties of MoS_2 in the course of the discharge. The diffusion behavior of lithium in MoS_2 is one of the physical property of the MoS_2 cathode. Therefore, the measurement of the diffusion coefficient of lithium in MoS_2 provides the information about the discharge mechanisms of MoS_2.

The oriented film was helpful for simplifying the diffusion model and mathematical calculations. In this study, the MoS_2 thin film was prepared by the CVD method. The low pressure CVD method proved to be able to prepare the thin film of MoS_2[7]. $MoCl_5$ was vaporized at 373 K. The gases of $MoCl_5$ and H_2S reacted to deposit on the substrate as the MoS_2 thin film. The pressure of H_2S was 1.0 Torr. The deposition rate was calculated as the increment of the weight per minute at various reaction temperatures, as shown in Fig. 1-4. The deposition rate changed suddenly above 723 K, probably due to the decomposition of H_2S gas. At 673 K, it may be possible that the atomic sulfur reacts with the $MoCl_5$, leading to a high deposition rate. The MoS_2 thin films used in the following sections were prepared at 723 K.

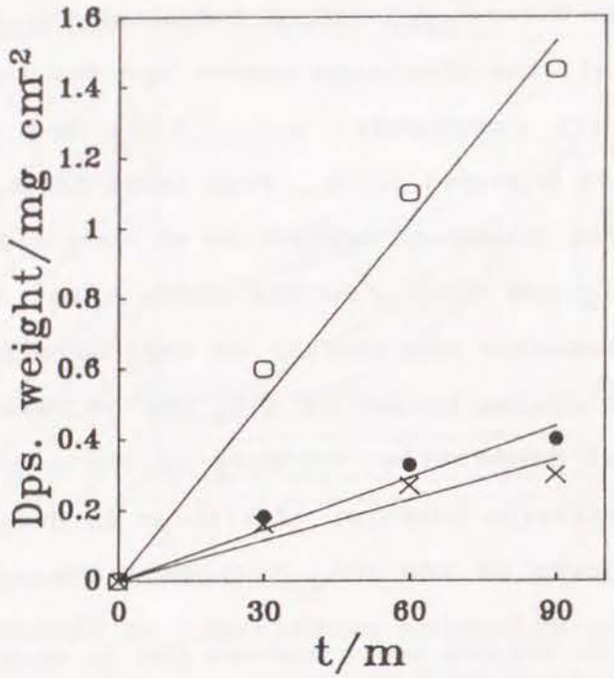

Fig. 1-4 Rate of the MoS_2 film deposition under various temperatures, o;723 K, ●;698 K, ×;673 K.

The x-ray diffraction pattern of the synthesized MoS_2 thin film was shown in Fig. 1-5. Some peaks from (001) reflection planes disappeared in the synthesized film. If the crystal planes were oriented parallel to the direction of the x-ray radiation, the diffraction cannot occur[7]. From this result, the c-axis orientation of the film was confirmed. In the case of the measurement of the diffusion coefficient of lithium by using such a highly oriented film, the one-dimensional linear diffusion model was used.

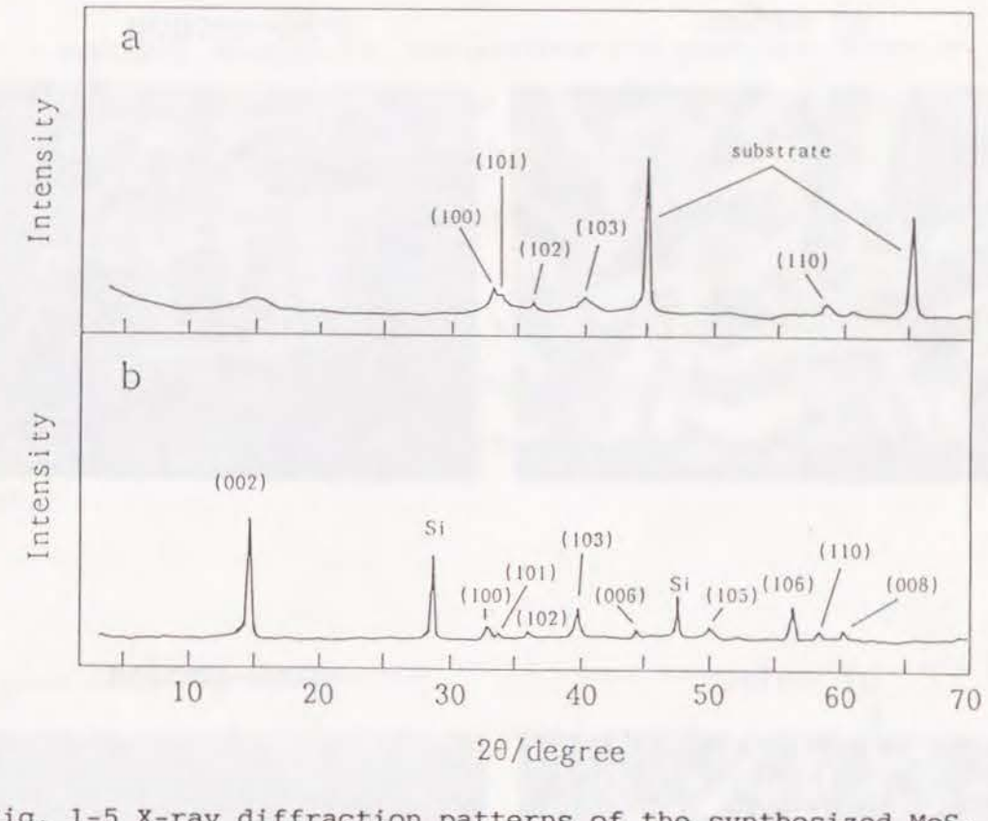

Fig. 1-5 X-ray diffraction patterns of the synthesized MoS_2 film(a) and the powder MoS_2(b).

Figure 1-6(a) shows the SEM photograph of the film synthesized at the heating rate of 100 Kmin^{-1}. Large plate-like MoS_2 crystals deposited vertically to the substrate. This photograph indicates the formation of c-axis oriented crystalline MoS_2. As shown in the cross-sectional photograph, the inner part of the deposited film was not so porous. With decreasing of the heating rate (e.g., 30 Kmin^{-1}), the more dense film was synthesized, as shown in Fig. 1-6(b). The apparent density of the dense film was estimated to be 3.9 g cm^{-3} from the observed film thickness and the weight of the deposited film. Theoretical density of MoS_2 was 4.8 g cm^{-3}.

a) surface

cross-section

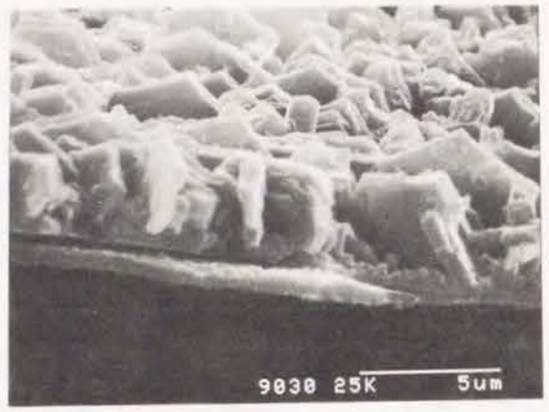

b) surface

cross-section

Fig. 1-6 SEM photographs at the surface and the cross-section of the MoS_2 film, (a);heated at 100 $Kmin^{-1}$, (b);heated at 30 $Kmin^{-1}$.

The ESCA spectra of the synthesized film are shown in Fig. 1-7. These peaks correspond to Mo^{4+} $2p_{3/2}$ and $2p_{1/2}$. The spectrum of the synthesized film was very similar to the powder MoS_2. Any peaks corresponding to Mo^{3+} or Mo^{5+} were not observed. Thus, it can be seen that the valence of Mo in the synthesized film is 4. This fact also shows the stoichiometry of the synthesized film is close to that of MoS_2. From these analyses, it is concluded that the synthesized film was c-axis oriented 2H-MoS_2.

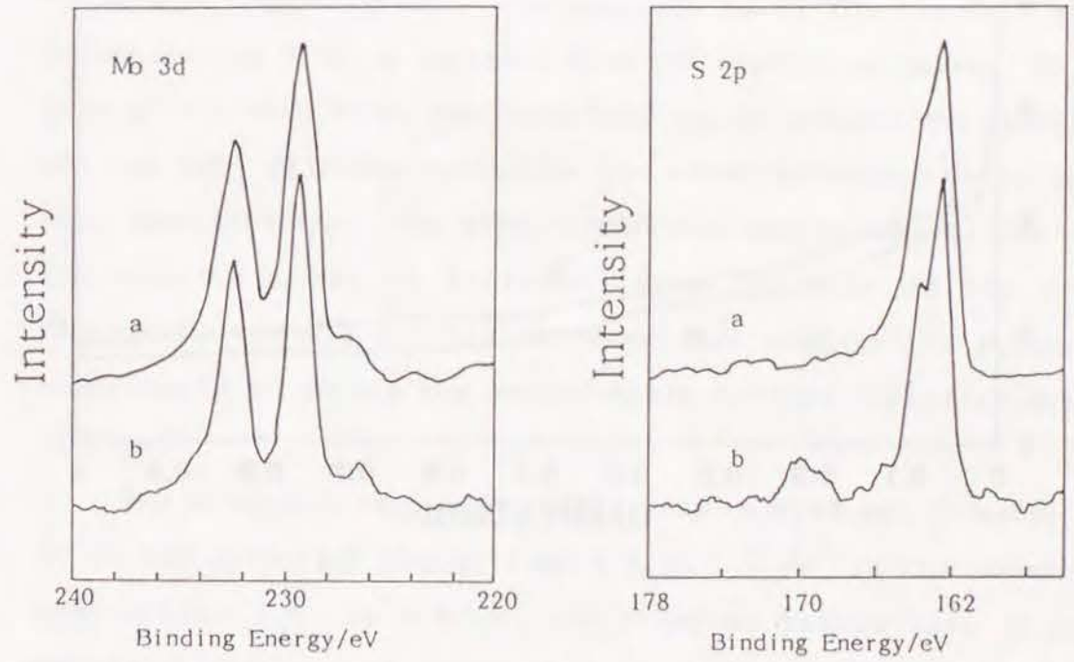

Fig. 1-7 ESCA spectra of Mo3d and S2p of the synthesized MoS_2 film(a) and the powder MoS_2(b).

The discharge curves are shown in Fig. 1-8. The discharge current density was 10 μAcm^{-2}. The discharge characteristics of the MoS_2 film were very similar to those of the powder MoS_2, as shown in Fig. 1-3. The polarization rapidly increased in the early stage of the discharge curve ($0 < x < 0.2$) and then became constant. This fact indicates that the electrochemical kinetics of the MoS_2 thin film is similar to the powder MoS_2.

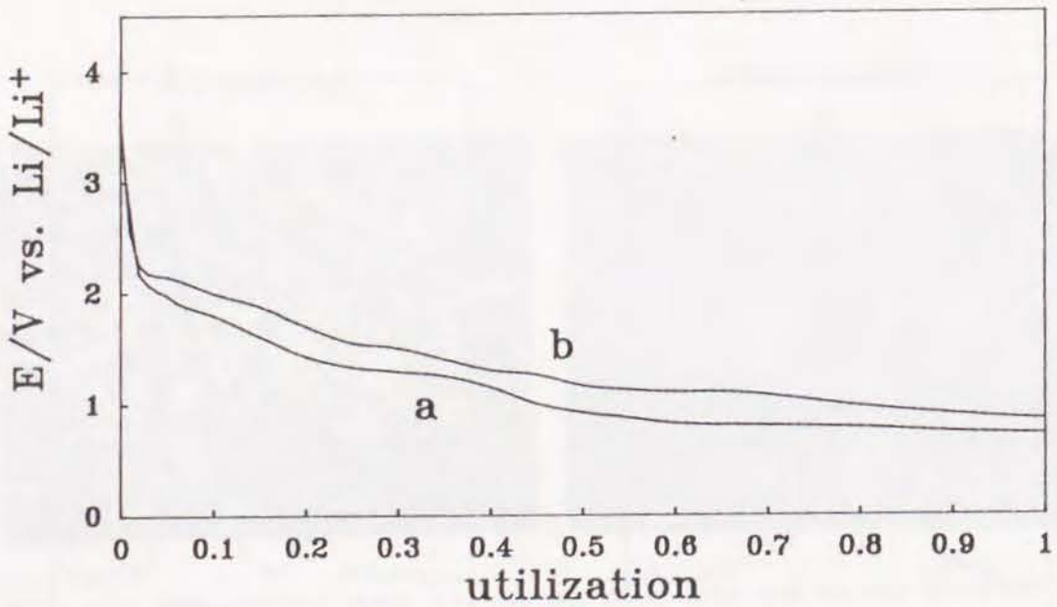

Fig. 1-8 Discharge characteristics of MoS_2 in propylene carbonate containing 1.0 M $LiBF_4$(a) and tetrahydrofuran containing 1.0 M $LiBF_4$(b).

The MoS_2 films were discharged potentiostatically and the current-time transients were measured. First of all, in order to confirm the reliability of this measurement, the dependence of the diffusion coefficient of lithium on the film thickness was investigated. The films whose thickness were 0.92, 2.2, and 3.6 μm, were prepared. The current-time transients during the potentiostatic discharge from 3.6 V to 3.3 V were measured for each film, as shown in Fig. 1-9. From the comparison between the calculated curve and the observed one, the diffusion coefficients of lithium in MoS_2 films whose thickness are 2.2 and 3.6 μm, were estimated to be 9.3×10^{-13} cm^2s^{-1} and 8.6×10^{-13} cm^2s^{-1}, respectively. The observed curve for the film whose thickness was 0.92 μm deviated from the calculated curve. In the case of the thin film, the interface region between the substrate and the MoS_2 film may influence the electrochemical behavior of MoS_2 significantly. The film orientation and/or composition near the substrate may be different from the bulk of the film. Therefore, the 2.0 μm film thickness was used in the following experiments to obtain the reproducible diffusion coefficient of lithium.

The potential step experiments were carried out in every 500 mV in the potential region from 3.6 to 1.1 V. In the potential region from 3.6 to 1.5 V, the observed values were in good agreement with the theoretical curve as shown in Fig. 1-10(a). This means that lithium intercalates into the van der Waals gap and diffuse one-dimensionally through the octahedral sites surrounded by the six sulfur atoms[8]. The diffusion coefficient

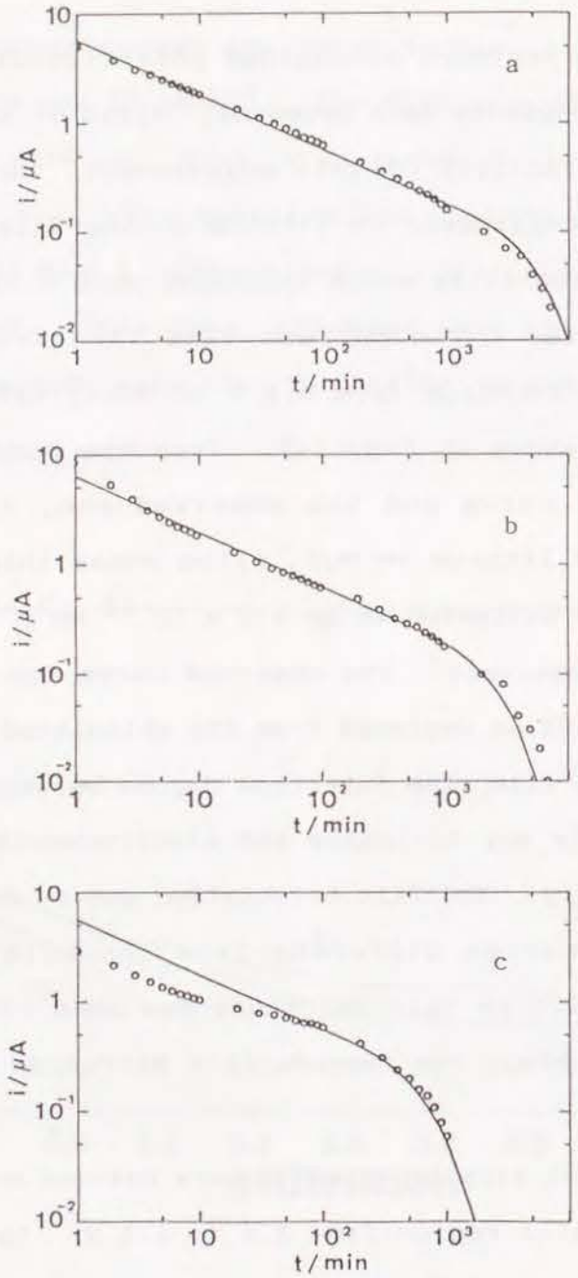

Fig. 1-9 Current-time transients in the course of the potentiostatic discharge of the MoS_2 films with various thickness, a;3.6 μm, b;2.2 μm, c;0.92 μm.

was estimated to be 5×10^{-13} $cm^2 s^{-1}$. Probably, the large polarization, as shown in Fig. 1-8, is due to the poor diffusivity of lithium in MoS_2.

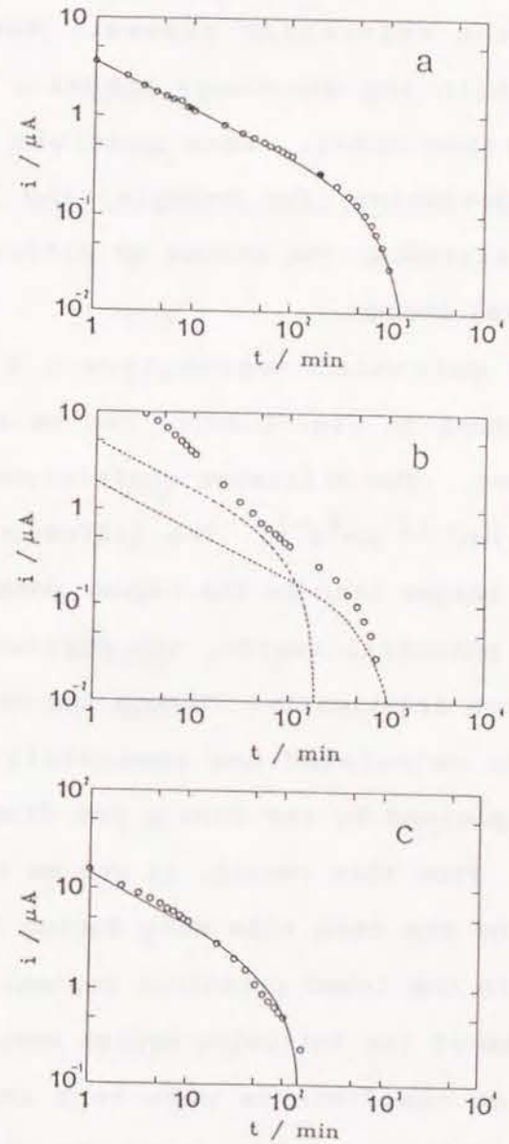

Fig. 1-10 Current-time transients in the course of the potentiostatic discharge of the MoS_2 films in various potential regions, a; from 3.6 to 1.5 V, b;from 1.5 to 1.2 V, c;from 1.2 to 0.9 V.

In the potential region from 1.5 to 1.2 V, the deviation of the observed curve from the calculated one was very large as shown in Fig. 1-10(b). The current-time transient might consist of two types of the relaxation curves. Therefore, it is impossible to explain the discharge behavior using the one-dimensional diffusion model. Some possible reasons can be proposed for the deviation, for example, the increase of the charge-transfer resistance, the change of diffusion coefficient due to the structural change.

In the lower potential region from 1.2 to 0.9 V, the current-time transient in Fig. 1-10(c) can be explained by the one relaxation curve. The diffusion coefficient of lithium was estimated to be 5 $x10^{-12}$ cm^2s^{-1}. The diffusion coefficient in this potential was larger than in the higher potential region (> 1.5 V). In this potential region, the physical properties of MoS_2 would not change drastically. Though the observed curve did not agree with the calculated one completely, the discharge behavior can be explained by the finite one-dimensional lithium diffusion in MoS_2. From this result, it can be expected that the structural change of the thin film MoS_2 during the discharge is almost terminated in the lower potential region. The summary of these data and those of the following cycles were listed in Table 1-1. The diffusion coefficients were kept in the same value after the first discharge. This means the physical property change of the thin film MoS_2 was irreversible reaction. Probably the thin film MoS_2 changes to another stable structure after the discharge.

Table 1-1 The diffusion coefficients in charge-discharge cycles.

	Potential (V)	Diffusion coefficient (cm^2s^{-1})
1st discharge	3.0	$5.3x10^{-13}$
	1.3	-
	1.0	$5.1x10^{-12}$
1st charge	1.0	$5.1x10^{-12}$
	3.0	$4.8x10^{-12}$
2nd discharge	3.0	$4.9x10^{-12}$
	1.0	$5.0x10^{-12}$
2nd charge	1.0	$4.5x10^{-12}$
	3.0	$4.8x10^{-12}$

The activation energies and pre-exponential factors for the lithium diffusion in MoS_2 listed in Table 1-2 were estimated from the Arrhenius plots shown in Fig. 1-11. The activation energies in both potential regions are not high for the diffusion process, but the pre-exponential factors are very small. So, the small diffusion rate is not caused by the potential well, but the jump frequency. It is not clear why this frequency is so small, but one possibility is that the local strain of the host lattice between the jump sites is small. In addition, for the diffusion model itself, there are some additional factor, e.g., an elastic interaction energy between intercalated lithium atoms.

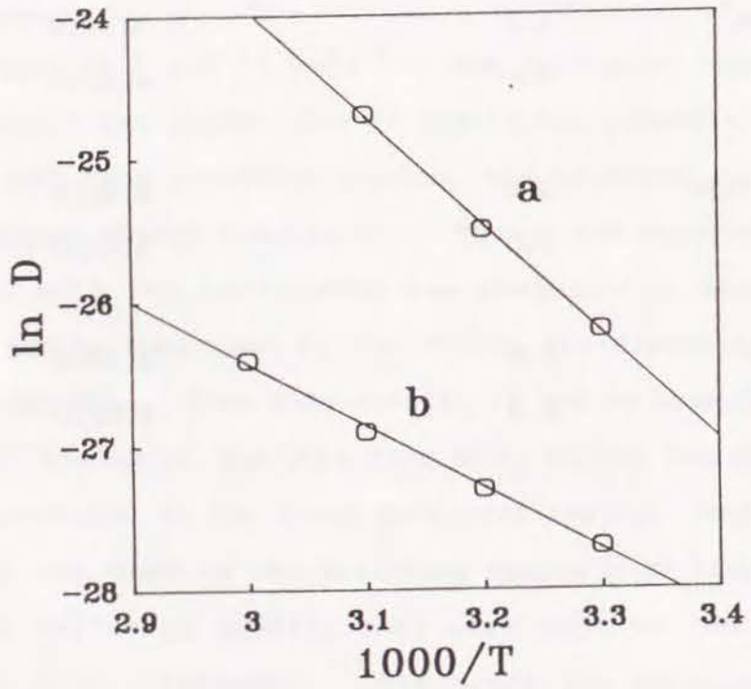

Fig. 1-11 Arrhenius plots for the diffusion of lithium in the MoS_2 film in the two different potential regions, a;from 1.2 to 0.9 V, b;from 3.6 to 1.5 V.

Table 1-2 Parameters of Arrhenius plot(D, D_0, and Ea).

Potential region	D/cm^2s^{-1}	D_0/cm^2s^{-1}	$Ea/kcalmol^{-1}$
3.6 ~ 1.5 V	$5x10^{-13}$	$1x10^{-6}$	8.6
1.2 ~ 0.9 V	$5x10^{-12}$	$2x10^{-1}$	15

It was reported that the phase transformation from 2H to 1T type structure occurs in the region of $0.2 < x < 1.0$ in Li_xMoS_2 [5]. The potential plateau region in the discharge curve may be due to some structural change. In fact, some new peaks were observed in the x-ray diffraction pattern of the MoS_2 powder after 100% discharge, as shown in Fig. 1-12. Moreover the intensities of the peaks totally decreased after the discharge. Therefore the change of the diffusion coefficients may be caused by these structural changes. On the other hand, any clear peaks were not observed in the x-ray diffraction pattern after 100 % discharge of the thin film MoS_2. This indicates that the structure of the Li_xMoS_2 film becomes amorphous completely after

100% discharge. In both cases the decrease of the crystallinity of MoS_2 was clearly observed. Such a structural change influences the diffusion behavior of lithium. Probably the diffusion coefficient of ion in the solid increased with decreasing crystallinity[6]. Moreover, the transformation from 2H to 1T type structure also is related to the diffusion of lithium. In this case, the diffusion coefficient of lithium also increases.

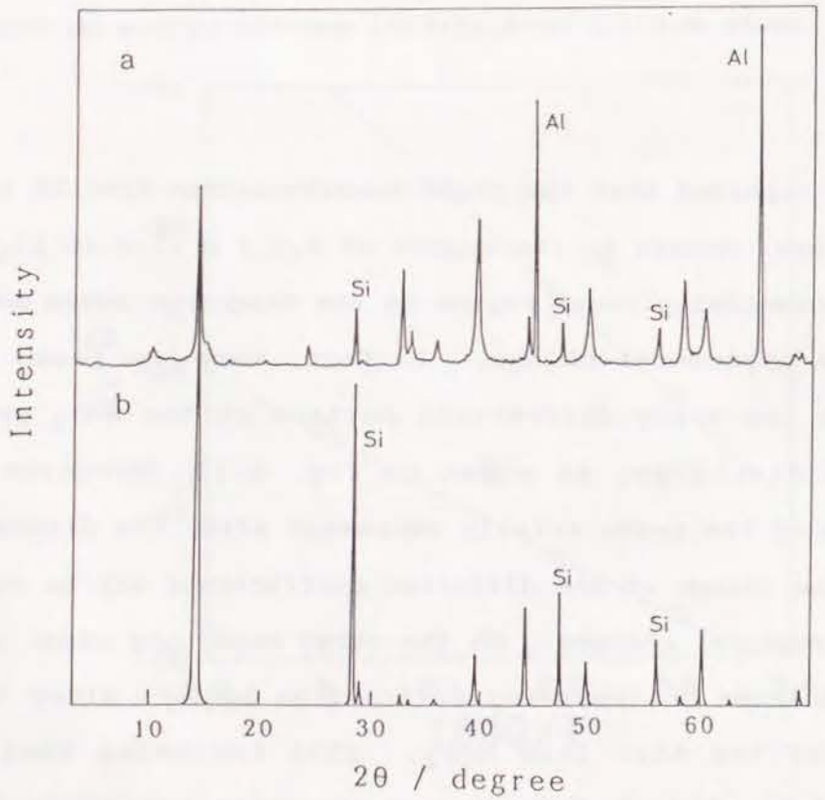

Fig. 1-12 X-ray diffraction patterns of $LiMoS_2$(a) and the powder MoS_2(b).

References

1. M.B.Dines, Mat.Res.Bull., 10, 287(1975).
2. T.R.Halbert and J.Scanlon, Mat.Res.Bull., 14, 415(1979).
3. D.W.Murphy and F.A.Trumbore, J.Crystal Growth, 39, 185(1977).
4. J.A.R.Stiles, New Materials & New Processes, 3, 89(1985).
5. M.A.Py and R.R.Haering, Can.J.Phys., 61, 76(1983).
6. K.Kanamura, K.Yuasa, and Z.Takehara, J.Power Sources, 20, 127(1987).
7. K.Kanehori, F.Kirino, Y.Ito, K.Miyauchi, and T.Kudo, J.Electrochem.Soc., 136, 1265(1989).
8. M.S.Whittingham, Prog.Solid State Chem., 12, 41(1978).
9. K.M.Abraham, G.L.Holleck, T.Nguyen, D.M.Pasquariello, and D.A.Schwartz, J.Power Sources, 26, 313(1989).
10. B.DI Pietro, M.Patriarca, and B.Scrosati, Synthetic Metals, 5, 1(1982).

Chapter 2. Effect of Electrolyte Solvents on Lithium Intercalation into MoS_2.

2.1 Introduction

MoS_2 has been studied as a cathode material for high energy secondary lithium cells with aprotic organic electrolytes[1-5]. The structurally modified Li_xMoS_2 has been known to discharge at about 2 V showing a good cycling behavior[6]. This Li/MoS_2 system was commercialized by Moli Energy Ltd. and the "AA" size cell showed higher performance than Ni-Cd cell under some conditions, such as C/5 rate cycling[7,8]. Thus, this cell has been expected to be applied as a power source for portable devices. A problem of this cathode material is to induce the decomposition of the electrolytes, which results in the decrease of cycle life[9]. However, the decomposition mechanism has not been clarified yet.

The lithium intercalation process into MoS_2 is an interesting phenomenon from the view point of fundamental research, because the intercalation induces the change of electronic and magnetic properties, and structural modification of the host lattice[10-13]. As lithium was intercalated into 2H-MoS_2, the phase transition to 1T structure was found in the range from x=0.2 to x=1.0 in Li_xMoS_2[6]. In this study, we have investigated the charge-discharge characteristics of the Li/2H-

MoS_2 cell and the structural change of 2H-MoS_2 by lithium intercalation. Especially, the effect of electrolyte solvent has been examined.

2.2 Experimental

The MoS_2 powder was provided from Sumitomo Metal Mining Co., Ltd., whose average particle size was 10μm in diameter. The powder was dried at 150 °C for several days before use.

Chemically lithiated MoS_2 was prepared by the reaction of MoS_2 with n-butyllithium. Five grams of MoS_2 was mixed and stirred with 40 ml of 1.6 M n-butyllithium in hexane at room temperature for three days. The reaction products were washed with n-hexane, and then dried under vacuum at room temperature. The lithium content in the reaction products was analyzed by atomic absorption method to be determined as $Li_{1.12}MoS_2$.

Charge-discharge tests were carried out by using the coin-type cell(CR2025) as shown in Fig. 2-1. One hundred mg of the MoS_2 powder was pressed into a tablet in 8 mm diameter under 10 MPa. The lithium sheet with 0.34 mm in thickness was used as the anode. The electrodes were separated by a microporous polypropylene sheet. The electrolytes used in the present study were 1M solution of $LiClO_4$ in propylene carbonate(PC)/dimethoxyethane(DME)[1:1 by volume] and 1M solution of $LiClO_4$ in DME, which were supplied from Mitsubishi Petrochemical Co., Ltd. The test cells were cycled

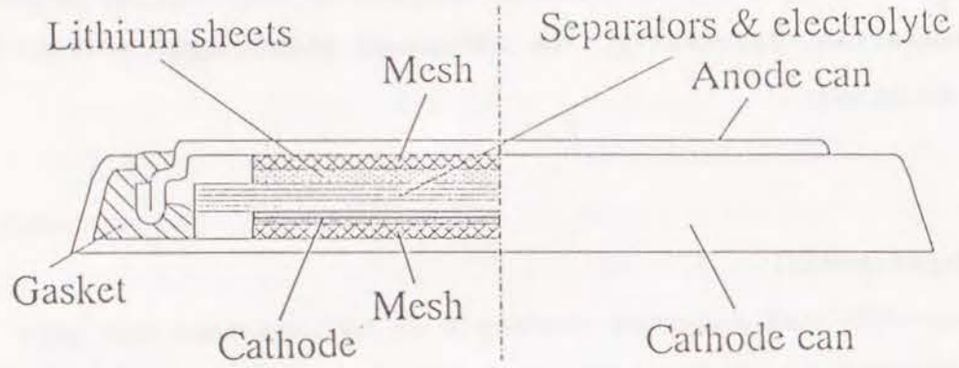

Fig. 2-1 The experimental coin-type cell for electrochemical measurements.

galvanostatically between 0.9 and 3.5 V at a constant current density of 200 μAcm^{-2}. The lattice parameters were measured by X-ray diffractometer(Rigaku Rotaflex RU-200B) with CuKα radiation. The XRD measurements for lithium intercalated products were done by covering the sample with aluminum thin film with 7 μm in thickness in order to avoid the contact with moisture. The silicon powder was used as the inner standard material. The construction of the cell, preparation of the sample for XRD measurements and all other procedures were performed in an Ar atmosphere dry box.

2.3 Results and Discussion

The first five cycles of the Li/2H-MoS_2 cell using PC-DME and DME as the electrolytes are shown in Fig. 2-2. The characteristic features of the 1st discharge of these cells are the initial large voltage drops and following voltage plateau at 1.3-1.1 V. Fig. 2-2(a) shows that the cell voltages are still as high as 1.1 V after 170 $mAhg^{-1}$ discharge, which corresponds to $Li_{1.0}MoS_2$. However, the 1st charge capacity was extremely low and the cycle efficiency calculated by the ratio of charge/discharge capacity of the first cycle was only 13 %. The charge and discharge capacities of the 5th cycle diminished markedly compared to the 1st charge/discharge one. Such a low charge capacity suggests that some of irreversible reaction occurs during the voltage plateau of the discharge process.

On the other hand, the Li|DME|2H-MoS_2 cell showed rather improved cycling behaviors than in the Li|PC-DME|2H-MoS_2 cell as shown in Fig. 2-2(b). The 1st discharge profile showed almost the same as that of the PC-DME cell. However, the 1st charge process and following charge and discharge cycles showed much higher capacities. The cycle efficiency was about 53 % in the 1st cycle and showed no decrease in the following cycles.

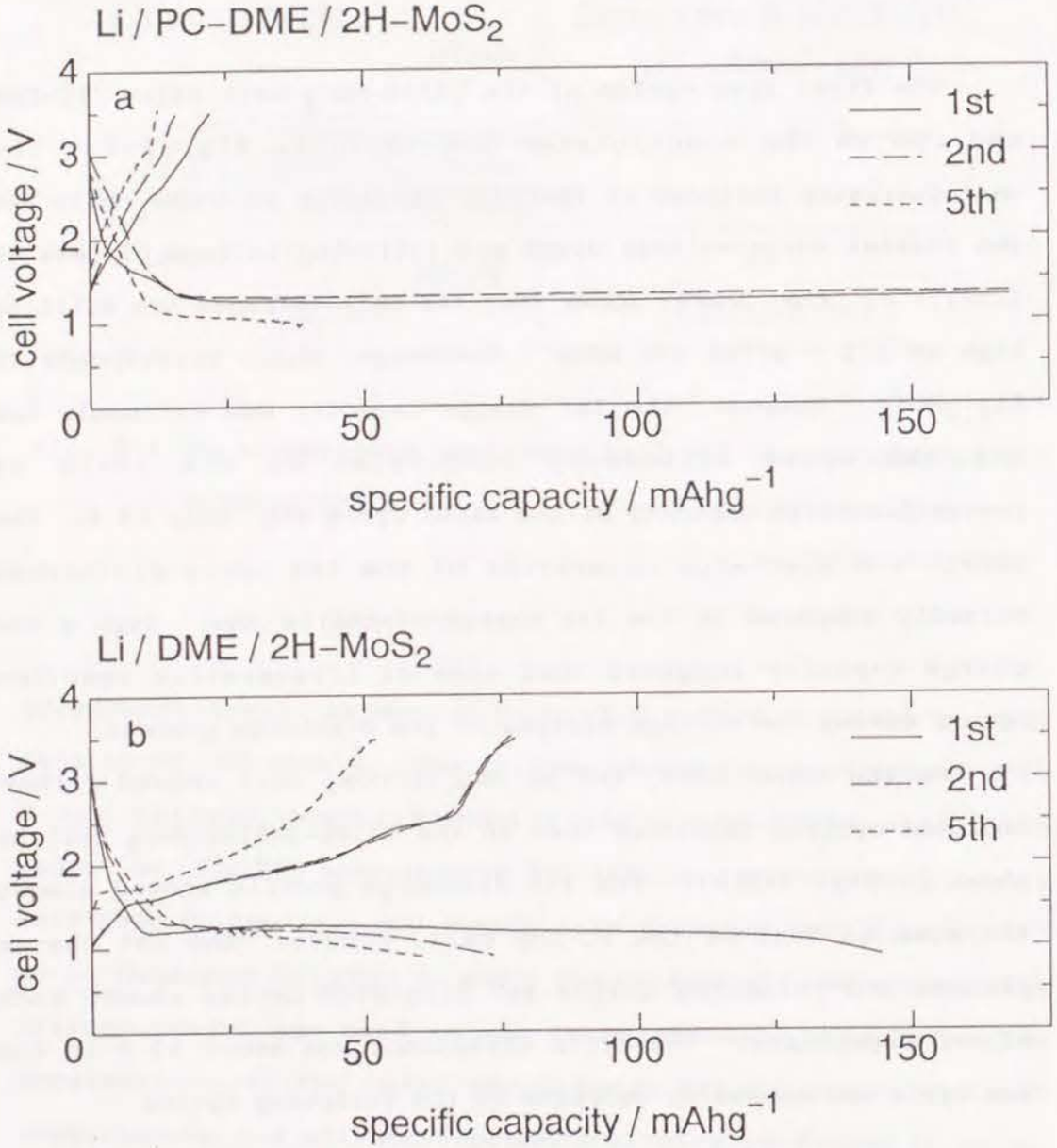

Fig. 2-2 The first five charge-discharge cycles of the Li/MoS_2 cell. (a)1M $LiClO_4$/PC-DME, (b)1M $LiClO_4$/DME.

The structural change in 2H-MoS_2 during the 1st charge-discharge cycle was analyzed by XRD measurements. Figure 2-3 shows the change of XRD patterns of the cathode material for the various steps of discharge and charge. These patterns showed several new peaks besides those of original MoS_2. If the peak at the lowest angle, 5.1°(d=14.31A) in Fig. 2-3(a), is assumed as 001 reflection of MoS_2, the peaks indicated by circles at 10.2°(8.665A), 15.3°(5.786A) and 20.5°(4.329A) can be indexed as 002, 003 and 004 reflections, respectively. From these results it is suggested that the lithiated MoS_2 has the expanded interlayer space after the lithium intercalation. In addition to the expanded phase, the third phase could be also observed as shown in Fig. 2-3. It would be clear from a peak at 13.9° and much broader peaks at around 43 and 54°, which are indicated by triangles in the figure, appeared in the patterns of the deep discharged sample to 168 $mAhg^{-1}$. As shown later, these peaks are considered to belong to the 1T phase.

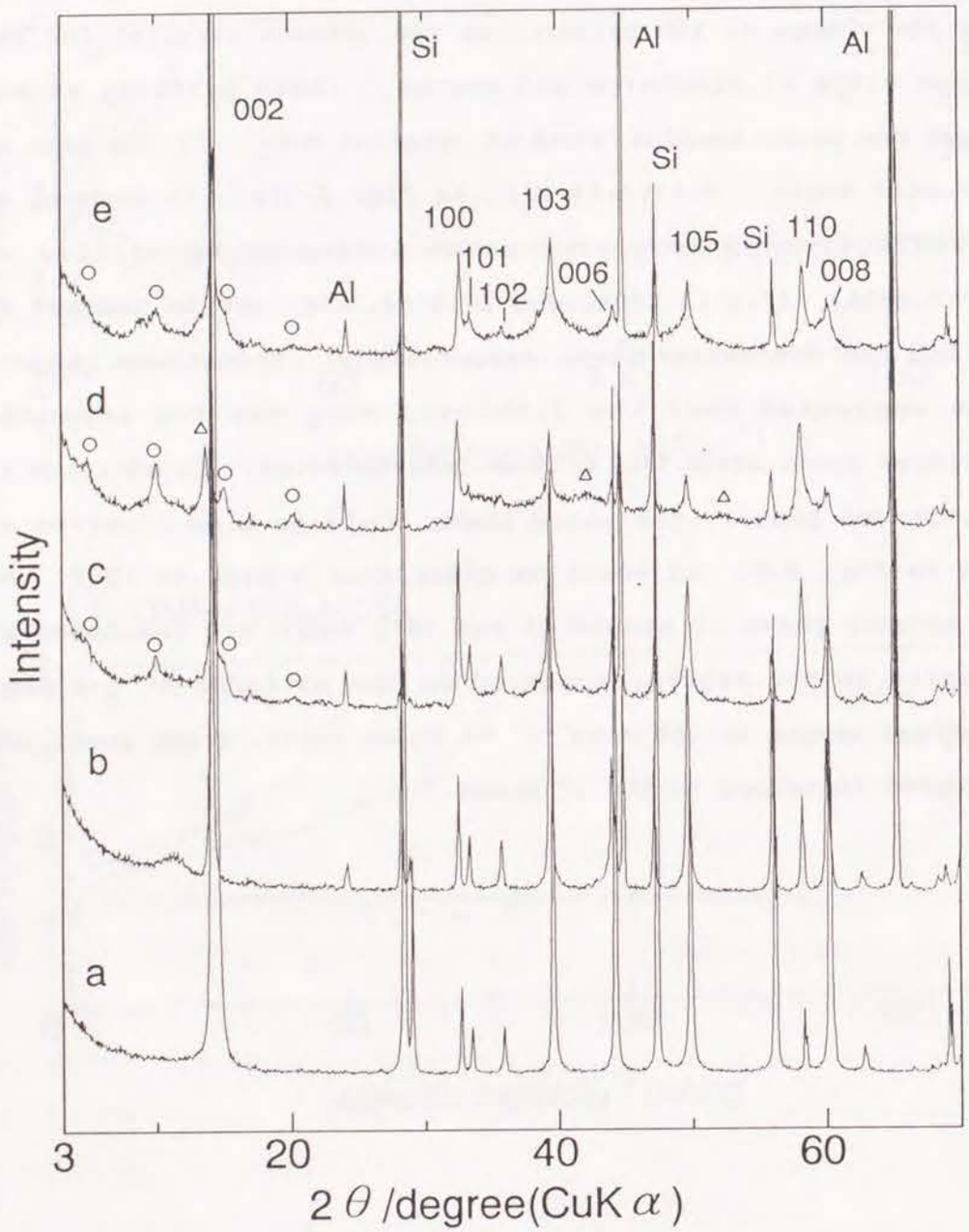

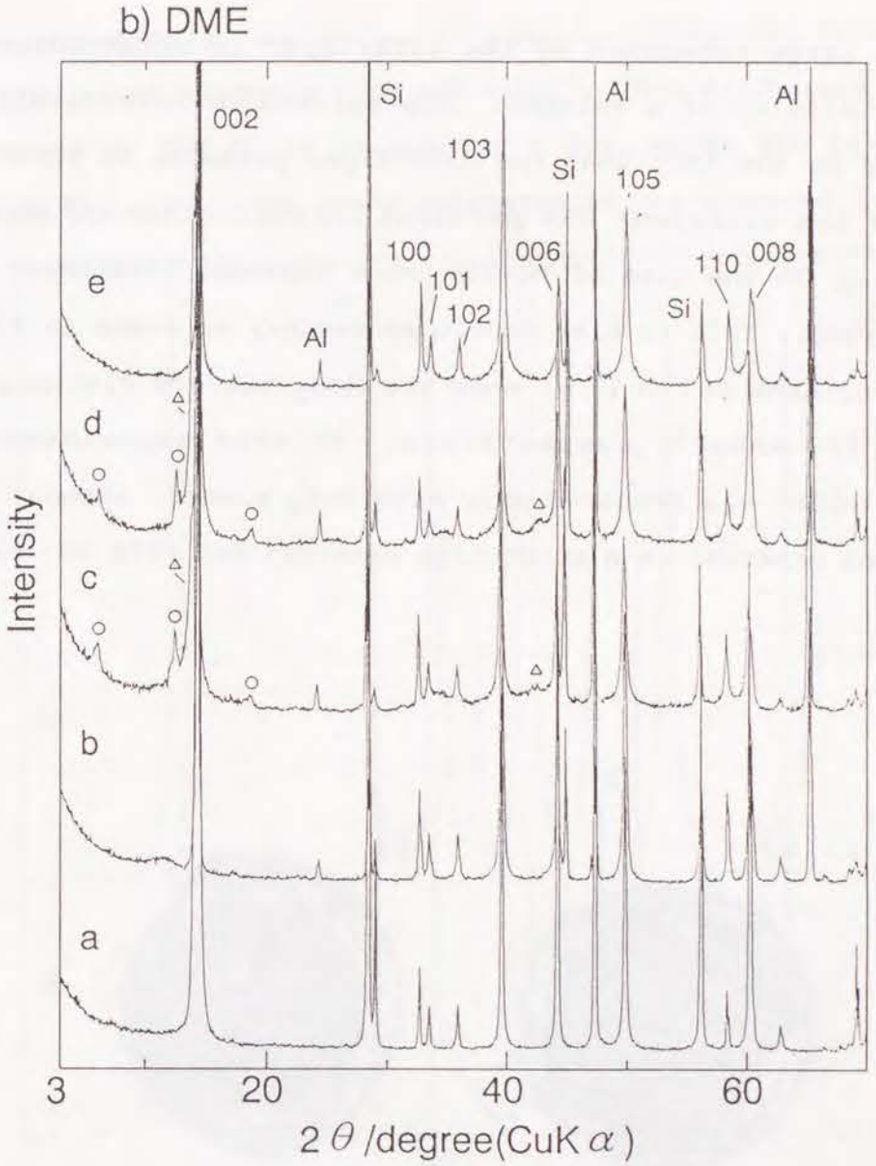

Fig. 2-3 X-ray diffraction patterns of MoS_2 during the 1st cycle.
(○)expanded MoS_2 phase,(△)1T phase.
(a) PC-DME; after a)0, b)17, c)84, d)168 $mAhg^{-1}$ discharge, and e)25 $mAhg^{-1}$ charge after 168 $mAhg^{-1}$ discharge.
(b) DME; after a)0, b)15, c)75, d)150 $mAhg^{-1}$ discharge, and e)75 $mAhg^{-1}$ charge after 150 $mAhg^{-1}$ discharge.

The large expansion of the interlayer is often induced by co-intercalation of a solvent. The solvent co-intercalation is confirmed by the fact that the discharged products in PC-DME and DME show the different XRD patterns in each other as shown in Fig. 2-3. In the case of PC-DME, more expanded interlayer space was observed. This is also convinced visibly as shown in Fig. 2-4. Photographs (a) and (b) show the MoS_2 tablets discharged to 17 and 170 $mAhg^{-1}$, respectively. In this experiment, the cathode tablet was prepared only with MoS_2 powder, without using any carbon material as a conducting material and PTFE as binding

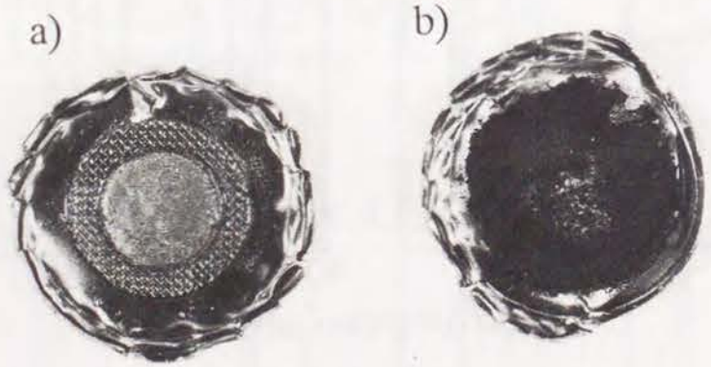

Fig. 2-4 The photographs of the MoS_2 cathode tablet (a)after 17 $mAhg^{-1}$ and (b)170 $mAhg^{-1}$ discharge.

agent. Apparently, the volume of cathode tablet was drastically increased after discharged to 170 $mAhg^{-1}$. The discharged product was heated at 300 °C in vacuum for 1 day, whose XRD pattern is shown in Fig. 2-5. The peaks indicated as the expanded layers

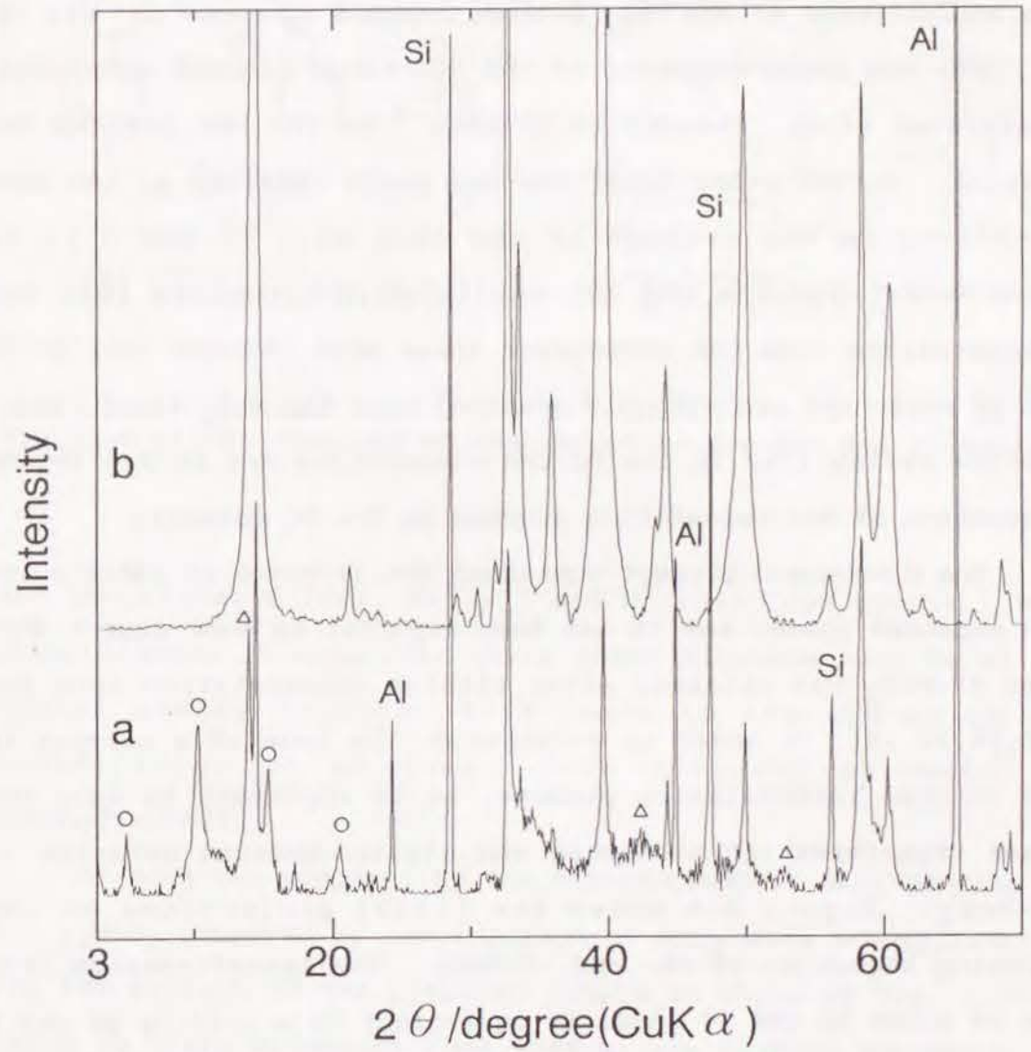

Fig. 2-5 X-ray diffraction patterns of (a) MoS_2 after the 1st discharged to 170 $mAhg^{-1}$ and (b) heat-treated discharged sample at 300 °C in vacuo. (○)expanded phase, (△)1T phase.

disappeared perfectly. This means that the intercalated solvent molecule was extracted away and the interlayer distance returned to that of original 2H-MoS_2.

The extraction of the solvent molecule was also observed in the XRD patterns of the MoS_2 cathode charged as shown in Fig. 2-3. The new peaks appeared in the discharge process completely diminished after charged to 75 $mAhg^{-1}$ in the DME cell as the solvent. On the other hand, the new peaks remained at the same positions in the cathode of the cell with PC-DME. It is considered that the DME can easily co-intercalate into and deintercalate from the interlayer space with lithium ion, while the PC molecules are strongly adsorbed onto the MoS_2 layer. Thus, the low cyclability in the PC-DME electrolyte may be due to the prevention of deintercalation process by the PC molecule.

The discharged product contained the 1T-phase in addition to the expanded phase. And it has been reported in some papers that only 1T-MoS_2 was obtained after lithium intercalation into 2H-MoS_2[6,12,13]. In order to understand the role of a solvent in the lithium intercalation process, it is important to know the phase transformation mechanism and electrochemical behavior of 1T-MoS_2. Figure 2-6 shows the (1120) projections of the stacking sequences of 2H- and 1T-MoS_2. The transformation from the 2H phase to the 1T phase is equivalent to a sliding of one S layer in a S-Mo-S slab accompanied with the sliding of S layer in an adjacent slab to opposite direction at the same distance. The trigonal prismatic coordination occurs when 4d levels of Mo atom split into three groups which are lower stabilized d_z2 orbitals

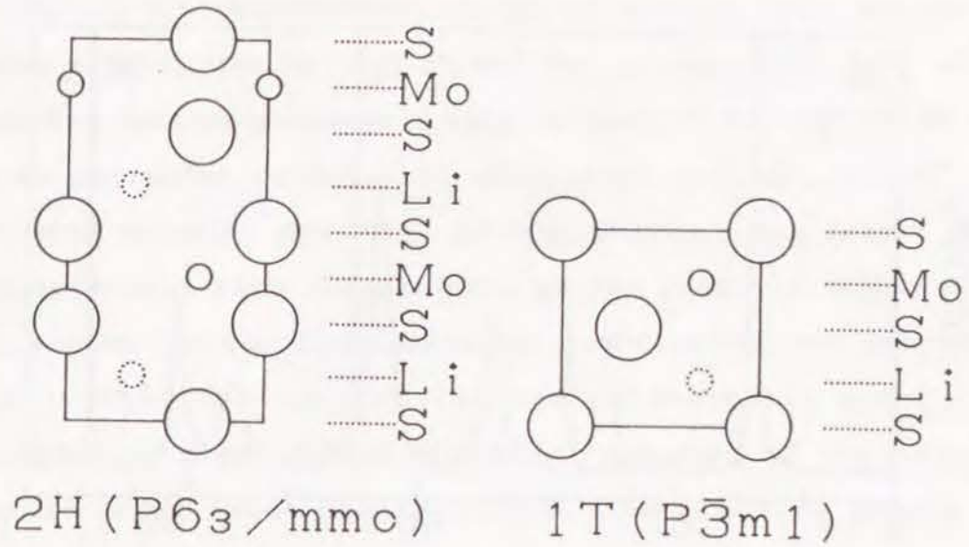

Fig. 2-6 (1120) sections of the structure for 2H- and 1T-MoS_2.

and two higher e'(dxy, dx^2-y^2) and e" (dxz, dyz)groups. When intercalation is occurred, newly added electron must be at the higher energy levels. This leads to the change in the coordination of Mo atom from trigonal prismatic to octahedral[10].

1T-MoS_2 was prepared by the electrochemical delithiation of $Li_{1.12}MoS_2$ prepared by the reaction of MoS_2 with n-butyllithium. The XRD pattern of the prepared sample is shown in Fig. 2-7(a), which is quite different from that of the 2H-type structure. As no X-ray diffraction profile of 1T-MoS_2 has been reported in the JCPDS cards, it was simulated by using the program RIETAN[14]. The conditions of the simulation are as follows; the space group

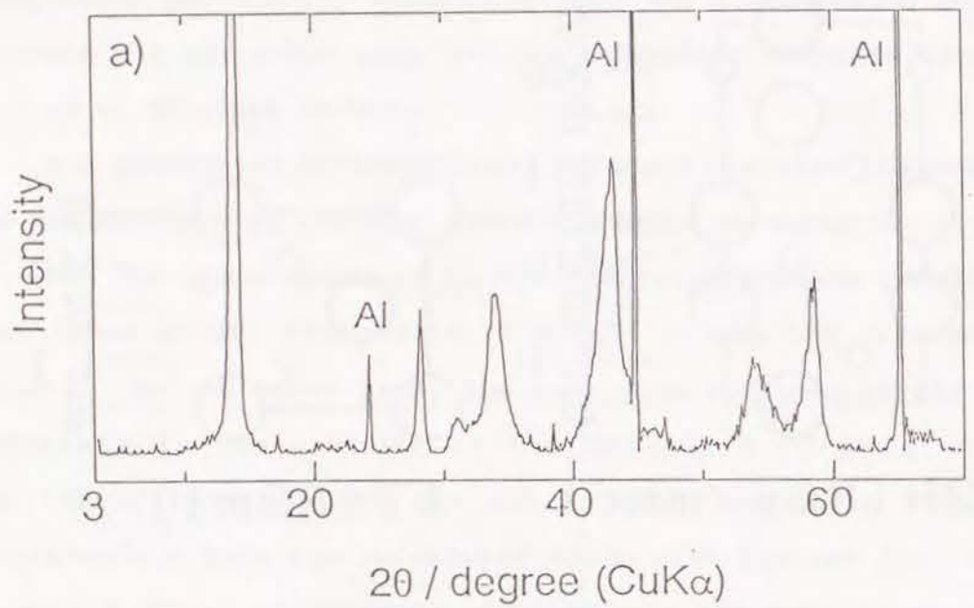

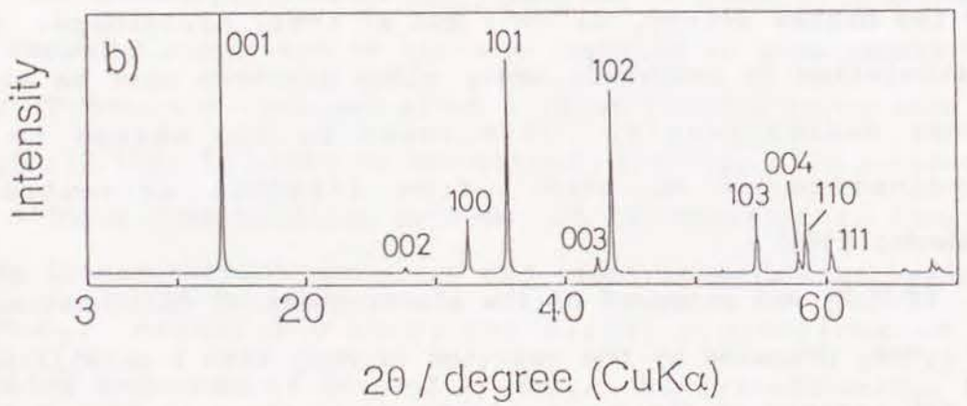

Fig. 2-7 X-ray diffraction patterns of (a) a prepared 1T-MoS_2 and (b) simulated patterns by using a computer.

is P3m1 and equivalent positions for Mo are x=0, y=0, z=0 and for S were x=0.66, y=0.33, z=0.25 and for Li were x=0, y=0, z=0.5, where the lattice parameters were assumed to be same as 2H-MoS_2 and no preferred orientation of crystal was considered. The simulated patterns are shown in Fig. 2-7(b). The result is in good agreement with the patterns of the prepared sample. The main reason for the differences between observed and calculated data is that the applied lattice parameters(a and c) for calculations might differ slightly from ones of the prepared sample. From these consideration, the prepared sample was concluded to be 1T-MoS_2.

Charge-discharge characteristics of 1T-MoS_2 were measured at 200 μAcm^{-2} in PC-DME. As shown in Fig. 2-8, the cycling

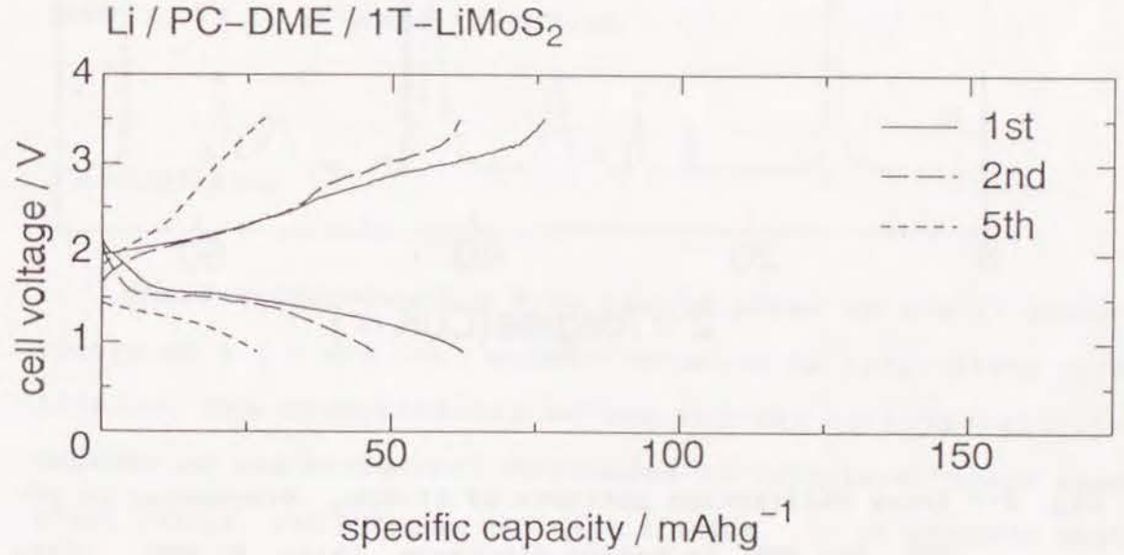

Fig. 2-8 The first five charge-discharge cycles of a Li/1T-MoS_2 cell. 1M $LiClO_4$/PC-DME.

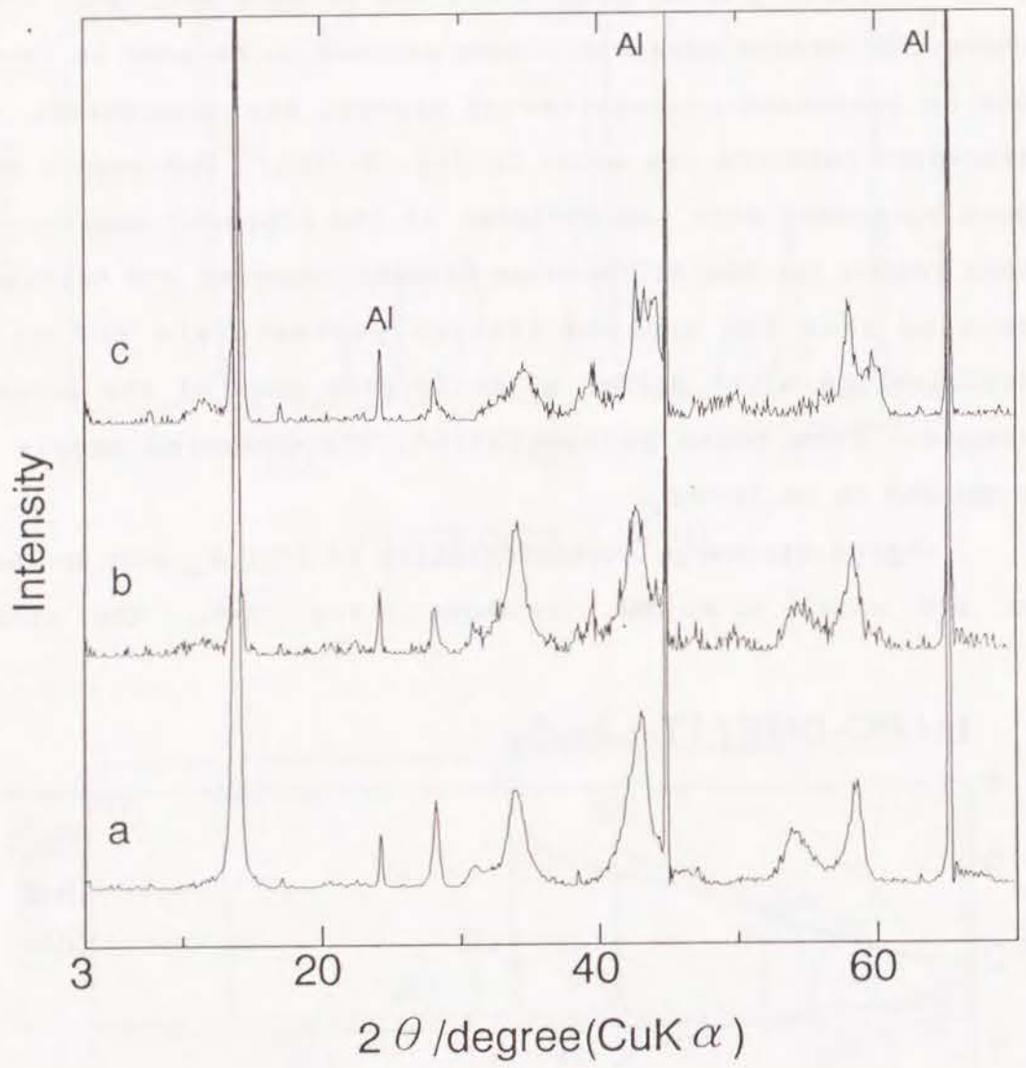

Fig. 2-9 X-ray diffraction patterns of 1T-MoS_2 discharged in PC-DME and DME. (a)before discharge, (b)in PC-DME, (c)in DME.

efficiency was over 80% at the 1st cycle, but the capacity of the each process was only 50 % of the theoretical one. It is worth while to note that the cycling behaviors are much similar to the 2nd and following cycles of the Li/2H-MoS_2 cell in DME solvent. This suggests that the phase transformation from 2H to 1T phase occurs during the 1st discharge process. XRD patterns of 1T-MoS_2 discharged in PC-DME and DME solvents are shown in Fig. 2-9. No extra peak due to the solvent intercalation is observed for both electrolytes. It is suggested that electrolyte solvent does not intercalate into the interlayer space of 1T-MoS_2. Moreover, the large structural change such as the phase transformation also does not occur. We conclude from these results that the electrolyte solvent can co-intercalates only at the period of sliding process of atomic layers in 2H-MoS_2, that is, 2H to 1T phase transition.

2.4 Conclusion

Phase transformation from the 2H phase to the 1T phase occurs at 1.1 V and the solvent molecule co-intercalate with lithium. The reversibility of the solvent co-intercalation depends on its character. PC remains in interlayer space even after charge, but DME goes out with lithium. It is possible that reduction of PC molecule occurs in interlayer space, because PC is comparatively reducible easily. The solvent molecule does not intercalate into the interlayer space of 1T-MoS_2.

References

1. J.J.Auborn, Y.L.Barberio, K.J.Hanson, D.M.Schleich, and M.J.Martin, J.Electrochem.Soc., 134, 580(1987).
2. A.J.Jacobson, R.R.Chianelli, and M.S.Whittingham, J.Electrochem.Soc., 126, 2277(1979).
3. M.S.Whittingham and R.Gamble, Mat.Res.Bull, 10, 363(1975).
4. F.C.Laman, J.A.R.Stiles, R.J.Shank, and K.Brandt, J.Power Sources, 14, 201(1985).
5. D.Ilic, K.Wiesener, and W.Schneider, J.Power Sources, 14, 223(1985).
6. M.A.Py and R.R.Haering, Can.J.Phys., 61, 76(1983).
7. F.C.Laman, M.W.Matsen, and J.A.R.Stiles, J.Electrochem.Soc., 133, 2441(1986).
8. J.A.R.Stiles, New Materials and New Processes, 3, 89(1985).
9. M.W.Juzkow and I.D.Gay, J.Phys.Chem., 95, 9911(1991).
10. E.Sandre, R.Brec, and J.Rouxel, J.Solid State Chem., 88, 269(1990).
11. P.J.Mulhern, Can.J.Phys., 67, 1049(1989).
12. C.Julien, T.Sekine, and M.Balkanski, J.Electrochem.Soc., 48, 225(1991).
13. K.Chrissafis, M.Zamani, K.Kambas, J.Stoemenos, and N.A.Economou, Materials Science and Engineering, B3, 145(1989).
14 F.Izumi, J.Mineral Soc.Jpn., 17, 37(1985).

Chapter 3. Characteristics of Modified FeOCl Containing Organic Compounds in the Interlayer Space.

3.1 Introduction

Layered compounds have been developed as cathode materials for lithium secondary batteries. For example, the transition metal dichalcogenides, TiS_2, MoS_2, $NbSe_2$, etc., are well known [1] and so far, most investigations have been concentrated on their electrochemical and chemical properties.

Oxyhalides of the transition metals, for example, FeOCl and VOCl, are also layered compounds. The intercalation of lithium into FeOCl has been investigated by some workers and it is supposed that the structure of FeOCl intercalated by lithium ions unstable and decomposes[2,3,4]. The discharge products of FeOCl, confirmed by X-ray diffraction, are α-Fe, LiCl, and Li_2O[2]. Though FeOCl can be used as lithium primary battery cathode material it cannot be used for a lithium secondary battery.

In this study, FeOCl modified by the addition of various organic compounds has been investigated in an attempt to improve its stability when intercalated by lithium.

3.2 Experimental

FeOCl was prepared by heating a mixture of α-Fe_2O_3 and $FeCl_3$ in a sealed glass tube[4] and then modified by the intercalation of a basic organic compound. This was carried out as follows: acetone containing FeOCl and one of each of the organic compounds 4-aminopyridine(4-AP), pyridine(PY), pyradine(PA), and 2-vinylpyridine(2-VP) were heated in sealed Pyrex tubes at 80-100 °C. The interlayer distances of the modified FeOCl were larger than that of FeOCl itself, and are summarized in Table 3-1. The electronic conductivities of the modified FeOCl were larger than that of FeOCl.

Table 3-1 Interlayer distances of FeOCl intercalated by various organic compounds.

	(010)2θ	Interlayer distance(A)
FeOCl	11.38	7.917
$FeOCl(4\text{-}AP)_{1/4}$	6.38	13.57
$FeOCl(pyridine)_{1/n}$	6.89	12.82
$FeOCl(pyradine)_{1/n}$	6.80	12.99
$FeOCl(2\text{-}VP)_{1/n}$	6.40-6.90	13.80-12.80

A mixture of FeOCl or modified FeOCl, conductive material(acetylene black), and binding material (Teflon), with a weight ratio of 80:15:5, were compressed at a pressure of 3 $toncm^{-2}$. FeOCl and modified FeOCl cathodes were discharged galvanostatically in propylene carbonated containing 1.0 M $LiBF_4$. The stabilities of FeOCl and modified FeOCl intercalated by lithium were examined using X-ray diffraction (XRD) and electron probe microanalysis(EPMA).

3.3 Results and Discussion

Figure 3-1 shows the discharge and charge curves of FeOCl and four kinds of modifies FeOCl. The discharge capacities of FeOCl and FeOCl intercalated by pyradine, FeOCl(PA), were larger than the theoretical capacities calculated from the amount of active material when the intercalation of lithium was the main reaction in the course of the discharge. In this case, the reaction is described as:

$$FeOCl(organic\ compound)+xLi^{+}+xe^{-} = Li_xFeOCl(organic\ compound) \quad (1)$$

However, the FeOCl and FeOCl(PA) intercalated by lithium were unstable and they could not be charged. Therefore, the discharge reaction of FeOCl and FeOCl(PA) will proceed with the decomposition of the discharged compound. The discharge reaction of FeOCl was investigated in ref.1, and it was supposed that the

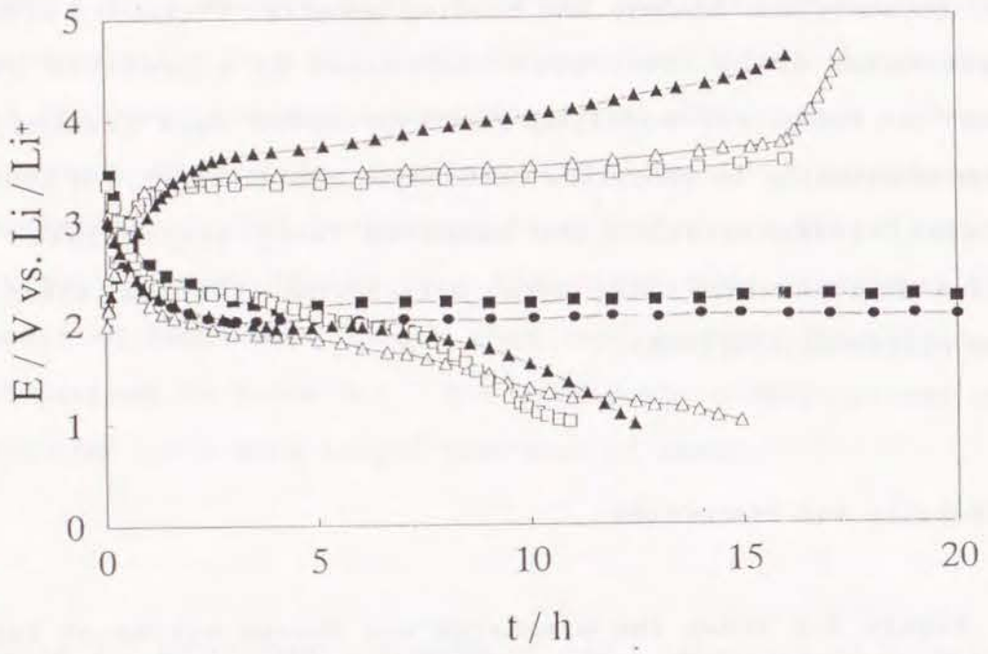

Fig. 3-1 The discharge and charge curves of FeOCl intercalated by 4-aminopyridine(△), pyridine(□), 2-vinylpyridine(▲), pyradine(■), and FeOCl(●) in propylene carbonate containing 1.0 M $LiBF_4$ at $1mAcm^{-2}$.

decomposition compounds were α-Fe, LiCl, and Li_2O. The discharge reaction of FeOCl can be described by the following equation:

$$FeOCl+3Li^{+}+3e^{-} \rightarrow \alpha\text{-}Fe+LiCl+Li_2O \qquad (2)$$

On the other hand, FeOCl intercalated by 4-AP, PY and 2-VP could

be charged after the first discharge. Their discharge capacities were almost in agreement with the theoretical capacities estimated from the intercalation of lithium into them. From these results, it can be seen that some organic compounds intercalated into FeOCl result in the high stability of the discharge compound. Though FeOCl itself cannot be used as cathode material for lithium secondary battery, FeOCl intercalated by an organic compound can.

Figure 3-2 shows X-ray diffraction patterns of FeOCl(4-AP)

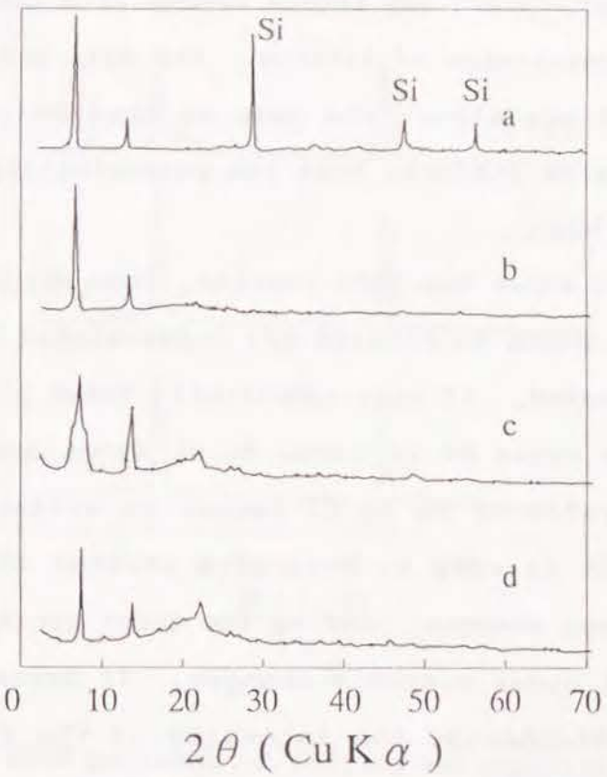

Fig. 3-2 X-ray diffraction patterns of FeOCl(4-aminopyridine) discharged by 20%(a), 50%(b), 100%(c), and after the first cycle(d).

discharged to various degrees, where the degree of discharge was calculated in accordance with reaction(1). The main peak at $2\theta=6.38°$ corresponds to the interlayer distance, which was calculated as 13.57 A. The main peak did not shift during the course of the discharge. It is considered that lithium intercalates into the interlayers of FeOCl(4-AP) without any great structural change. In other words, the stability of FeOCl(4-AP) intercalated by lithium seems to be greater than that of FeOCl. The main peak broadened but it did not shift. The structure of FeOCl(4-AP) may become random with the intercalation of increasing quantities of lithium. The main peak after charge was sharp, and was almost the same as that before discharge. These XRD patterns indicate that the reversibility according to reaction(1) is high.

Figure 3-3 shows the EPMA results, from which the ratio of Fe atoms to Cl atoms in FeOCl(4-AP) intercalated by lithium can be easily estimated. If only reaction(1) takes place during the discharge, the ratio of Fe atoms to Cl atoms does not change. The absolute ratio of Fe to Cl cannot be estimated from EPMA results, but it is easy to determine whether the ratio of Fe atoms to Cl atoms changes. During the first cycle, the ratio of Fe atoms to Cl atoms scarcely changes. If decomposition took place during discharge, the intensity of the Cl atoms would decrease with respect to that of the Fe atoms. By contrast, in the case of FeOCl, the intensity of the Cl atoms does decrease as the discharge proceeds. These facts indicate that lithium is reversibly intercalated into, and deintercalated from

FeOCl(organic compound).

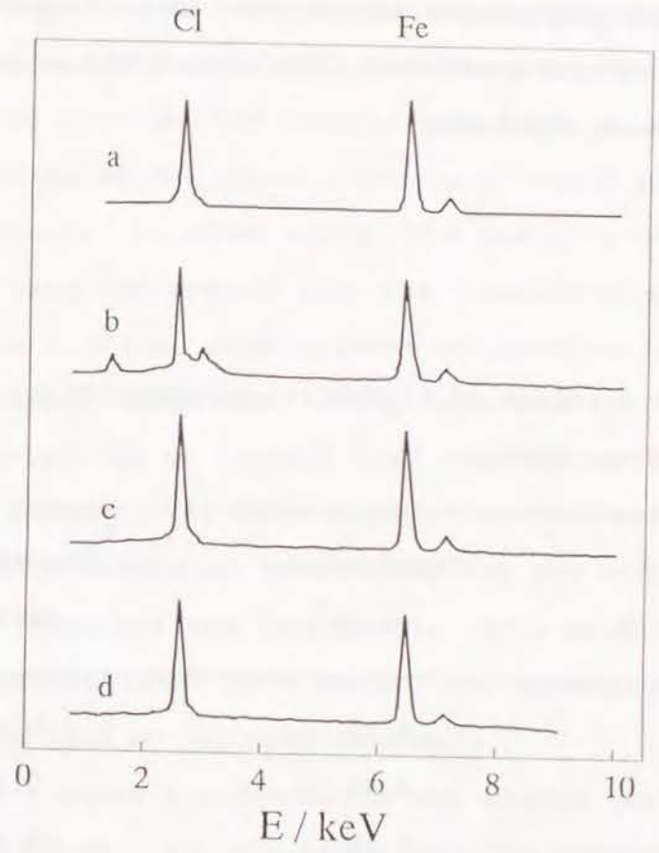

Fig. 3-3 The EPMA patterns of FeOCl(4-aminopyridine) before discharge(a), discharged by 20%(b), discharged by 80%(c), and after the first cycle(d).

In order to confirm the intercalation of lithium into FeOCl(organic compound), the amount of intercalated lithium was measured using an atomic absorption procedure. Table 3-2 gives the experimental values, and also the theoretical values calculated from the quantity of electricity consumed. The experimental and theoretical values were in good agreement. From these results, it is confirmed that only lithium intercalation takes place during discharge.

Table 3-2 The x values of Li_xFeOCl(4-aminopyridine) discharged to various depths.

Depth of discharge(%)	Experimental value*	Theoretical value**
20	0.18	0.20
40	0.33	0.40
60	0.58	0.60
80	0.79	0.80

*From atomic absorption measurement

**From the quantity of electricity consumed

The stability of FeOCl intercalated by lithium was improved by the intercalation of an organic compound. However, FeOCl intercalated by pyradine decomposed as discharge proceeded. Its discharge characteristics were very similar to that of FeOCl. The organic compounds contain a nitrogen atom which has a lone pair of electrons. The charge transfer complex is formed from the organic compounds and FeOCl[5,6]. The characteristics of the charge transfer complex, for example, the bonding energy, depend on the properties of the organic compound, which plays the role or electron donor. In other words, the basicity of the organic compound is very important for the stability of the FeOCl intercalated by lithium. The basicity of pyradine is the weakest of the four organic compounds. It is important for the stability of FeOCl intercalated by lithium that the highest basic organic compound be chosen. In this study, four different organic compounds were intercalated into FeOCl, and the stability of the FeOCl(organic compound) was determined. If a more basic organic compound is intercalated into FeOCl, the discharge and charge characteristics will be improved immensely.

Figure 3-4 shows the discharge and charge curves of FeOCl intercalated by 4-AP. The discharge capacity decreased gradually with increasing cycle number. These results show that the stability of FeOCl(4-AP) decreases with increasing cycle number, and FeOCl(4-AP) decomposes gradually during discharge or charge. Figure 3-5 shows the results of EPMA on FeOCl(4-AP) before the first discharge and after the tenth cycle. The intensity of the Cl atoms after cycling decreased by comparison with that before

cycling. This indicates that decomposition of FeOCl(4-AP) takes place during cycling, with a resultant decrease in the discharge capacity.

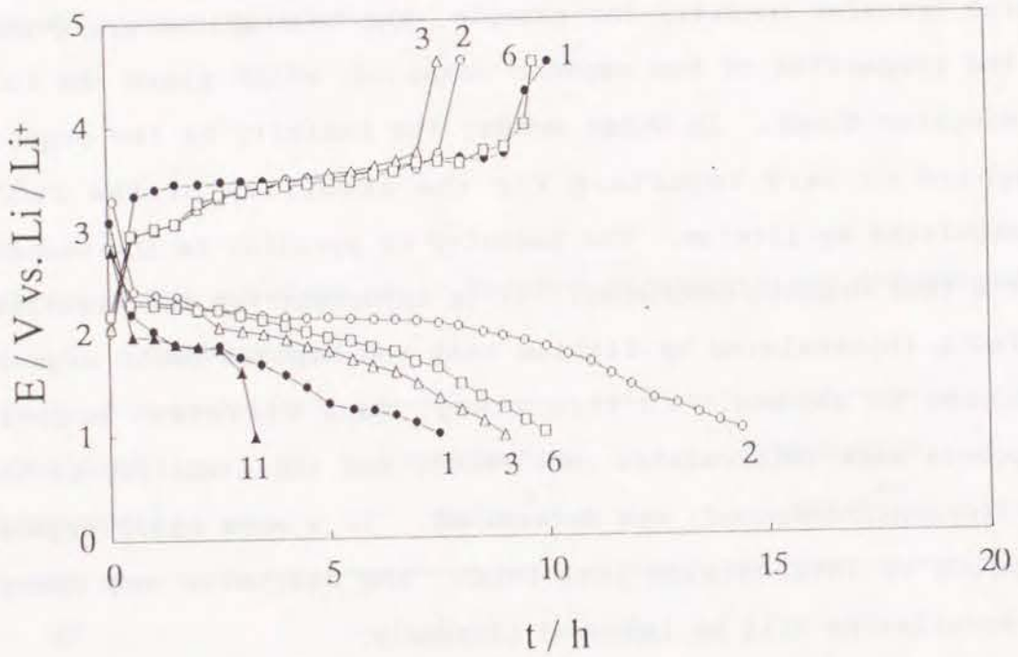

Fig. 3-4 The discharge and charge curves of FeOCl(4-aminopyridine) in propylene carbonate containing 1.0 M $LiBF_4$ at 1.0 $mAcm^{-2}$. The figures by the curves indicate cycle numbers.

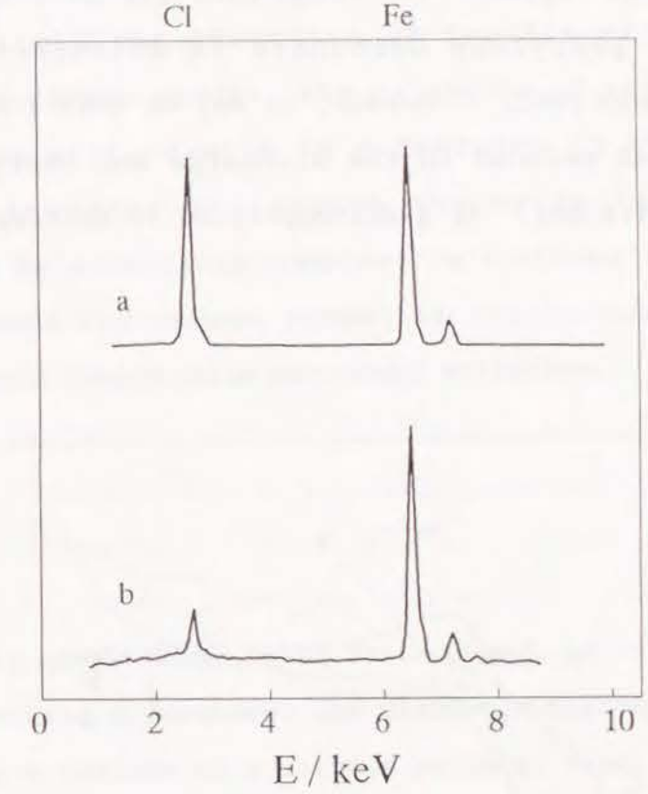

Fig. 3-5 The EPMA patterns of FeOCl(4-aminopyridine) before discharge(a) and after the tenth cycle(b).

Figure 3-6 shows cycling voltammograms of FeOCl(4-AP) and 4-amino-pyridine in propylene carbonate with 1.0 M $LiBF_4$. A Pt plate was used as working electrode for the cyclic voltammetry of 4-amino pyridine. The cyclic voltammogram of FeOCl shows that in addition to the intercalation of lithium into FeOCl(4-AP), other

reactions occur in the discharge and charge potential region. 4-aminopyridine was oxidized and reduced in the discharge and charge potential region. The redox behavior of 4-aminopyridine dissolved in propylene carbonate is different from that intercalated into FeOCl. However, it may be that 4-aminopyridine is oxidized and reduced in the discharge and charge potential region of FeOCl(4-AP). If 4-aminopyridine is oxidized or reduced

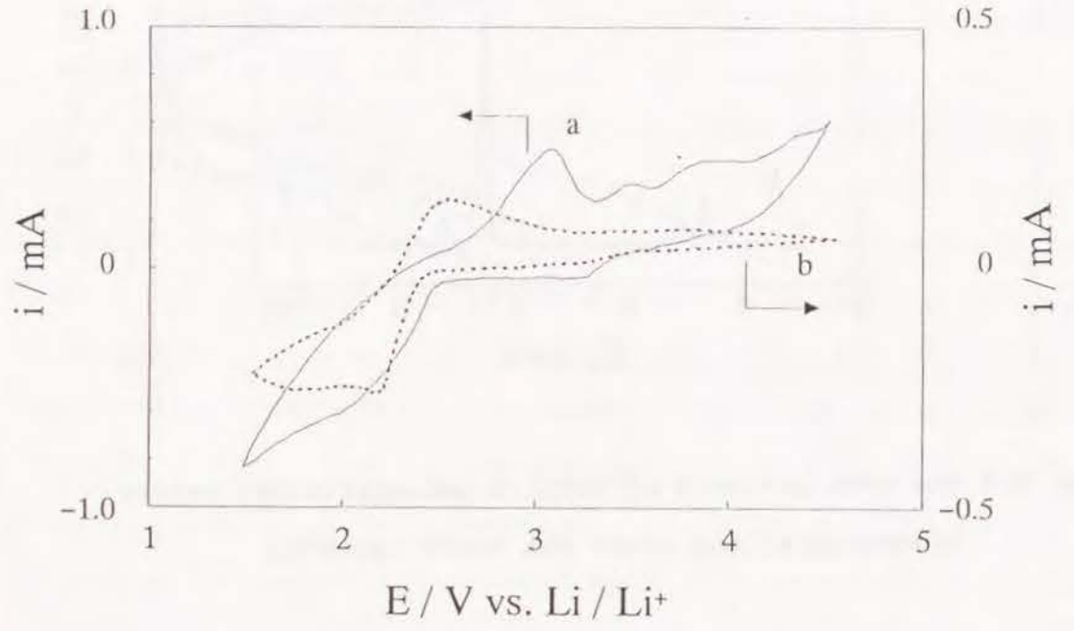

Fig. 3-6 Cyclic voltammograms of FeOCl(4-aminopyridine)(a) and 4-aminopyridine(b) in propylene carbonate containing 1.0 M $LiBF_4$. Sweep rate:(a) $1mVs^{-1}$ (b) 50 mVs^{-1}.

and changes to an inert compound, the discharge and charge characteristics will change in the course of the discharge and charge cycles. Since the organic compound intercalated into FeOCl stabilized the structure of FeOCl(4-AP) during the discharge and charge cycles, the oxidation of reduction of 4-aminopyridine will results in a decrease in the discharge capacity. In order to improve the cycle life of FeOCl intercalated by an organic compound, a compound stable in the FeOCl discharge and charge potential region must be used as cathode material for lithium secondary batteries.

References

1. M.S.Whittingham, Prog. Solid State Chem., 12, 41(1978).
2. K.Kanamura and Z.Takehara, The discharge characteristics of FeOCl as a cathode of a lithium battery, Proc. 27th Battery Symp. Japan, Nov. 1986, Osaka.
3. S.Kikkawa, T.Yamamoto, and M.Koizumi, Yogyo-Kyokai-Shi, 93, 47(1985).
4. H.Meyer, A.Weiss, and J.O.Besenhard, Mater.Res.Bull., 13, 913(1978).
5. S.Kikkawa, F.Kanamaru, and M.Koizumi, Inorg.Chem., 15, 2195(1976).
6. S.Kikkawa, F.Kanamaru, and M.Koizumi, Bull.Chem.Soc.Jpn., 52, 963(1979).

Chapter 4. Characteristics of Defect Thiospinel Compounds Having Three Dimensional Lithium Diffusion Paths.

4.1 Introduction

The high rate rechargeability is the important factor of a cathode material for lithium secondary batteries. Some oxides and sulfides having a spinel structure have been investigated as a cathode for a lithium secondary battery with high power density[1-3]. The spinel structure has three dimensional interstitial sites as pathways of lithium diffusion. However, the diffusion rate of lithium ions into the oxide spinels is generally small. The bottle neck size via 8a and 16c sites is too small for lithium diffusion in an oxide framework, and A-site cations prevent the three dimensional diffusion in the host lattice[4].

Recent papers have reported the lithium diffusion in a large number of other type of spinel structures, for example, chloride-spinels[5] and chalcogenide-spinels[4]. In these compounds, the bottle neck size formed by the anions is larger than in the oxide spinels. If the immobile A-site cations can be removed from the lattice, these compounds can be expected to show the higher lithium ion mobility.

There are only a few studies about the electrochemical properties of the thiospinels as a cathode for a lithium

secondary battery, although a large number of varieties of spinel compounds are known. In this study, we tried to synthesize the defect thiospinel compounds which have the formula of $Cu_xM_2S_4$ (M=Ti, Cr)[4,6]. Then, its possibility as a rechargeable cathode with high power density, was discussed.

4.2 Experimental

$CuTi_2S_4$ and $CuCr_2S_4$ were prepared from the each element. Stoichiometric amount of elements were mixed and sealed in an evacuated silica tube. In order to prepare $CuTi_2S_4$, the mixture was kept at 400°C for 3 days, then heated again at 700°C for 3 days. The extraction of the copper atom was carried out by oxidation at 60°C for 3 weeks using I_2/CH_3CN solution. The copper and titanium ratio was determined by the atomic absorption method and the limiting composition was determined to be $Cu_{0.18}Ti_2S_4$. In the case of $CuCr_2S_4$, the silica tube was heated at 400 °C for 1 day, then heated again at 700°C for 3 days. The products were ground once, then heated in vacuum at 700°C for 3 days. The copper extraction from $CuCr_2S_4$ by the oxidation with the I_2/CH_3CN did not succeed. Then, an ion exchange with lithium was attempted by reaction with 1.6 M n-butyllithium in hexane at room temperature.

Charge-discharge tests were carried out by using a coin-type cell which has been described in Chapter 2. 70 mg of cathode material and 2 mg of PTFE were mixed and pressed under 10 MPa

pressure into a tablet with an 8 mm diameter. A lithium sheet of 0.34 mm thickness was used as an anode. The electrolyte was a solution of 1 M $LiClO_4$ dissolved in a mixture of propylene carbonate(PC) and dimethoxyethane(DME) solvent.

4.3 Results and Discussion

The $Cu_xTi_2S_4$ was obtained as a single phase for a composition range of $0.18<x<1.0$ as shown in Fig. 4-1. The (220) diffraction peak indicating the existence of cations at the 8a sites of the spinel framework decreases with the oxidation and almost diminishes in $Cu_{0.18}Ti_2S_4$. This behavior clearly indicates that the copper atom is removed from the spinel lattice by the chemical oxidation.

Figure 4-2 shows the discharge curve of $Cu_{0.18}Ti_2S_4$ at various current densities and open circuit voltage(OCV) curves for charge and discharge processes. The $Cu_{0.18}Ti_2S_4$ shows a stable voltage of about 2 V for a composition range of $0<x<1.2$ in $Li_xCu_{0.18}Ti_2S_4$. No significant degradation of discharge behavior was observed for the applied current densities below 3 $mAcm^{-2}$. The coulomb density at 0.2 $mAcm^{-2}$ is 177 $mAhg^{-1}$ based on a 1.0 V cut off. The OCV curves show the typical S-shaped profile indicating the reaction of single phase, that is, a formation of a lithium-thiospinel solid solution. The OCV curves of discharge and charge directions show almost the same profile over the whole range of x. This means that smooth lithium insertion and

extraction occur in both processes.

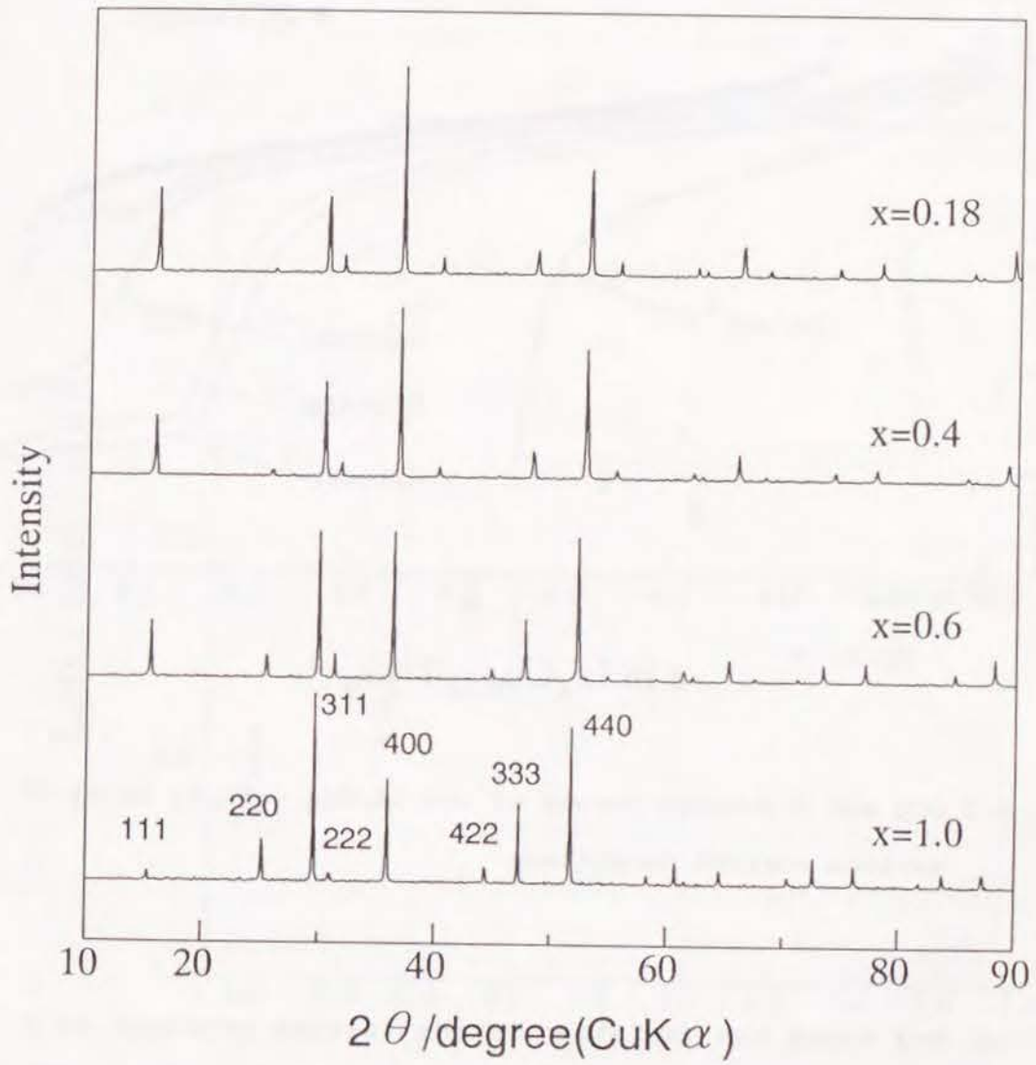

Fig. 4-1 XRD patterns of $Cu_xTi_2S_4$ at various oxidation states.

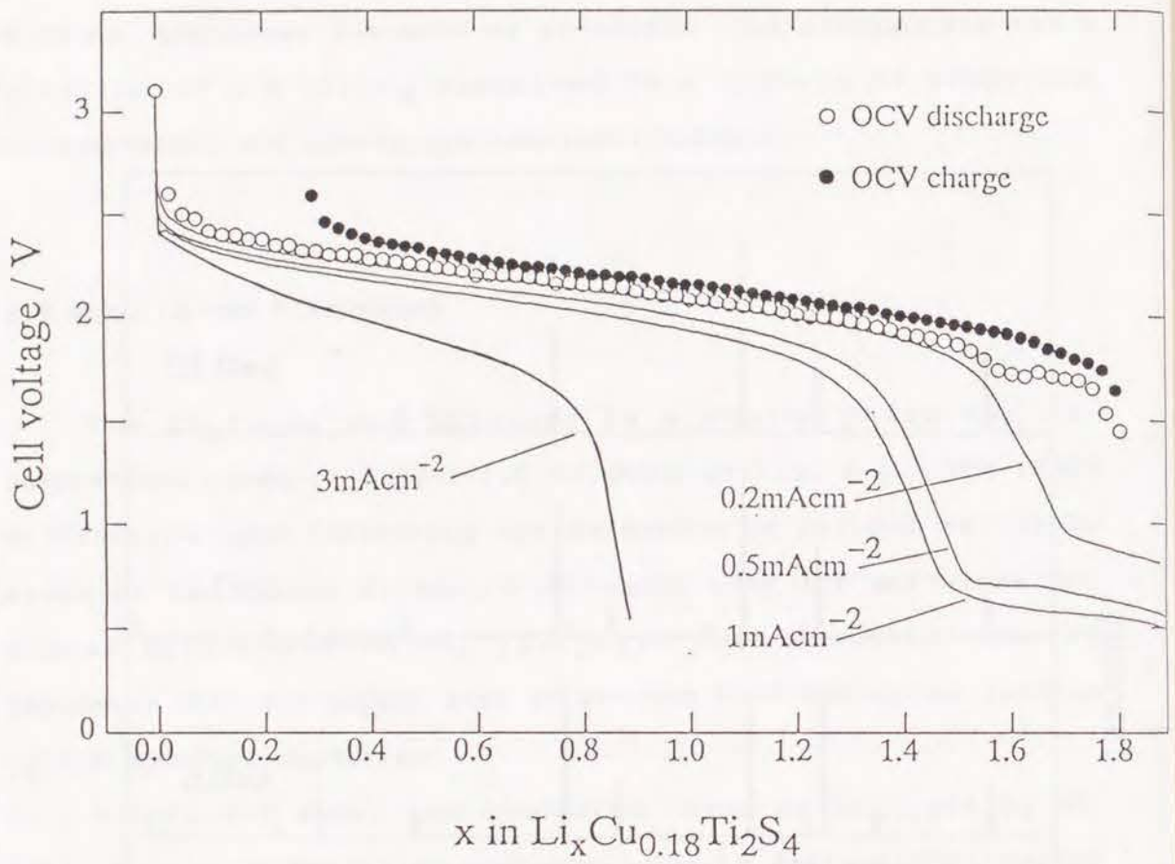

Fig. 4-2 OCV and discharge curves of the Li/$Cu_{0.18}Ti_2S_4$ cells at various current densities.

Fig. 4-3 shows the variation of the lattice constant as a function of x in $Li_xCu_{0.18}Ti_2S_4$ for both the discharge and charge processes on cycling. The a-axis linearly increases with the

discharge capacity, which results in a 7.8 % expansion in volume of the unit cell at x=1.8. At the charge side, the perfect recovery of the lattice constant is observed. This compound shows reversible lattice expansion and contraction on cycling.

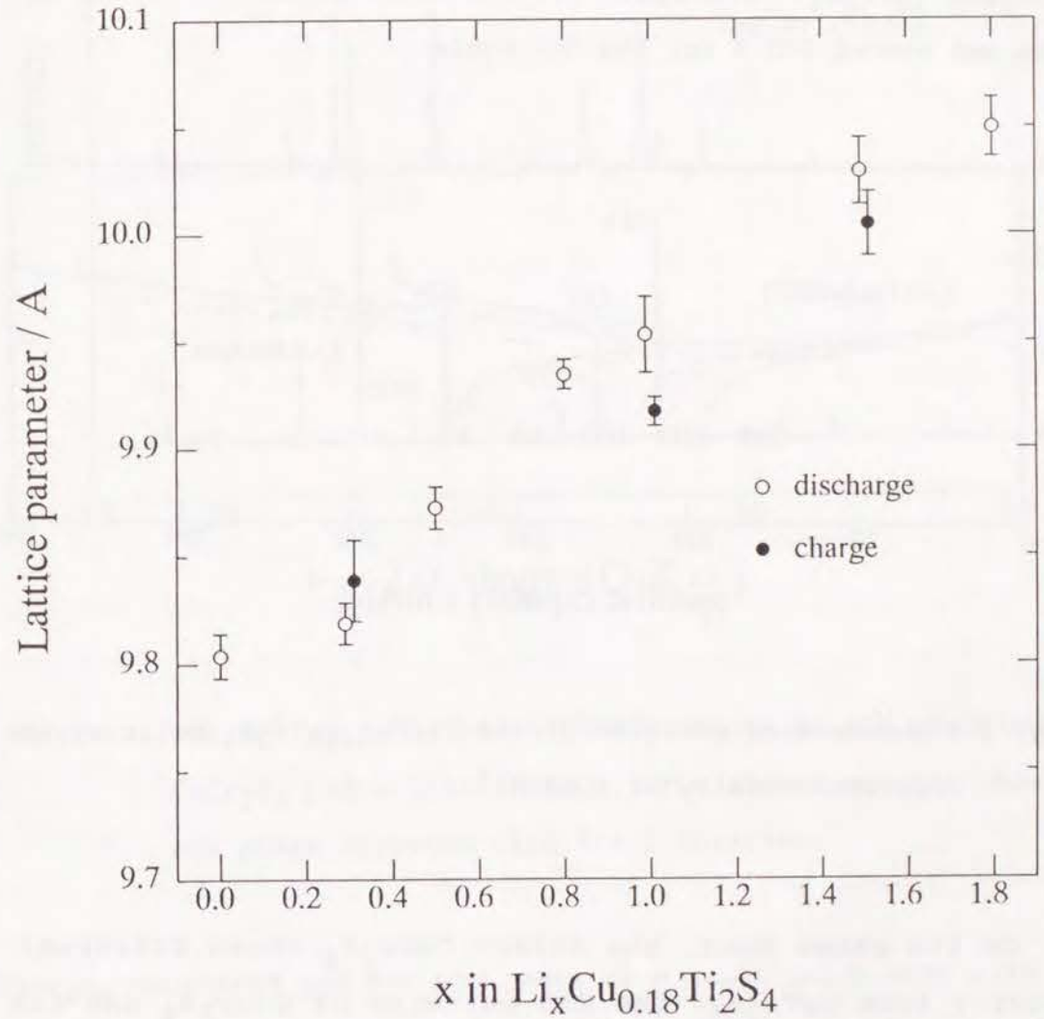

Fig. 4-3 The variation of the lattice parameter of the $Li_xCu_{0.18}Ti_2S_4$ on the 1st charge-discharge cycle.

Figure 4-4 shows cycling behaviors of the $Li/Li_xCu_{0.18}Ti_2S_4$ cell. The cycling test was carried out between 3.0 and 1.2 V at the current densities of 1 $mAcm^{-2}$. The coulomb densities of the 1st cycle are about 170 and 130 $mAhg^{-1}$ for the discharge and charge process, respectively, which correspond to x=1.5 and 1.2 in $Li_xCu_{0.18}Ti_2S_4$. The cycle efficiencies are 80 % for the 1st cycle and almost 100 % for the 5th cycle.

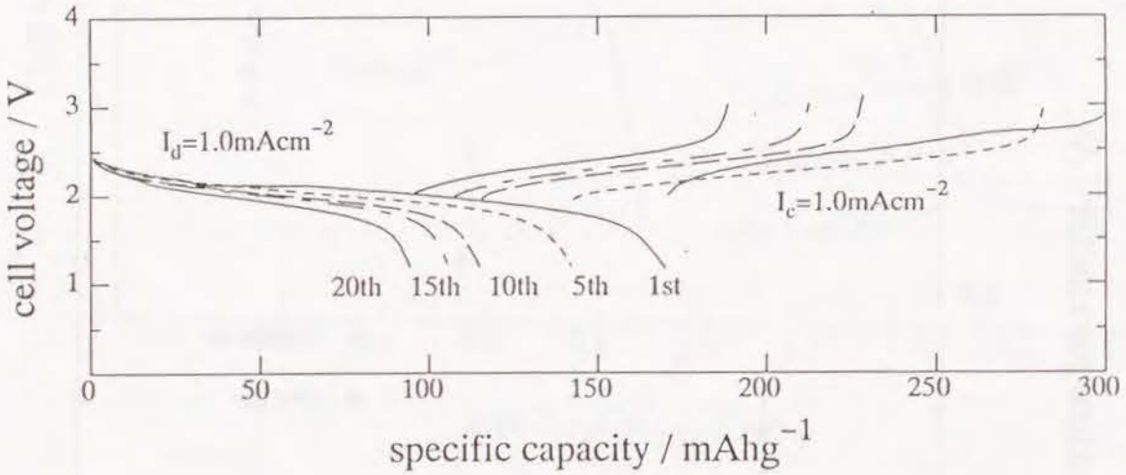

Fig. 4-4 The cycling profiles of the $Li/Cu_{0.18}Ti_2S_4$ cells at the current density of 1 $mAcm^{-2}$.

On the other hand, the defect $CuCr_2S_4$ shows different behavior from $CuTi_2S_4$. The XRD patterns of $CuCr_2S_4$ and its lithiated phase marked by the closed circles are shown in Fig. 4-5. Silicon powder was used as the internal standard material. As the reaction with n-butyllithium proceeds, the intensity of

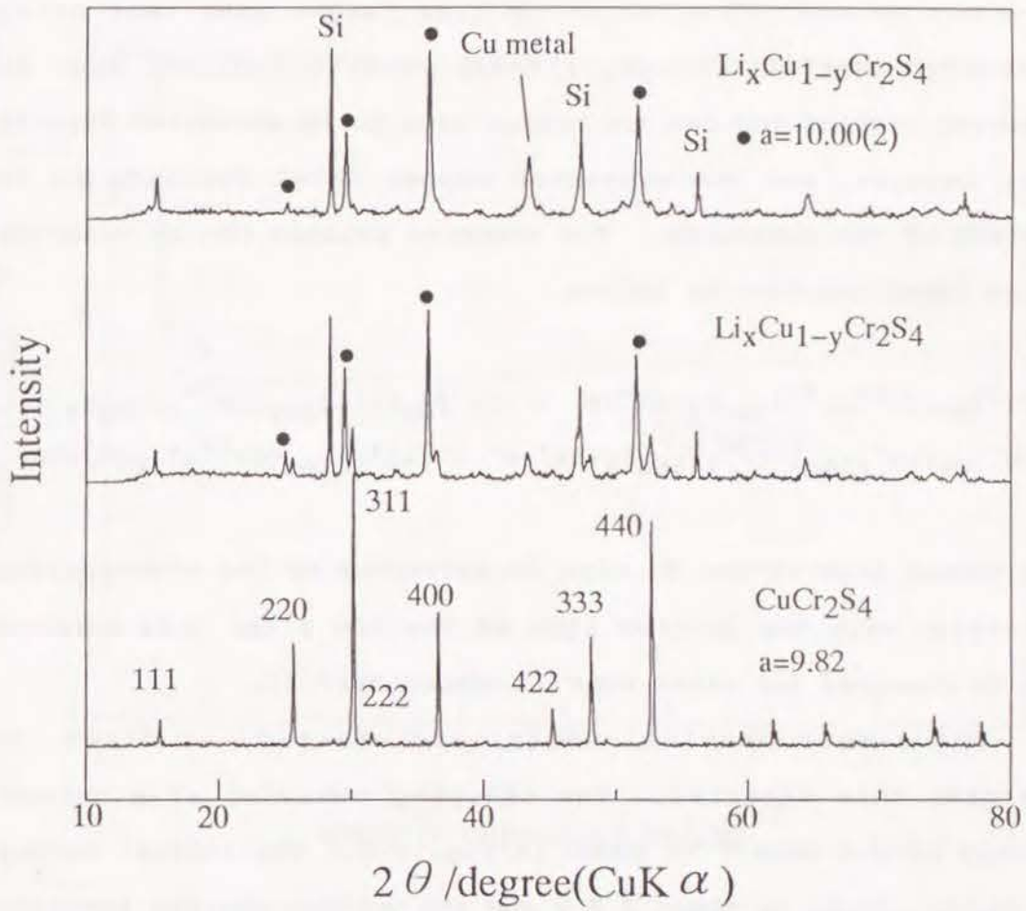

Fig. 4-5 The XRD patterns of reduced products by the reaction of $CuCr_2S_4$ and n-butyllithium. The closed circles show a new phase appeared with the lithiation.

$CuCr_2S_4$ decreases and the new peaks of a cubic phase with a=10.00 A increases. At the same time, the peaks of copper metal appears. The new cubic phase marked by closed circles is considered to be a lithiated spinel, $Li_xCu_{1-y}Cr_2S_4$. The lattice

constant is a=10.00 A, which is 1.8% larger than that of the starting material, $CuCr_2S_4$. These results indicate that the inserted lithium induces the copper atom to be extracted from the host lattice, and the extracted copper metal deposits on the surface of the compounds. The reaction process can be described in an idealized form as follow,

$$\{Cu^+\}_{8a}\{Cr^{3+}Cr^{4+}\}_{16d}S_4+Li^++e^- = \{Cu^+\}_{8a}\{Li^+\}_{16c}\{Cr^{3+}{}_2\}_{16d}S_4$$

$$\{Cu^+\}_{8a}\{Li^+\}_{16c}\{Cr^{3+}{}_2\}_{16d}S_4+Li^++e^- = \{Li^+{}_2\}_{16c}\{Cr^{3+}{}_2\}_{16d}S_4+Cu$$

The copper atom at the 8a site is extracted by the electrostatic repulsion with the lithium atom at the 16c site. This behavior can be observed for other type of compounds[7,8].

The electrochemical tests were started, at first, by charging this material. The charging behavior at a current density of 0.2 $mAcm^{-2}$ is shown in Fig. 4-6. The initial voltage of $Li_xCu_{1-y}Cr_2S_4$ is about 2.8 V and the voltage sharply increases up to 4.0 V just after the charge process starts. Then the voltage drops again and shows a plateau at 2.6 V. The total voltage profile is similar to that of $Cu_xTi_2S_4$ except for the initial voltage overshoot. However, the following discharge profile is impossible to measure because the polarization becomes too large. In order to clarify the reason for irreversibility of $Li_xCu_{1-y}Cr_2S_4$, XRD measurements were carried out for samples charged at several states, which are indicated as A, B, and C on the charge curve in Fig. 4-6.

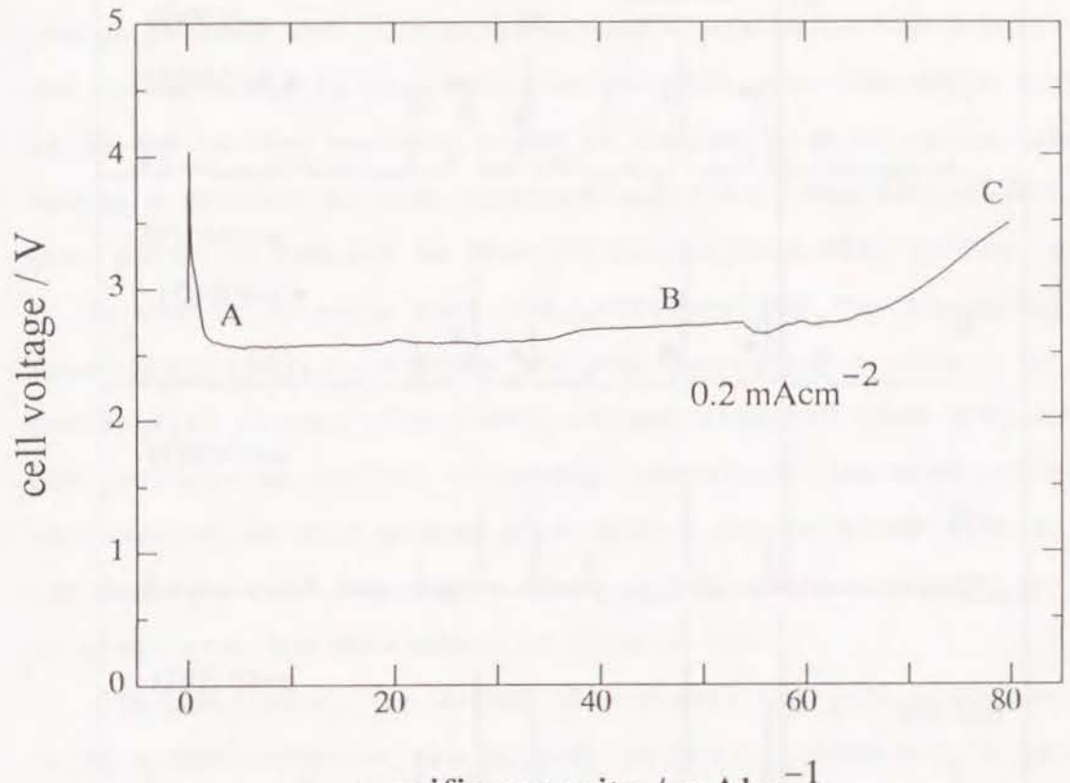

Fig. 4-6 The charge curve of the Li/$Li_xCu_{1-y}Cr_2S_4$ cell at the current density of 0.2 $mAcm^{-2}$.

Figure 4-7 shows the XRD patterns of the indicated A, B, and C stages on the charge curve. The starting material before charging shows a strong copper peak corresponding to copper metal

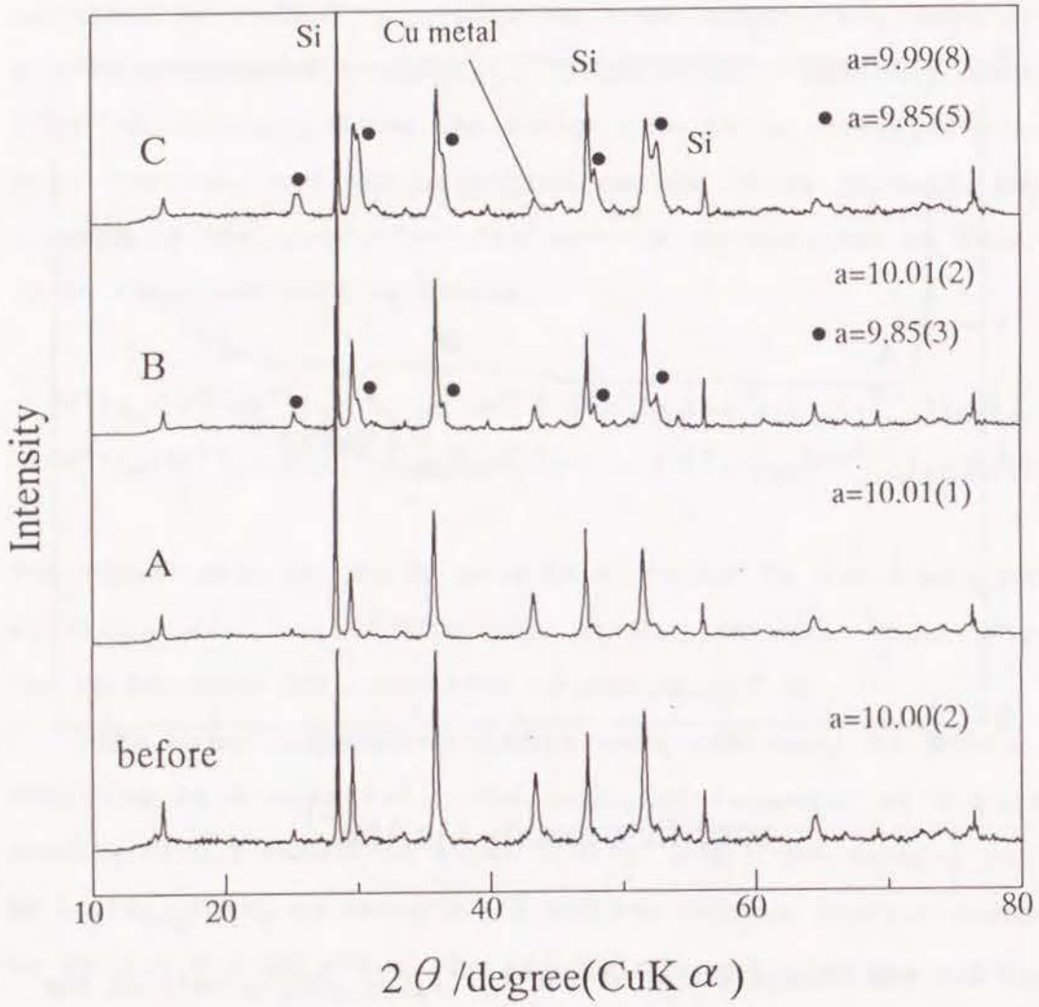

Fig. 4-7 The XRD patterns of $Li_xCu_{1-y}Cr_2S_4$ at several charged states. The closed circles show the spinel, $CuCr_2S_4$.

deposited on the surface. The intensity decreases along the charge process and the peaks almost diminish at the C point of the charge curve in Fig. 4-6. In addition, the new phase marked by closed circles appears, which is indexed as a thiospinel phase having a smaller lattice constant(a=9.85A). The XRD pattern of this phase is similar to that of $CuCr_2S_4$(a=9.82A) in Fig. 4-5. It is worthy to note that the (220) peak of the new phase at around 25°(2θ) indicates the existence of a cation on 8a tetrahedral sites. The light lithium atom can give only small contribution to the XRD intensity, therefore, the most probable explanation is that copper atom occupy the 8a sites. Thus, we can conclude that the copper metal on the surface returns to the 8a sites with the extraction of lithium ion.

In conclusion, the defect thiospinel, $Cu_{0.18}Ti_2S_4$ is proved to be a candidate for the cathode material, which can be cycled at the high current density. However, it is important to remove the copper atom in advance. The residual copper in the lattice prevents the smooth diffusion of lithium ions and, therefore, the smooth charge-discharge reaction.

References

1. M.M.Thackeray, A de Kock, M.H.Rossouw, D.Liles, R.Bittihn, and D.Hoge, J.Electrochem.Soc., 139, 363(1992).
2. R.Kanno, Y.Kawamoto, Y.Takeda, M.Hasegawa, and O.Yamamoto, Solid State Ionics, 40/41, 576(1990).

3. B.Zachau-Christiansen, K.West, T.Jacobsen, and S.Atlung, Solid State Ionics, 40/41, 580(1990).
4. A.C.W.P.James and J.B.Goodenough, Solid State Ionics, 27, 37(1988).
5. R.Kanno, Y.Takeda, K.Takeda, and O.Yamamoto, J.Electrochem.Soc., 131, 469(1984).
6. R.Schollhorn and A.Payer, Anew. Chem. Int. Ed. Engl., 24, 67(1985).
7. Y.Takeda, K.Itoh, R.Kanno, T.Ichikawa, N.Imanishi, and O.Yamamoto, J.Electrochem.Soc., 138, 2567(1991).
8. Y.Takeda, R.Kanno, M.Noda, and O.Yamamoto, Mat.Res.Bull., 20, 71(1985).

Chapter 5. Characteristics of Brannerite-Type $CuV_{2-x}Mo_xO_6(0<x<1)$ Cathodes.

5.1 Introduction

Vanadium pentaoxide has been of special interest in an active cathode material for rechargeable lithium cells[1] because of its open structure and high valence state of vanadium ions. However, the cycle life is not adequate when the discharge proceeds to the +4 state of vanadium[2]. To overcome this disadvantage and to improve the rechargeability, various modified systems related to vanadium oxides have been tried as cathode materials for lithium secondary batteries. These include V_6O_{13}[3,4], LiV_3O_8[5], amorphous V_2O_5-P_2O_5[6], $V_9Mo_6O_{40}$[7], and Wadsley-Roth phases[8,9].

Among them, the Cu-V-O systems have been extensively studied by the NTT group in Japan[10]. These copper vanadates which are CuV_2O_6, $Cu_2V_2O_7$, and $Cu_5V_2O_{10}$, exhibit good electrode properties in both energy density and cycle performance. One of them, CuV_2O_6, has been known to have the brannerite-type structure and to form a series of divalent metal vanadates $M^{2+}V_2O_6$(M=Mg, Ca, Mn, Co, Ni, Zn, Cd) by replacing the copper with another divalent metal ion[11]. We were interested in the electrode behavior of these metavanadates in lithium cells compared to the copper vanadate, CuV_2O_6. However, all the divalent metal vanadates

except for CuV_2O_6 showed only very poor electrochemical properties in spite of their similar crystal structures[12]. The difference in electrode capacity between CuV_2O_6 and other MV_2O_6 compounds has long been puzzling to the present authors. We suppose that the higher redox potential of copper compared to other divalent ions in MV_2O_6 is one of the reasons why only CuV_2O_6 shows good electrode properties; that is, the Cu^{2+} state in CuV_2O_6 can be easily reduced to Cu^+ and/or Cu metal state by reaction with Li^+. A displacement of copper by lithium often occurs in copper intercalated electrodes. Examples are the Li/Copper Chevrel-phase, $Cu_xMo_6S_8$, couple[13]

$$Cu_xMo_6S_8 + xLi \rightarrow Li_xMo_6S_8 + x\ Cu$$

and also the Li/Cu-V-O oxide couples[10].

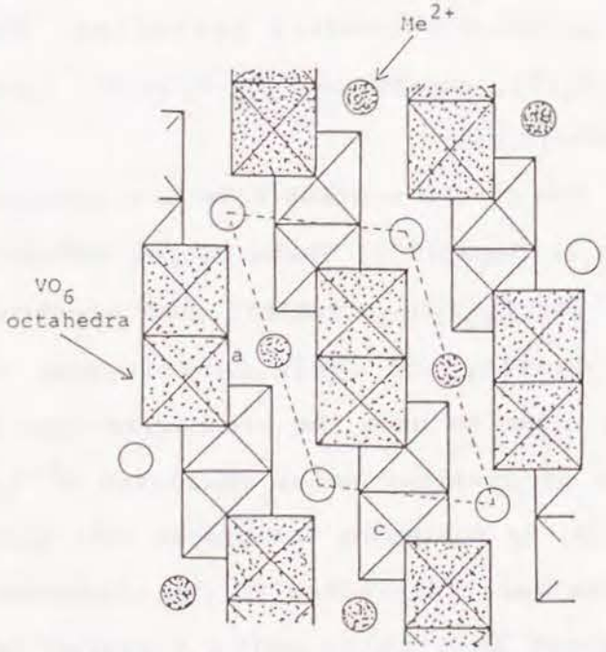

Fig 5-1 Idealized projection of the brannerite type structure MV_2O_6 on the (010) plane with M^{2+} cations and VO_6 octahedra on two levels (after Mocala et al (15))

As shown in Fig. 5-1, the brannerite-type structure is composed of anionic sheets of VO_6 octahedra sharing three edges, and M^{2+} ions in octahedral interlayer positions binding the VO_6 sheets together. The introduction of Cu^{2+} ions into the M^{2+} sites leads to a strong Jahn-Teller distortion by which the structure of CuV_2O_6 is deformed from a monoclinic symmetry in the normal brannerite-type oxide to a triclinic one. By replacing pentavalent V^{5+} ions with hexavalent Mo^{6+} ions, monovalent Cu^+ ions can be accommodated in the structure. When Mo^{6+} ions substituted half of the vanadium positions, all of the copper ions are reduced to the monovalent state. It is interesting to see the electrode behavior, especially the intercalation and deintercalation of Li and Cu ions in the materials containing the different oxidation states of copper. Substituted samples have been already prepared by Machej et al.[14], but due to their synthesis in air they contain vacancies at Cu^{2+} sites, which is why they have a complex formula $Cu^{2+}{}_{1-x-y}Cu^{1+}{}_y\Phi^\circ{}_xV_{2-2x-y}Mo_{2x+y}O_6$ ($x_{max}=0.233$, $y_{max}=0.27$) where $\Phi^\circ{}_x$ represents a vacancy at the Cu^{2+}site. To suppress the oxidation of copper, we tried to prepare the $Cu^{2+}{}_{1-x}Cu^{1+}{}_xV_{2-x}Mo_xO_6$ solid solution with controlled composition in a closed system such as a sealed silica tube where oxygen cannot come in and out. The solid solution in the range of $0<x<1.0$ was obtained as a single phase. The structural changes and electrochemical behavior were studied using these materials as the cathode in lithium cells.

5.2 Experimental

$CuV_{2-x}Mo_xO_6$(0<x<1.0) samples were prepared by heating a well-mixed mixture of CuO, V_2O_5, MoO_3 and Mo metal in a sealed evacuated silica tube for three days at 600 °C(0<x<0.7) or 500 °C (0.8<x<1.0). The melting points for the samples with x=0.8-1.0 was lower than 600 °C. The MoO_3/Mo mixing ratio was used to control the oxygen content of $CuV_{2-x}Mo_xO_6$. The products were identified by the x-ray diffraction(XRD) on Rigaku RAD-RC(12 kW) using monochromated CuKα radiation and a scintillation detector. The lithiated samples were protected against moisture during the XRD measurements by using a gas-tight holder filled with argon gas. A 7 μm thick aluminum window covered the sample holder plate in a arc. The discharge and charge tests were performed in coin cells which has been described in Chapter 2. The anode was a lithium foil disk of 14 mm diam. and 0.24 mm thickness. The separator was a microporous polypropylene sheet. The cathode comprised a mixture of 0.05 g of the oxide, 0.015 g of acetylene black and 0.0015 g of Teflon powder; they were pressed into a tablet 11.5 mm in diam. The electrolyte was 1M $LiClO_4$ in a 1:1 by weight mixture of propylene carbonate and 1.2-dimethoxyethan, which was supplied by Mitsubishi Petrochemical Company. All the electrochemical measurements were carried out at room temperature after an overnight stand at zero current. Quasi-open-circuit voltages (OCV) were measured by alternating a discharge or charge(0.1 mA/cm^2, 1h) and rest (7h) period. The cell voltages then measured were considered as quasi-OCV because

the change in the measured cell voltage was less than 1 mV/1h.

5.3 Results and Discussion

5.3.1. Relationship between structural characteristics and discharge-charge processes.

Because of the vacuum-sealed preparation of the samples, a wide range of Mo substitution for V in CuV_2O_6 was possible. The XRD patterns of all samples of $CuV_{2-x}Mo_xO_6$ in the x range 0-1.0 were completely indexed as the brannerite-type structure. For x>1, impurities such as MoO_3 remained. The lattice parameters calculated by using the program RSLC-3[15] are listed in Table 5-1 and the variations with composition are shown in Fig 5-2. The degree of the triclinic distortion decreases with the introduction of Mo, which corresponds to an increase of Cu^+ content and the structure changed to monoclinic at x=0.6. This change in symmetry may be due to the decrease of Jahn-Teller Cu^{2+} ions.

All the materials showed semiconductive character from room temperature to 15K. Their resistivities at room temperature, as measured by a four probe-method, exhibited fairly low values, $1.13x10^2$(x=0), $0.15x10^2$(x=0.3), $0.81x10^2$(x=0.6) and $0.76x10^2$ Ωcm (x=1.0).

Table 5-1 Lattice parameters in the system $CuV_{2-x}Mo_xO_6$.

x	a/A	b/A	c/A	α/deg	β/deg	γ/deg	V/A^3
0.0	9.183(2)	3.5564(6)	6.4836(9)	92.32(2)	110.35(2)	91.76(2)	198.15(6)
0.1	9.207(2)	3.5715(5)	6.4641(9)	92.07(2)	110.83(2)	91.48(2)	198.37(6)
0.2	9.237(3)	3.5870(6)	6.453(2)	91.80(2)	111.11(2)	91.24(2)	199.24(8)
0.3	9.270(4)	3.601(2)	6.449(2)	91.52(3)	111.33(3)	91.05(4)	200.4(2)
0.4	9.285(3)	3.6129(7)	6.440(2)	91.23(2)	111.44(2)	90.86(3)	200.99(7)
0.5	9.320(3)	3.6266(7)	6.440(2)	90.92(2)	111.52(2)	90.57(2)	202.46(7)
0.6	9.347(4)	3.638(1)	6.445(2)		111.5(1)		203.8(1)
0.8	9.396(4)	3.6594(9)	6.467(2)		111.5(1)		206.8(1)
1.0	9.447(3)	3.6782(9)	6.487(2)		111.50(9)		209.73(9)

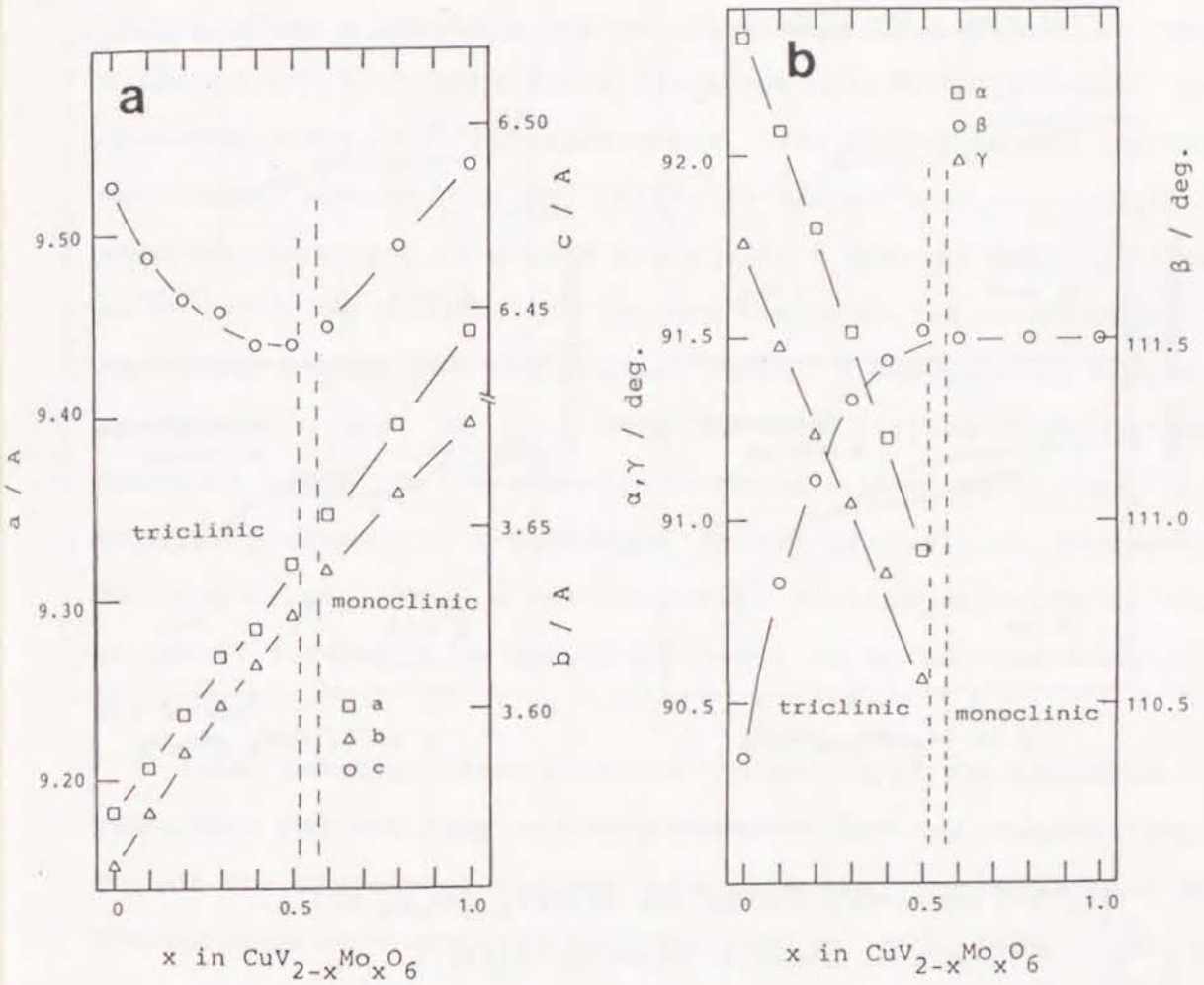

Fig 5-2 Composition dependence of lattice parameters for $CuV_{2-x}Mo_xO_6$ (0<x<1.0). The transition from the triclinic to monoclinic symmetry is observed between x=0.5 and 0.6.

Figure 5-3 shows quasi-OCV curves of $Li/CuV_{2-x}Mo_xO_6$ cells with x=0, 0.3, 0.6, and 1.0 for both discharge and charge directions for the first cycle. The OCV curves during charge were measured by reversing the charge transferred at y=3 in Li_yCuV_{2-}

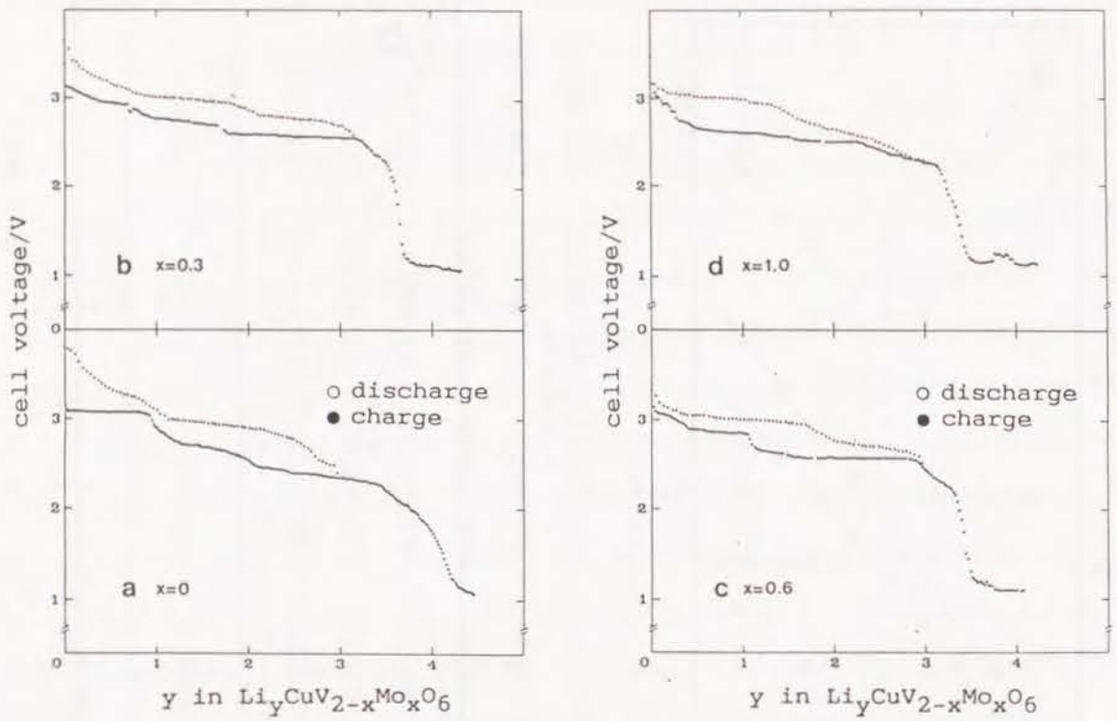

Fig 5-3 Quasi-OCV curves for $Li/CuV_{2-x}Mo_xO_6$ cells.
a)x=0, b)x=0.3 c)x=0.6 d)x=1.0

$_xMo_xO_6$ after a constant current discharge (0.1 mA/cm^2). The different OCV profiles for the discharge and charge processes are characteristic of each compositions. The discharge OCV for the Mo-undoped sample, CuV_2O_6, initially showed a plateau up to a shoulder developed at around y=1.0 with a gradual falling slope up to y=3.5. We believe this plateau indicates the existence of a two-phase region and the gradual slope, a homogeneous single-phase region, that is, the formation of a lithium intercalation compound. With the introduction of Mo ions into the V sites, the initial plateau for x=0 changed to the gradual and shortened falling slope, while a new potential plateau appeared in the range of $1.8<y<3.2$ for x=0.3, $1.7<y<2.8$ for x=0.6, and $1.7<y<2.2$ for x=1.0.

Upon charging, clear plateaus indicative of the existence of two-phase regions were scarcely observed for any compositions. To see the structural changes more directly, the variations in XRD patterns were measured as a function of y in $Li_yCuV_{2-x}Mo_xO_6$ for both discharge and charge processes. The XRD patterns for x=0, 0.3, 0.6, and 1.0 are shown in Fig. 5-4. When the XRD patterns were obtained, tungsten metal powder was mixed with the sample as standard to adjust the peak positions. The XRD patterns of brannerite oxides broadened with increasing charge transferred, y, in $Li_yCuV_{2-x}Mo_xO_6$. The crystallinity especially declined more rapidly in vanadium-rich samples. The small positional displacement of the principal peaks of the original and discharged compounds suggests there is no extensive difference in their crystal structures. The deeply discharged

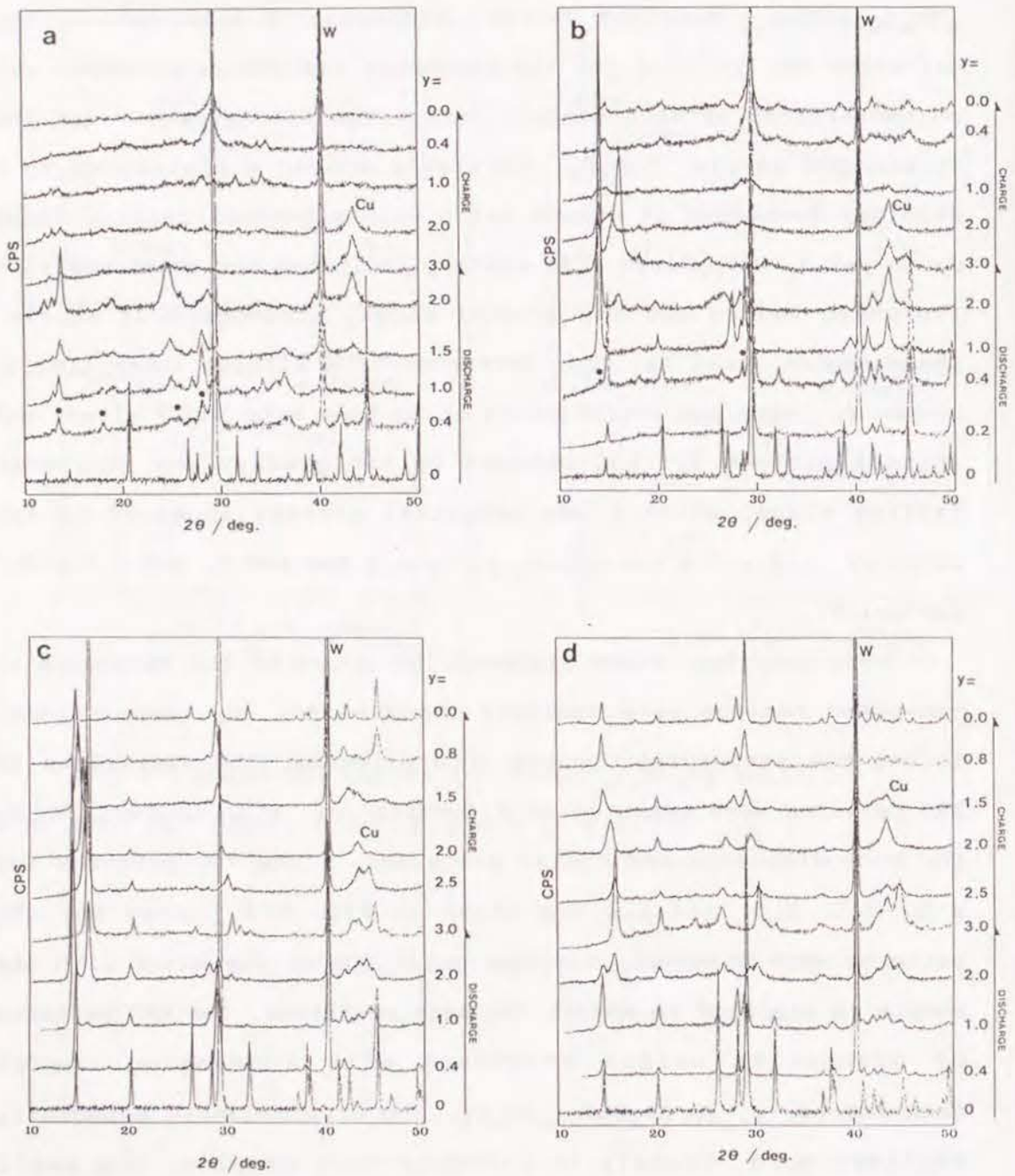

Fig 5-4 XRD patterns of $Li_yCuV_{2-x}Mo_xO_6$ electrodes for various discharge and change depths.

a)x=0 b)x=0.3 c)x=0.6 d)x=1.0

samples were impossible to index because of their low crystallinity. The principal structure of the discharged samples seems to be same for all compositions of x. When the discharged electrodes were charged again, the degree of recovery in the crystallinity depends on the Mo content. The XRD patterns of CuV_2O_6 were hardly recovered, while those of $CuVMoO_6$ were perfectly reobtained. For all compositions of x, peaks corresponding to Cu metal appeared clearly with the increasing discharge depth and vanished perfectly when the cell was charged. It is difficult to detect precisely the small amount of Cu metal on XRD charts because of its low crystallinity, but it roughly begins to deposit at y=1.0 in $Li_yCuV_2O_6$(x=0), y=0.4 in $Li_yCuV_{1.7}Mo_{0.3}O_6$(x=0.3), y=0.4 in $Li_yCuV_{1.4}Mo_{0.6}O_6$(x=0.6) and y<0.2 in $Li_yCuVMoO_6$(x=1.0). With increasing Mo content, the depth where Cu metal begins to deposit appears to shift to smaller y values. The divalent Cu^{2+} ions in $Cu^{2+}{}_{1-x}Cu^{+}{}_xV^{5+}{}_{2-x}Mo^{6+}{}_xO_6$ were, at first, reduced to Cu^{+} state upon intercalation of Li^{+} ions, a process which corresponds to the initial discharge stage observed in the OCV curves shown in Fig. 5-3. As shown in the variation of XRD patterns from y=0 to 1.0 in Fig. 5-4, the phase containing reduced Cu^{1+} ions has a larger c-spacing. For example, the (001) peak refraction near 2θ =15°, which reflects the spacing of $(V,Mo)O_6$ layers, moves to lower angle. This increase of the interlayer spacing is probably due to the Cu^{1+} ions having a larger ionic size than that of Cu^{2+} ions. At x=0 and x=0.3, the original and new(marked by black circles) phases coexist at 0<y<1 and 0.4<y<0.8, respectively. Beyond y=1.0,

metal Cu begins to deposit, and at the same time the new phase having the shorter c-spacing begins to coexist. This phase may be Cu-free or have a low Cu content and be presented as $Li_yV_{2-x}Mo_xO_6$. In the case of x=0, CuV_2O_6, the discharged $Li_3V_2O_6$ is perfectly amorphous but the OCV profile shows that the monophase intercalation reaction occurs in the range $1<y<3$.

In Fig 5-5, the variations of d-spacings corresponding to the (001) plane is shown as a function of y in $Li_yCuVMoO_6$ for both the discharge and charge processes. Other compositions except for x=0, show, on the whole, similar tendency. The OCV and XRD observations suggested that the so called "monophasic region" continues during the whole range of the charging process. The Cu-free $Li_3V_{2-x}Mo_xO_6$ phase looks like it returns smoothly to $CuV_{2-x}Mo_xO_6$ accompanying Li deintercalation and Cu intercalations. On charging, the rapid change in the peak positions between $1.5<y<2.5$ corresponds to Cu intercalation into the electrode material. After recharge, the OCVs for the samples with x=0 and 0.3 show higher values than those found before the discharge. It may be that perfect Li deintercalation is hindered by the occurrence of a quasi-stable structure differing from the original one. On the other hand, a perfectly reversible exchange of Li and Cu ions is observed for x=0.6 and 1.0 in $CuV_{2-x}Mo_xO_6$ electrodes.

This good rechargeability of Li ions in copper brannerite electrodes is due to the tendency of the Cu ions in the structure to be easily deintercalated and intercalated. For other divalent metal brannerite compounds, $M^{2+}V_2O_6$ (M=Mg, Ca, Mn,

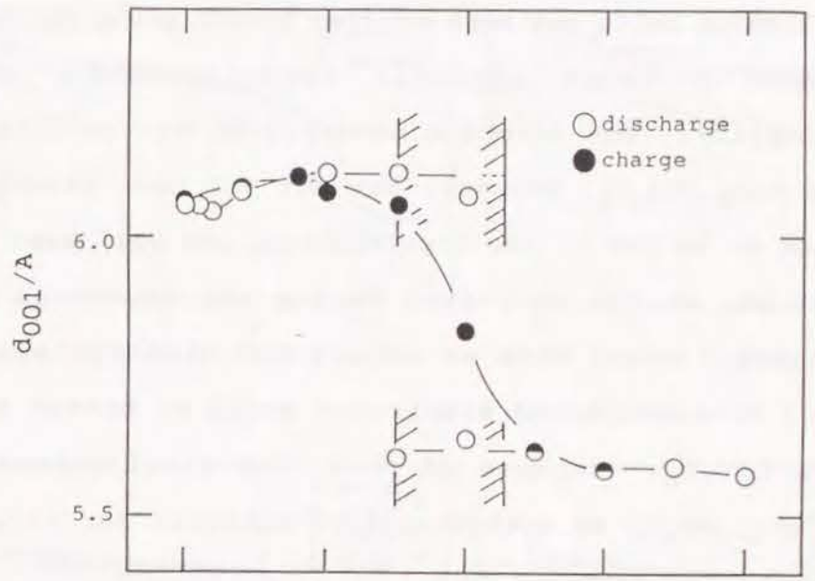

Fig 5-5 Variations of the d-spacing of (001) peak as a function of y in $Li_yCuVMoO_6$.

Co, Ni, Zn, Cd), no divalent metal ion has such a tendency, and consequently, Li ions are hindered from entering the interlayer by the blocking divalent ions.

5.3.2. The Li/$CuV_{2-x}Mo_xO_6$ cell performances

The electrochemical behavior of CuV_2O_6 as a cathode active material for lithium cells has been studied by NTT group in Japan and has shown a large specific capacity and good rechargeability[10]. The cathodic behavior of Mo-substituted Cu-brannerite $CuV_{2-x}Mo_xO_6$, however, has not yet been examined. By substitution of Mo for V, the crystallinity was well kept and the structure was easily recovered during the discharge and charge processes, which made us expect the electrochemical performance of Mo-substituted electrodes would be better than those of pure CuV_2O_6. Because of this, the electrochemical behavior of $CuV_{2-x}Mo_xO_6$ as cathode-active material for lithium cell was studied.

In Fig 5-6, the discharge curves for the cells with $CuV_{2-x}Mo_xO_6$ (x=0, 0.3, 0.6, and 1.0) at current densities ranging from 0.1 to 5 mA/cm^2 are shown. With increasing Mo content, the first plateau observed for y<1 in $Li_yCuV_2O_6$ corresponding to the $Cu^{2+} \longrightarrow Cu^{+}$ reduction shifts to shallower amounts of charge transfer and almost disappears in $CuVMoO_6$, where only a single gentle falling slope, which is equivalent to the second region in CuV_2O_6, becomes dominant. Energy density tends to decrease with increasing Mo content because of the falling voltage. Discharge properties for the cathode with various Mo contents at 0.5 mA/cm^2 are listed in Table 5-2. The energy density was calculated based on a 2.0 V cutoff. At a high discharge rate of 5 mA/cm^2, the capacity drastically decreased in Mo-rich cathodes.

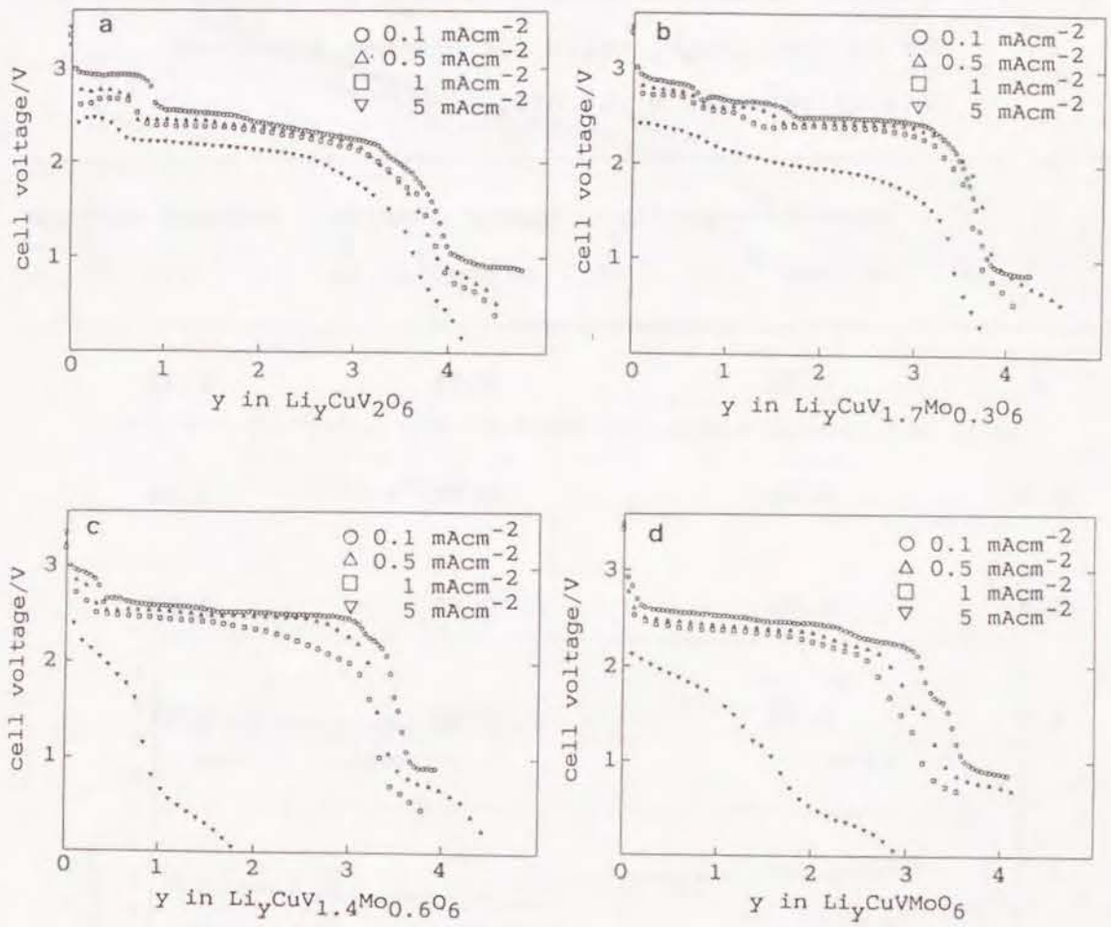

Fig 5-6 Discharge curves at various current densities for the $Li/CuV_{2-x}Mo_xO_6$ cells.
a)x=0, b)x=0.3 c)x=0.6 d)x=1.0

Table 5-2 Specific capacity, energy density, and average voltage for $Li/CuV_{2-x}Mo_xO_6$ cells for discharge process (0.1 mA/cm^2, 2.0 V cut off).

x	Specific capacity (Ahg^{-1})	Energy density (Whg^{-1})	Avarage voltage (V)
0	0.36	0.86	2.42
0.3	0.34	0.87	2.53
0.6	0.32	0.80	2.52
1.0	0.23	0.66	2.39

The cells were cycled over 50 times at 0.8 mA/cm^2 between the potentials of 2.0 and 3.5 V. The tests were tried three times. The variations of specific capacity with cycle numbers are shown in Fig. 5-7 and the typical cycling voltage profiles are shown in Fig 5-8. Contrary to our expectation, there was no distinct difference in cycling behaviors between Mo-nondoped and Mo substituted electrodes except for $Li/CuV_{1.4}Mo_{0.6}O_6$. In this case a rapid decrease and increase in discharge and charge

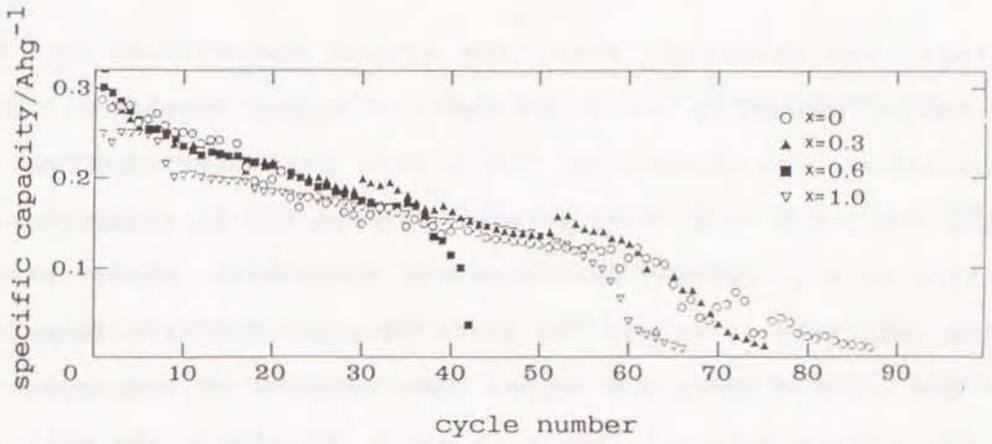

Fig 5-7 Cathodic utilization vs. cycle number for cells $Li/CuV_{2-x}Mo_xO_6$.

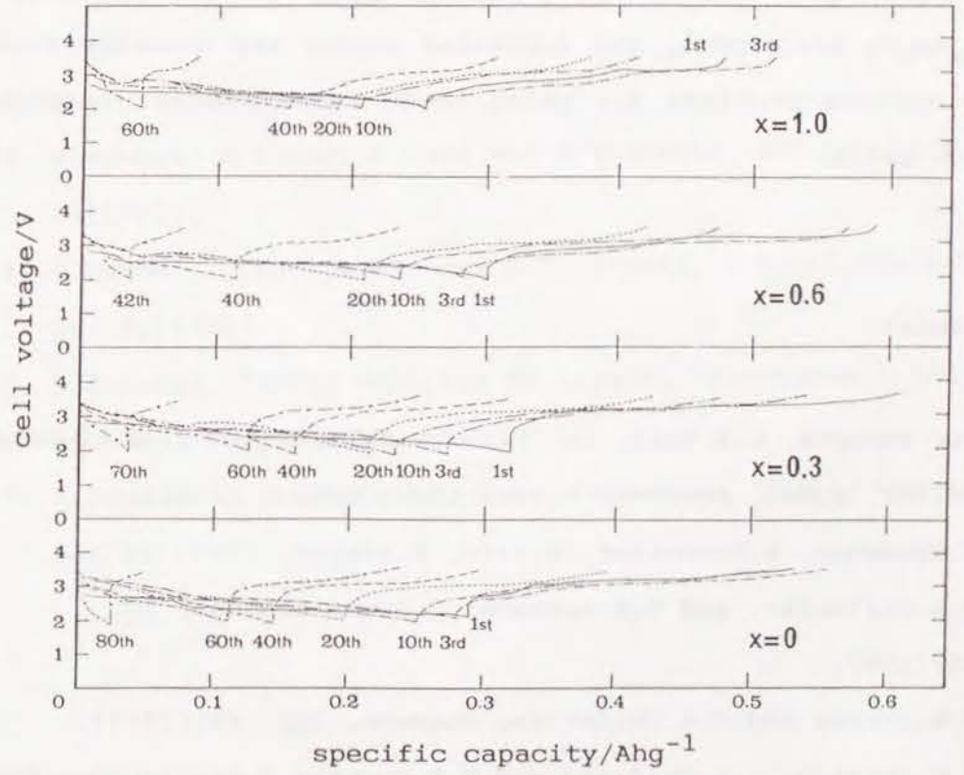

Fig 5-8 Typical cycled curves of the $Li/CuV_{2-x}Mo_xO_6$ cell.

voltages was observed everytime around the 40th cycle. The discharge capacity at 5 mA/cm^2 is quite small at this composition. The minimum of the c-axis parameter observed at around x=0.5-0.6 (Fig. 5-2) likely affects the Li intercalation reaction at high current densities and cycle life. Observations of the materials after cycling tests revealed dendrite formation near the lithium anode and copper discoloration on the separator and the cathode material itself. A short circuit in the cells is one of the possible contributors to the deterioration of cycle life. XRD measurements for cathode materials after much cycling showed broad amorphous lines mixed with those of Cu metal. After many cyclings the cathode material can no longer intercalate copper easily. Thus, in spite of the apparent reversibility of $CuV_{2-x}Mo_xO_6$ electrodes, the deposited copper may possibly slowly cause serious problems for using these materials in secondary lithium cells.

References

1. For example, C.R.Walk, in "Lithium Batteries," J.-P. Gabano, Editor, p.265, Academic Press, Ltd., London (1983).
2. K.Wiesener, W.Schneider, D.Ilic, E.Steger, K.H.Hallmeier, and E.Brackmann, J.Power Sources, 20, 157(1987).
3. D.W.Murphy and P.A.Christian, Science, 205, 651(1979).
4. K.M.Abraham, J.L.Goldman, and M.D.Dempsey,J.Electrochem.Soc., 128, 2493(1981).
5. S.Panero, M.Pasquali, and G.Pistoia, J.Electrochem.Soc, 130, 1225(1983).
6. Y.Sakurai and J.Yamaki, J.Electrochem.Soc., 132, 512(1985).
7. Y.Takeda, R.Kanno, T.Tanaka, and O.Yamamoto, J.Electrochem.Soc., 134, 641(1987).
8. R.J.Cava, D.W.Murphy, and S.M.Zahurak, J.Electrochem.Soc., 130, 243(1983).
9. R.J.Cava, D.W.Murphy, and S.M.Zahurak, J.Electrochem.Soc., 130, 2345(1983).
10. Y.Sakurai, H.Ohtsuka and J.Yamaki, J.Electrochem.Soc., 135, 32(1988).
11. K.Mocala and J.Zlolkowski, J. Solid State Chem., 69, 299 (1987).
12. Unpublished data
13. Y.Takeda, R.Kanno, M.Noda and O.Yamamoto, Mat.Res.Bull., 20, 71(1985).
14. T.Machej, R.Kozlowski, and J.Zilikoski, J.Solid State Chem., 38, 97(1981).
15. T.Sakurai, "X-Ray Analysis of Crystal Structures," 2nd ed. Syokabo, Tokyo(1969).
16. K.Macala, J.Zlolkoowski, and L.Dziembaj, J.Solid State Chem., 56, 84(1985).

Part II

Anodic Reaction Mechanisms of Carbon Materials

Chapter 1. Carbon-Lithium Composite Anode for Lithium Secondary Battery.

1.1 Introduction

For the realization of lithium secondary batteries, there still exist some problems in the cathode material, electrolyte and anode material respectively. Especially the anode cyclability has a great importance for the realization of the practical lithium secondary batteries. Except for the bare lithium anode, lithium-aluminum alloy or the suitable electrolyte for making the surface film on lithium metal have been used so far. These are used for covering the lithium metal surface in order to avoid the formation of lithium dendrites. This surface covering film must be highly reductive and stable. In this respect the carbon is most suitable for the anode material of lithium batteries[1]. As a carbon material, thermal decomposition products of polymers such as polyphenylene and polyalylacethylene will be good candidates because or their high surface area. By using these materials, better cell cyclability would be expected[2]. In this study, some carbon-lithium composite anodes were discussed, and the charge-discharge mechanisms were studied in detail.

1.2 Experimental

In this study, carbons thermally decomposed from polymers in our laboratory and commercial products were used. The former materials were produced from polyphenylchloroacetylene(PPCA), polyvinylidenefluoride(PVDF), plyvinylidenechloride(PVDC) etc. by heating at 800 °C for 2 hours under N_2 atmosphere. The latter materials were supplied from various companies and they are called M46, VM60019, A6000 etc. Before testing these materials, they are ultrasonically pretreated in acetone and then dried. The preparation of the working electrode was as follows. The carbon material(50 mg) and polytetrafluoroethylene(PTFE) powder(5 mg) as a binding agent were mixed. This mixture was pressed under 100 kg cm^{-2} and formed into a disc shape(dia. 13.5 mm).

The cell construction is shown in Fig. 1-1. The two types of test cells were used. The cylindrical cell was used for the testing of the carbon fiber itself, while the commercial coin type cell was used for testing the characteristics as a secondary lithium battery. In both cases, the counter electrode was a lithium foil and the electrolyte was 1:1 propylene carbonate(PC)-dimethoxyethane(DME) containing 1 M $LiClO_4$. The separator was a microporous polypropylene sheet. The pellet of Cr_3O_8 was used as a cathode for the lithium secondary battery with the carbon-lithium composite anode. This cathode was prepared by the thermal decomposition of CrO_3 in an autoclave[3].

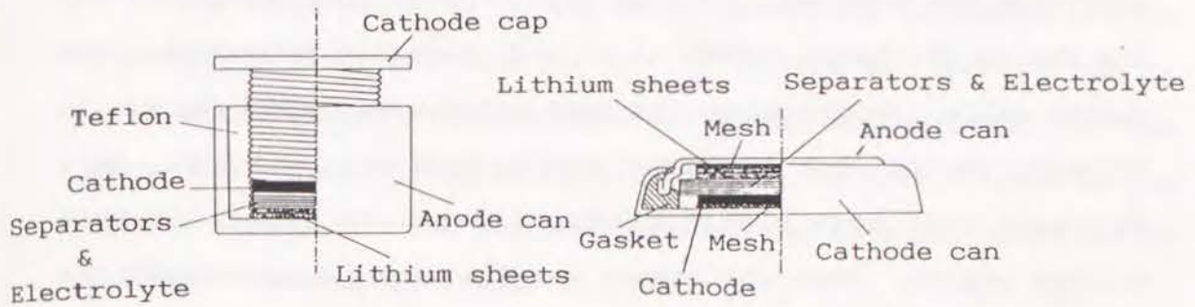

Fig. 1-1 The constructions of the carbon test cell and coin-type cell.

The materials obtained were characterized by using XRD, BET adsorption measurement, scanning electron micrograph(SEM) and XPS. The electrochemical measurements were carried out using a potentiostat. In the galvanostatic mode, the cutoff voltage was -0.03 V in charge and 2.5 V in discharge vs. Li/Li^+. The current density was 350 μA cm^{-2}. The open circuit voltage(OCV) was measured after a charge of specific capacity and 1 day duration. All the procedures were performed in an Ar atmosphere dry box.

1.3 Results and Discussion

At first, the charge-discharge characteristics of the carbon

electrode was examined. In Fig. 1-2 are shown the charge OCV and the charge-discharge curves of Li and thermally decomposed PPCA carbon cells. On charging, the cell voltage decreased rapidly in an early period, but decreased slowly from ca. 1 to 0 V. This suggests that some electrochemical reaction occurs in this voltage region. When the carbon was discharged successively the voltage rapidly increased to 2.5 V. This results show that only a little part of the charged lithium could be discharged. The OCV curve indicates that in the early period, the overvoltage was very large. On the other hand, it became very small after 20 hours charge. As mentioned before, the charge mechanisms of the carbon seemed to be different between the higher and lower voltage regions. What sort of reaction would occur in the course of charge is not clear at present.

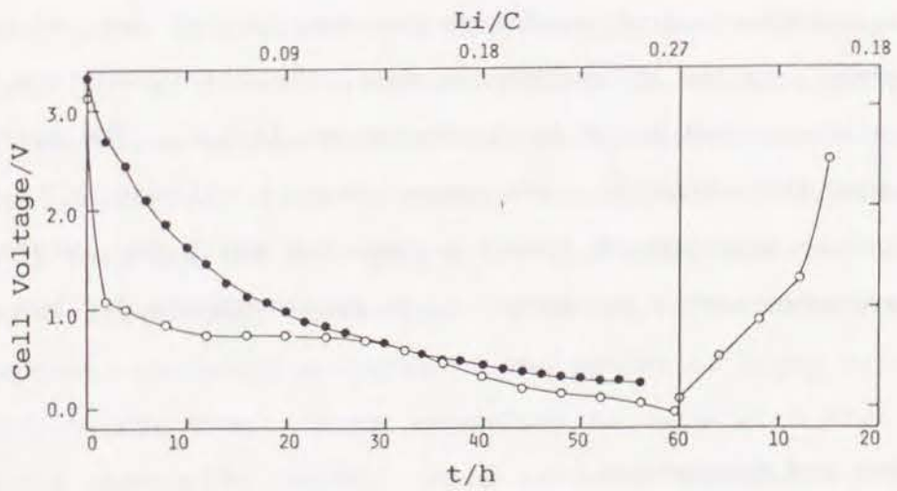

Fig. 1-2 The charge-discharge curves and OCV curve for the cell Li/carbon(PPCA) with current density 0.35 mA cm^{-2}. Open circles:CCV; Closed circles:OCV

The large capacity in the first charge may be partly due to adsorption onto the surface of the carbon and partly due to intercalation into the van der Waals gap of the graphite-like structure. Thus, it is important to know the surface area of the carbon examined. The surface area of the carbons, measured by the BET method, is listed in Table 1-1.

Table 1-1 Lithium storage capacities of thermal decomposition products of polymers and carbon fibers.

polymer or carbon fiber		Charge capacity (mAh/100mg) cycle number 1	3	5	Discharge capacity (mAh/100mg) cycle number 1	3	5	surface area (m^2/g)
Thermal decomposition polymers	PPCA	59.6	13.5	14.6	15.7	12.4	13.6	430
	PVDF	67.8	8.3	4.3	8.2	6.5	3.8	380
	PVDC	57.7	5.1	2.4	5.5	3.4	2.2	510
	POB	58.0	2.1	1.4	5.8	2.1	1.6	280
	PS	36.8	2.6	1.6	5.0	2.9	1.5	100
	PEPY	10.8	1.2	0.8	1.0	0.9	0.6	6
	PVC	27.0	0.8	0.6	5.0	0.7	0.6	4
	Graphite	14.0	1.0	0.5	0.8	0.6	0.4	4
carbon fiber	M46	18.5	7.3	8.4	8.3	7.1	8.1	1.3
	T300	21.8	3.5	1.1	2.3	0.8	0.5	1.6
	(Toray Industries, Inc.)							
	GM60019	22.4	5.8	3.5	6.2	5.1	3.1	1.3
	HTA-7	43.9	6.8	4.7	15.9	5.6	4.0	3.6
	GM6060ST	13.8	3.4	3.1	6.6	3.0	2.8	0.7
	(Toa Nenryo Kogyo, kk.)							
	GF8	24.2	1.4	1.2	4.9	1.1	0.8	0.4
	(Nippon Carbon Co. Ltd.)							
	A6000	33.8	0.5	0.3	7.4	0.3	0.4	4.9
	(Asahi Nippon Carbon Co. Ltd.)							
	HTA-7	28.4	3.2	3.1	10.5	3.2	2.8	3.6
	BP1034AES	13.6	0.5	0.2	11.0	0.4	0.1	1.1
	(Toho Rayon Co. Ltd.)							

PVDF : Polyvinylidenefluoride PVDC : Polyvinylidenechloride
POB : Polyoxybenzoate PS : Polysulfon
PEPY : Polyetherpolyimide PVC : Polyvinylchloride
PPCA : Poly-2-chloro-1-phenylacethylene

In the case of the thermal decomposition carbons, except for PPCA, the storage capacities at the 1st cycle increased with increasing surface area. From these results, the lithium charge capacity of the thermal decomposition products depends mainly on the lithium adsorption capacity on the carbon surface. The lithium storage is probably explained by charging the double layers on the carbon electrodes. Loss of capacity on following cycles indicate lithium adsorption onto surface is irreversible reaction. The reversible cyclability is not accomplished by a surface reaction and we suppose that intercalation reaction brings high reversibility. But in the case of PPCA, no significant decrease of capacity could be observed after 2nd cycle. This shows that the electrode reaction mechanism is different from those of the other thermal decomposition carbons. On the other hand, the surface areas of the commercial carbon fibers are extremely small in comparison with those of the thermal decomposition carbons. Moreover, loss of capacity was much smaller than thermal decomposition carbons. These results show lithium intercalation was predominant reaction in the commercial fibers. The highest efficiency was observed for the carbon fiber M46. In the case of PPCA and M46, the reaction of lithium intercalation into the host matrix is considered to contribute to the high charge capacity. The cycle test for PPCA showed good rechargeability only over 50 cycles, while the M46 showed over 1000 cycles. We conclude that M46 is a candidate for the anode of lithium secondary batteries.

The charge mechanisms of the carbon fiber M46 were studied

by the XRD method. Fig. 1-3(a) shows the XRD patterns at various charge capacities. The (002) peak shifted to lower angles with deeper charge, indicating the expansion of the inter layer along the c-axis. The intercalation of lithium ions and/or solvated lithium ions into the van der Waals gap would occur. The d-values of the (002) peak are plotted against the charge capacity in Fig. 1-3(b). This shows that the lithium charge reaction with M46 proceeds via. 3 steps.

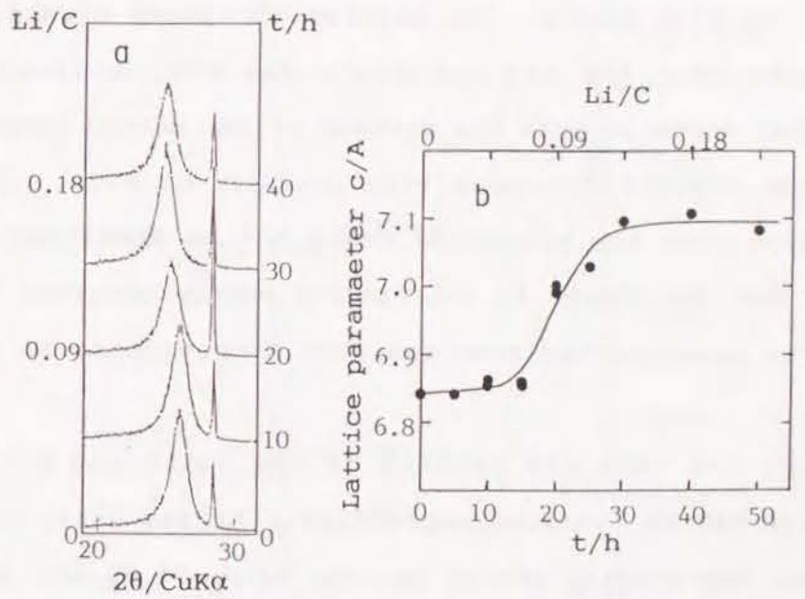

Fig. 1-3 (a)X-ray diffraction patterns of the carbon fiber M46 at different lithium capacities. (b)The change of the d-value of the carbon fiber M46 through the charge.

First, for x(Li/C)<0.05, lattice expansion was not observed. In this early region the lithium intercalation reaction did not proceed. This indicates that the surface reaction such as lithium adsorption occurred. For 0.05<x<0.14, a linear increase of d-value was observed. In the carbon fiber M46, the structure does not have a graphite type regular arrangement[4,5]. The staging structure does not appear and the peak is seemed to be the average of all the (002) peaks which have different level of expansion. In this charging stage, the lithium intercalation might occur and highly reversible characteristics could be expected. For x>0.14, no further lattice expansion could be observed. In this region, the lithium ions have already fully intercalated into the van der waals gap and, consequently, lithium metal deposits onto the surface of the carbon fibers.

For the thermal decomposition product of PPCA, lithium intercalation into the electrode could not be confirmed by the XRD data. But the change in the binding energy observed for XPS measurements suggests the same reaction mechanism as in the M46 material.

In Fig. 1-4, the XPS spectra of the Li 1s and C 1s were measured for M46 at various capacities. At the early stage of the charge, the binding energy of the Li(E_b=54.89 eV) is close to that of metallic lithium (E_b=54.69 eV). This shows that at the first stage of charge (x<0.05), the lithium exists in a metallic state and/or some reaction products with small binding energy. The peak shifts to higher energy with lithiation (x>0.05) and the maximum value (E=55.49 eV) is obtained around

x=0.09. This lithium is deduced to be the intercalated one and is in different state from the lithium at the early stage. Also at this capacity, the cyclability showed the highest efficiency. For x>0.14 the binding energy of lithium was reduced again and its value became as same as that of metallic lithium. Lithium metal deposition would happen in this region. This lithium did not show the good reversibility.

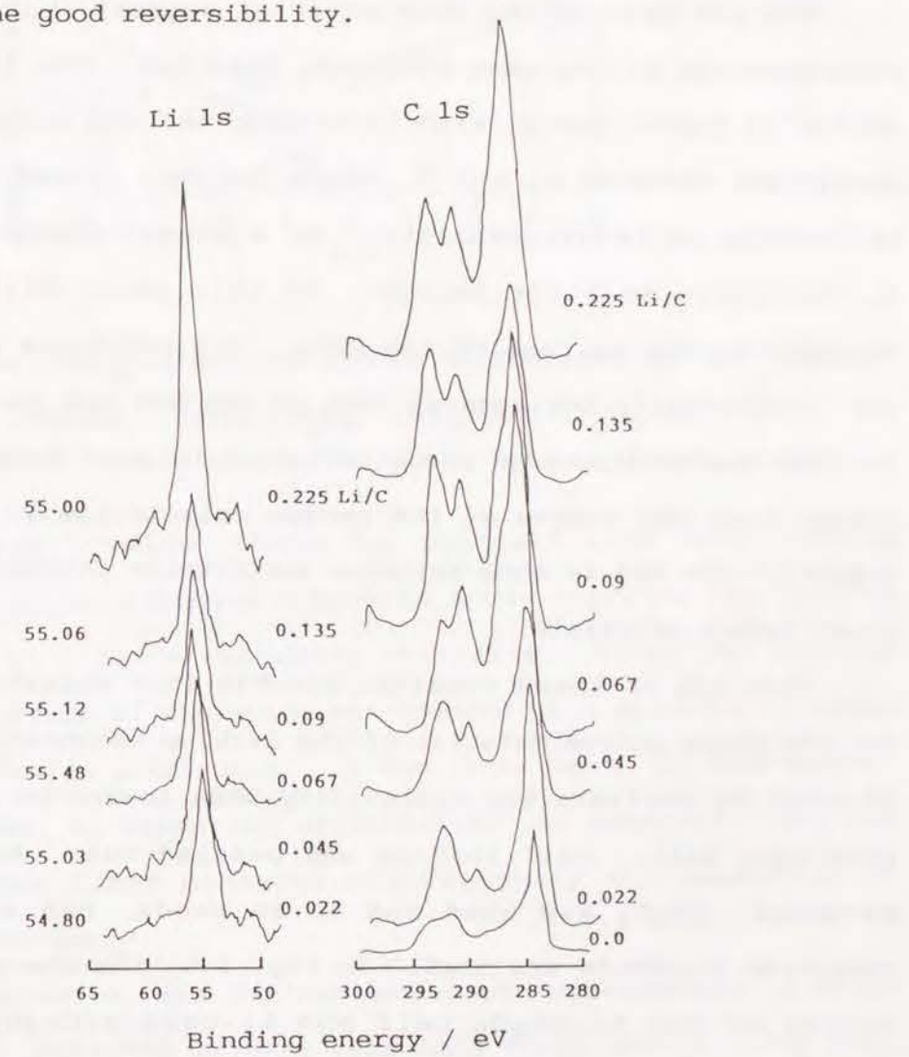

Fig. 1-4 The XPS spectra of the carbon fiber M46 at different lithium capacities.

For the C 1s spectra, a new peak with a higher binding energy(E=285.7 eV) was observed for the lithiated carbon besides the original carbon peak. The height of the new peak increased with charging and became a maximum at around x=0.09. The M46 showed the highest efficiency in rechargeability at this point as mentioned above.

The XPS data on the PPCA material suggest that the charge also proceeds by the same electrode reaction. The lithium peak shifts to higher energy with lithiation and the highest binding energy was observed at x=0.21, where the cell showed the highest efficiency in rechargeability. In a deeper charge, the peak shifts again to lower energy. At this point lithium metal deposits on the surface of the PPCA. The reactions of the PPCA are intrinsically the same as that of the M46 and the difference for the charge-discharge characteristics between these materials arises from the degree of the random orientation in the carbon crystal. The M46 is more suitable for lithium intercalation than other carbon materials.

From all of these results, the M46 is a suitable material for the anode active material of the lithium secondary batteries. In order to estimate the cyclability when loaded in a practical coin-type cell, cell testing was carried out. As a cathode material, Cr_3O_8 was used and as an anode, M46 and lithium composite electrode was used. In Fig. 1-5, the charge-discharge curves of the Li/Cr_3O_8 cell and Li-carbon/Cr_3O_8 cell are compared. For the cells using lithium metal, 80 cycles were obtained, while for the composite anodes, more than 170 cycles

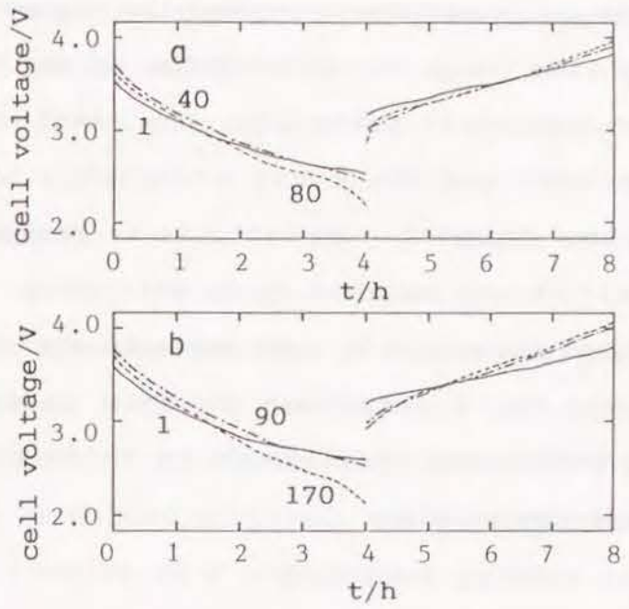

Fig. 1-5 The charge-discharge cycles of the cell using Cr_3O_8 as a cathode. (a)Li/Cr_3O_8 (b)Li-M46/Cr_3O_8

were obtained; twice those for the cell with only lithium anode. The carbon-lithium composite anode improves the cycling efficiency in lithium secondary batteries. After the cycling test, the surface of the anode was covered with dendritic lithium when only lithium metal used. On the other hand, for the carbon-lithium anode, no formation of dendrites was observed. The use of M46 carbon fiber hindered significantly the formation of lithium dendrites.

In conclusion, the carbon anodes can accommodate lithium ions and/or solvated lithium ions into their matrix. For M46, the lithium intercalation occurred at the utilization range

0.05<x<0.14 and the cycle efficiency showed the highest value in this region. Applying these characteristics to the reversible anode of lithium secondary batteries, the lithium dendrite formation was reduced and the cycle efficiency of the Li-carbon/Cr_3O_8 cell was improved. In fact, it is proved that the Li-carbon/Cr_3O_8 cell showed improved cycle efficiency. However, it is not clear what structure is most suitable for the lithium reversibility, and it is necessary to know in detail the structure of the carbon and the lithium as an intercalant to develop better carbon materials.

References

1. J.O.Besenhard and H.P.Frits, Angew.Chem. Int.Ed.Engl., 22, 950(1983).
2. F.P.Dousek, J.Jansta, and J.Baldrian, Carbon, 18, 13(1980).
3. K.A.Wilhelmi, Acta Chem.Scand., 22, 2565(1968).
4. Y.Matsuda, M.Morita, and H.Katsuma, Denki Kagaku, 51, 744(1983).
5. F.Beck, H.Junge, and H.Krohn, Electrochimica Acta, 26, 799(1981).

Chapter 2. Reaction Mechanisms of Lithium and PAN-Based Carbon Fiber

2.1 Introduction

During the past decade, a substantial research effort has been directed into the development of rechargeable lithium batteries. Although some improvements in cycle life and efficiency have been achieved, the reversibility of the lithium electrode remains as a significant problem in aprotic solvent based electrolytes. The major problems limiting cycle life are short circuits resulting from the growth of lithium dendrites and macroscopic shape changes during the recharge process. One solution to these problems is to use a lithium aluminum alloy instead of pure lithium[1,2]; β-LiAl electrodes limit the formation of dendrites and therefore exhibit good rechargeability. However, unsatisfactory mechanical stability is evident in these alloys due to the large volume change caused by the phase transformation that occurs during the removal or addition of lithium[3]. The other approach is to vary the electrolyte solution; the charging efficiency of pure lithium electrodes can reach 96-98 % in a carefully selected electrolyte solution[4]. Recently, a "rocking chair" battery that uses intercalation compounds has been proposed to solve this problem[5-8]. Among the alternative materials that could replace

lithium metal, carbon might be the best candidate as the negative electrode[9-12].

Carbon materials were previously proposed for the use as cathodes; Brenner first reported a combination of $Li/LiBF_4$, sulfolane (or 3-methylsulfolane)/graphite[13]. The charge and discharge mechanism of the graphite cathode was considered to be an intercalation reaction of anions as follow:

$$nC + A^- \underset{\text{discharge}}{\overset{\text{charge}}{\rightleftharpoons}} C_nA + e \ ,$$

where n and A^- indicate an integer and an anion, respectively [14, 15]. On the other hand, carbon has been proposed for use of anode of lithium batteries. Thermal decomposition products of polymers such as polyphenylene and polyalylacethylene are reported to have possibilities as negative electrodes in lithium cells[16, 17].

In previous work, we have examined carbon materials for use in anodes of rechargeable lithium batteries. While some carbon materials showed a significant loss in capacity during their first charge-discharge cycle, and a rapid decrease in efficiency upon further cycling, the thermal decomposition products of poly (2-chloro-1-phenylacetylene) and the carbon fiber M46 (Toray Industries, Inc.) stored lithium reversibly and showed high cycling performance[9, 10]. No significant degradation in the capacity was observed after two cycles for the thermal decomposition product of PPCA and the carbon fiber M46. The efficiencies at the 5th cycle of those carbons were calculated to

be more than 90 % based on the capacities at the 2nd cycle. Further, no surface area dependence of the storage capacity at 5th cycle indicated that the surface does not participate in the reversible lithium storage. These results were consistent with those obtained on petroleum coke reported recently by Fong et al.[12].

It was, however, difficult to determine if the reaction mechanism of the thermal decomposition products of PPCA, because the carbon synthesized by the thermal decomposition around 1000°C gave very broad X-ray diffraction peaks; the X-ray data showed no evidence of whether the reaction proceeded by the intercalation process or by other mechanisms. The carbon fiber (M-46), on the other hand, showed enough graphite character to give a relatively sharp X-ray diffraction (002) peak. This might enable us to determine the reaction mechanism with lithium.

The present paper is concerned with studies of the electrode reaction mechanisms and the cycling properties of carbon fiber anodes. We determined the charge properties, open circuit voltages (OCV), lattice parameters, and thermal behavior of carbon fiber electrodes using electrolytes with various PC/DME rations. In addition, the lithium/carbon-fiber composite anodes were found to reduce lithium-dendrite formation and to be promising anode candidates for lithium secondary cells.

2.2 Experimental

We examined the electrochemical properties of the carbon fiber M46(Toray Industries, Inc.) in order to clarify the detail of the lithium storage process. Typical properties of these fibers are as follows: diameter of a single fiber: ca. 6.5 μm, density: ca. 1.88 gcm^{-3}, tensile modulus: 4.51 x 10^{11} Nm^{-2}, tensile strength: 2.35 x 10^{9} Nm^{-2}. The x-axis parameter of the carbon fiber was determined to be 6.84 A (d(002) = 3.42 A), indicating that the fiber has little graphite character, about the same as Petroleum coke used in ref.[12]. The surface area measured by the BET method was 1.3 m^2g^{-1}. The crystallite size determined by (002) X-ray reflection was 50.4 A[18].

The working electrode consisted of a mixture of 50 mg carbon fiber and 5 mg Teflon powder pressed into a tablet of 13mm diameter under a pressure of 9 MPa. The cells used for the electrochemical tests were constructed in a cylindrical configuration described previously[19] or in a stainless steel 2025 coin-type configuration (20 mm outside diameter and 2.5 mm thickness). The counter electrode was a 15 mm diameter and 0.24 mm thickness disk of lithium metal foil. The separator employed was a microporous polypropylene sheet. Typical electrolytes used in these cells were 1 M solutions of $LiClO_4$ in a 50:50 mixture of propylene carbonate(PC) and 1,2 dimethoxyethane(DME) (Mitsubishi petrochemical company Ltd., battery grade) by volume. All reagents were dried in a standard manner[20, 21]. The water content of the electrolytes was less than 20 ppm. The cells were constructed in an argon filled glove-box. The 2025 coin-type configuration cells were used for

the "composite anode" cells. These cells were constructed as follows: the carbon anode was a mixture of 50 mg carbon fiber and 5 mg Teflon powder pressed into a tablet 15 mm diameter, which was placed on a lithium metal disk with 13 mm diameter and 0.4 mm thickness; the cathode was a mixture of 20 mg Cr_3O_8, 4 mg acetylene black and 0.3 mg Teflon powder. Chromium oxide, Cr_3O_8, was obtained by heating CrO_3 for 24 h at 270°C in an autoclave[19]. The current density was calculated based on the carbon electrode area. The electrochemical measurements were carried out at room temperature after an overnight stand under zero current flow. Cell properties were measured galvanostatically. Quasi-open-circuit voltages (OCV) were measured by alternating charge and rest periods. A constant current of 0.075 or 0.375 $mAcm^{-2}$ was passed through the cell for some period, and the cell voltages on an open circuit were considered as the quasi-OCV when the change in the measured cell voltage was less than 1 mV. After the electrochemical test, the carbon electrodes were handled under argon and were used for the following measurements without washing or drying.

X-ray photoelectron spectroscopy (XPS) spectra were measured with a Shimadzu ESCA 750 spectrometer. The reaction and weight loss of the carbon electrodes on heating to 500 °C were measured by an automatic differential thermal analysis-thermogravimetry (DTA-TG) apparatus of Rigaku DTA-6, TG-4. The measurements were carried out in an argon gas flow. For the XPS and the DTA-TG measurements, the sample chambers of the apparatus were covered with a glove-bag filled with dry argon when the samples were

loaded.

X-ray powder diffraction (XRD) data were collected with CuKα radiation using a high power X-ray diffractometer (Rigaku RAD 12kW) equipped with a graphite monochrometer. The samples for the XRD measurements were mounted on a specially designed X-ray holder in an argon .atmosphere after the electrochemical test. A 7 μm-thick aluminum window covered the sample holder to prevent moisture attack during the measurement. Lattice parameters were calculated against an internal silicon standard.

2.3 Results and Discussion

2.3.1 Charge-discharge properties of the Li/carbon fiber M46 cells using the solvents with various PC/DME ratios

Figure 2-1 shows an example of the first charge-discharge cycle for the Li/carbon fiber M-46 cell using the solvent mixture consisting of PC and DME, 50-50 by volume. The current density was 0.375 $mAcm^{-2}$ and the cut-off voltages were -0.03 V for charge and 2.5 V for discharge. On charge, the cell voltage decreases rapidly to 1 V, and after, decreases slowly to 0.0 V. The cell was then discharged. The amounts of lithium stored, Li/C, in the figure have not been renormalized. They were calculated from the current and the mass of carbon in each cell. This measures only the average Li content of the entire electrode[22]. The lithium storage capacities obtained were 18.5, 7.3, and 8.3 mAh/100mg for the first, second and third

charge, respectively.

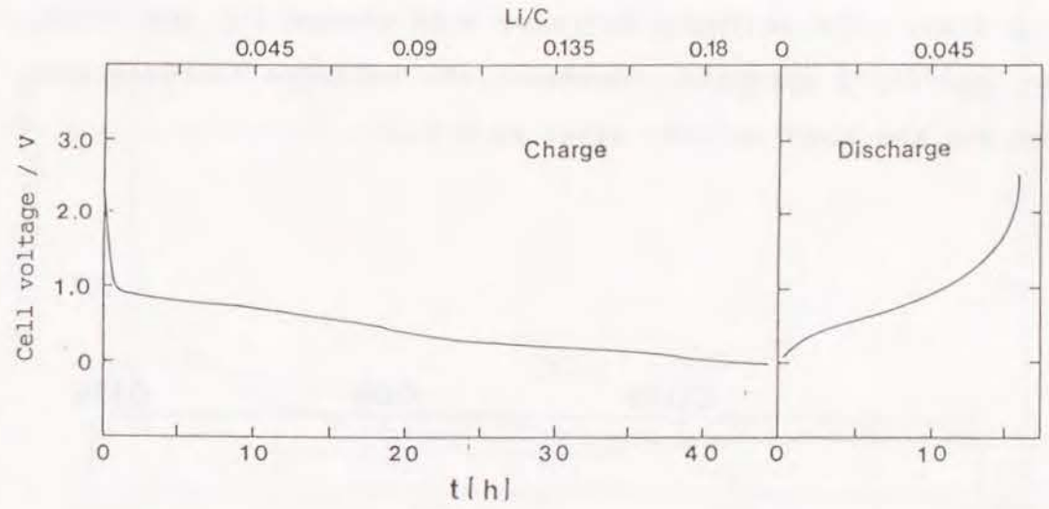

Fig. 2-1 Charge and discharge curve of the Li/carbon fiber M46 cell at 0.375 $mAcm^{-2}$ current density.

Figure 2-2 shows the charge curves for the Li/carbon fiber cells using solvent mixture with different PC/DME ratios, 100/0, 75/25, 50/50, and 25/75. The current density was 0.375 $mAcm^{-2}$ (Fig. 2-2(a)). The voltages decrease with Li/C for the cells with the 50/50 and the 75/25 solvents. However, the voltages rise with Li/C after Li/C 0.09 for the 100/0 solvent and after Li/C 0.055 for the 25/75 solvent. Lithium metal is observed on the carbon fiber surface even at a shallow charge depths for cells using the 25/75 solvent, indicating an inhomogeneous

reaction on the carbon fiber surface in this solvent. Figure 2-2(b) shows the charge curves with a current density of 0.075 $mAcm^{-2}$. The curves are slightly different from those shown in Fig. 2-2(a). The voltages decrease with charge for the 75/25, 50/50, and 25/75 solvents. However, the voltages increase with charge for the 100/0 solvent after Li/C 0.02.

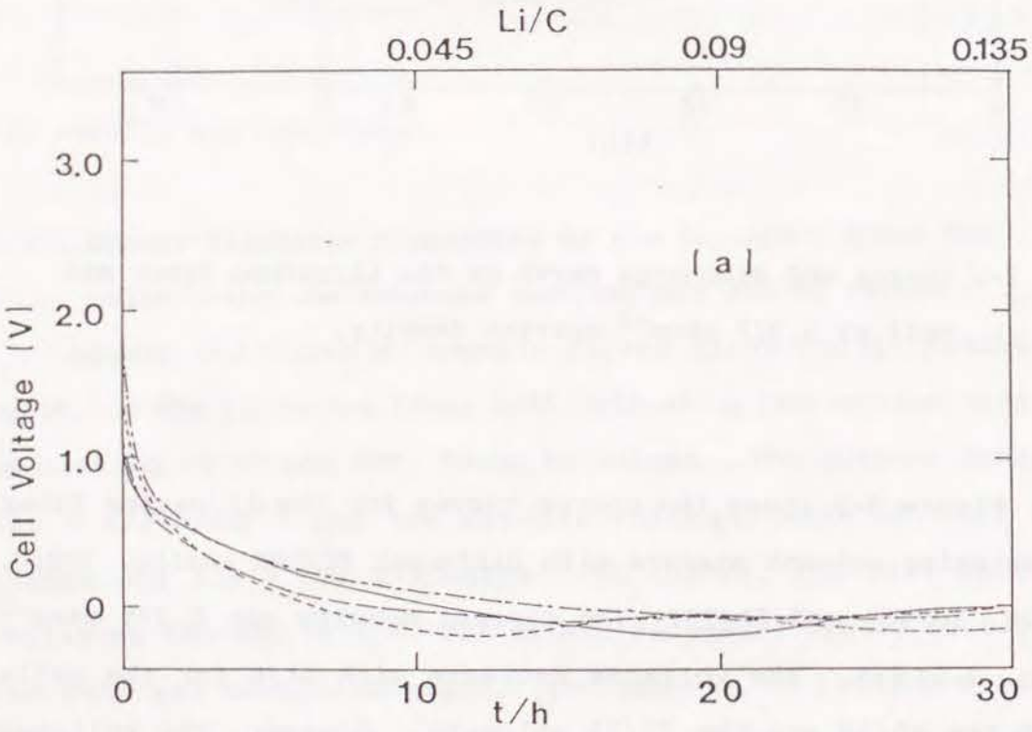

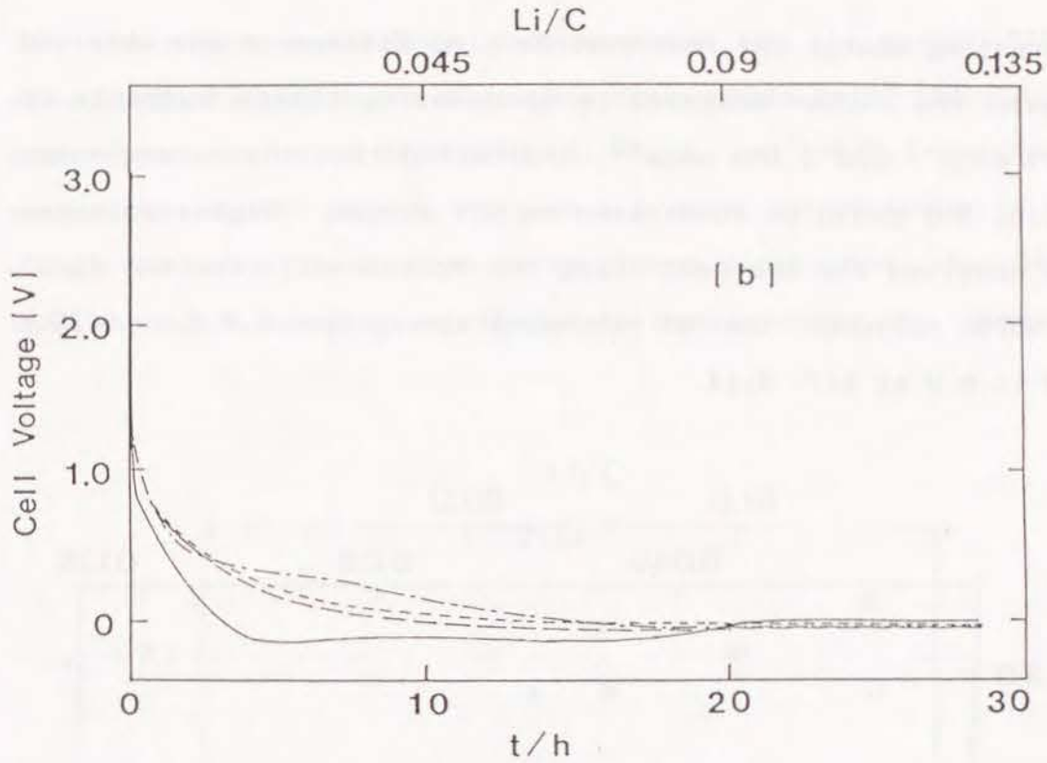

Fig. 2-2 Charge curves for the Li/carbon fiber M46 cell using the solvent mixture with various PC/DME ratios:
100/0(——); 75/25(---)
50/50(—·—); 25/75(·····)
The current densities were 0.375 $mAcm^{-2}$(a), and 0.075 $mAcm^{-2}$(b).

The OCV was measured for the Li/carbon fiber M46 cells using the 100/0, 75/25, and 50/50 solvents, in situations where no lithium deposition was observed in the shallow lithiated region. Figure 2-3 shows the cell voltages vs. Li/C curves measured by

alternating charge and rest periods. No difference was observed between the curves measured by alternating charge currents of 0.375 $mAcm^{-2}$ and 0.075 $mAcm^{-2}$, indicating that the curves shown in Fig. 2-3 could be considered as OCV curves. Higher voltages were observed for the cell using the PC solvent. For the 75/25 and 50/50 solvents, the OCV decreases slowly from 0.8 V at Li/C = 0.09 to 0 V at Li/C 0.14.

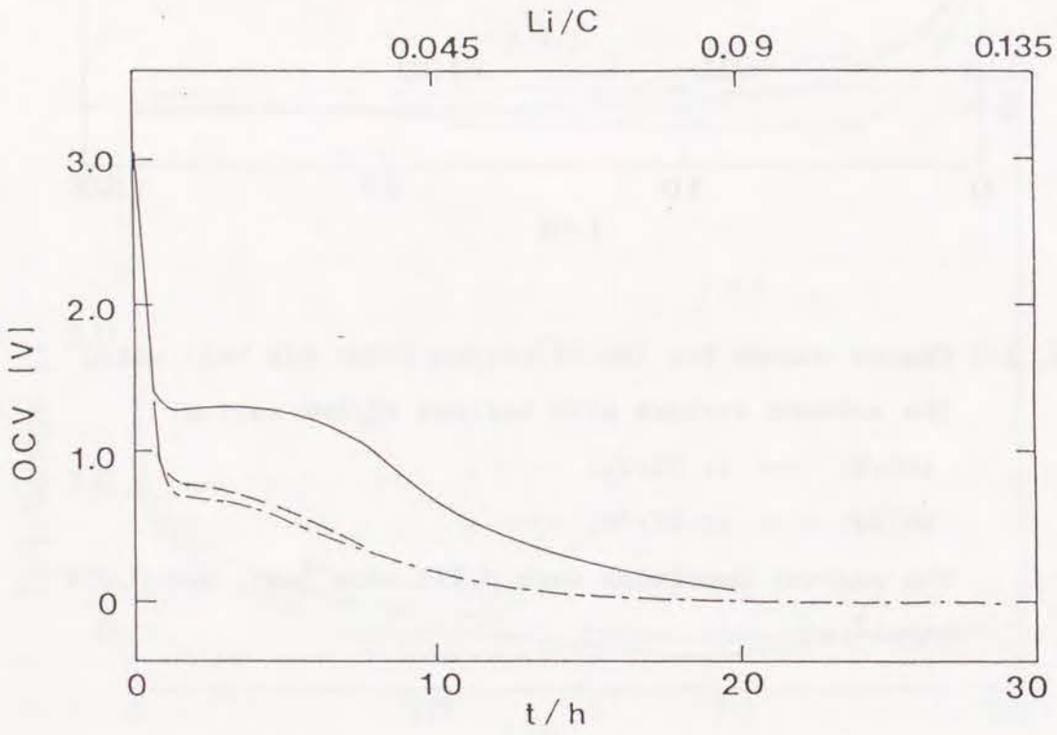

Fig. 2-3 OCV curves of the Li/carbon fiber M46 cells using the solvent mixture with various PC/DME ratios:
100/0(——); 75/25(– – –); 50/50(—·—).

The c-axis parameters were measured for the carbon fiber electrodes charged in the Li/carbon fiber cells using the solvent with PC/DME ratios of 25/75, 50/50, 75/25, and 100/0. The charge current was 0.375 $mAcm^{-2}$. Figure 2-4 shows the variation of the c-axis parameters as a function of charge depth. For the 50/50 and the 100/0 solvents, no change in the parameter was observed

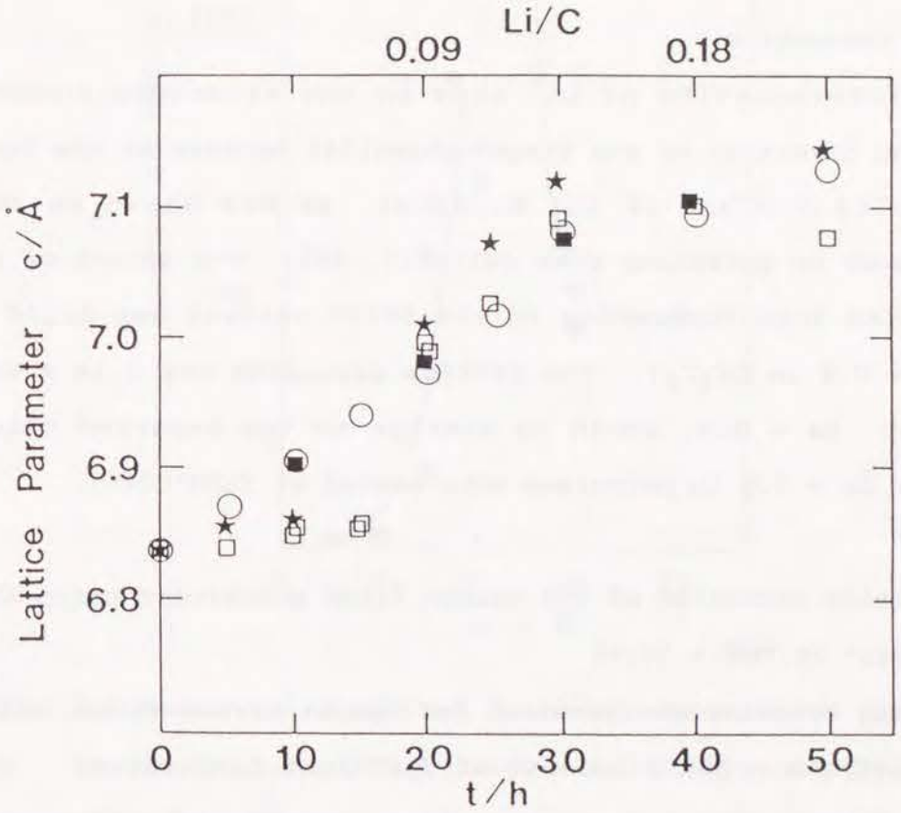

Fig. 2-4 Lattice parameter changes of the carbon fiber M46 electrodes as a function charge time. The solvents were the mixture of PC/DME with ratios of 100/0(★), 75/25(○), 50/50(□), and 25/75(■).

from Li/C = 0 to 0.067, while for 0.067 < Li/C < 0.135, the parameter increases from 6.82 to 7.0 A with charge. For the 25/75 and 75/25 solvents, on the other hand, the parameters vary from Li/C = 0 to 0.135; the intercalation proceeds from a very shallow lithiation range. The potential at which the lithium starts to intercalate was determined using the charge curves shown in Fig. 2-2(a). The lithium intercalation started at 0, 0.8 and 0 V vs. Li metal for the 50/50, 75/25, and 100/0 solvents, respectively.

The intercalation of Li^+ ions in the structure occurs without the formation of any staged-phase[24] because of the lack of crystalline order of the material, as was shown in the previous work on petroleum coke cells[12, 25]. The amount of Li intercalated into the carbon in the 50/50 solvent was $\Delta Li/C$ = 0.067 (x = 0.4 in Li_xC_6). The lattice expansion was 0.14 A for d(002) for Δx = 0.4, which is similar to the reported value 0.15 A for Δx = 0.5 in petroleum coke heated at 2100°C[25].

2.3.2 Reaction mechanism of the carbon fiber electrodes using the solvent PC/DME = 50/50

Cycling behavior was examined for the Li/carbon fiber cells using the PC/DME = 50/50 solvent at different Li/C values. The Li/carbon fiber cells were charged to a certain Li/C value, and the charge-discharge behavior at this Li/C value was examined with a depth of $\Delta Li/C$ = 0.004 and a current density of 0.375 $mAcm^{-2}$. Figure 2-5 shows a number of cycles as a function of Li/C value. The best rechargeability was obtained at Li/C = 0.1.

Poor rechargeability was observed both in shallower and deeper lithium storage ranges.

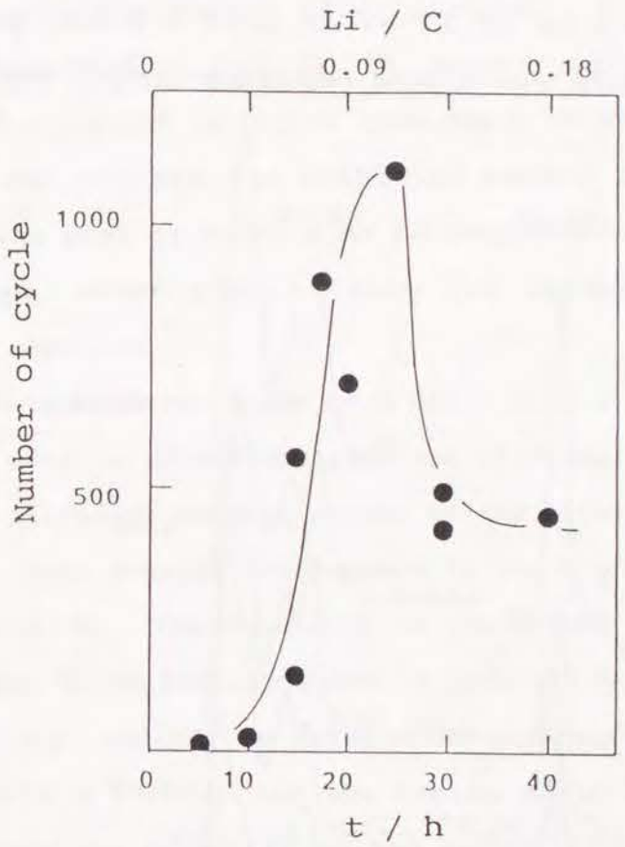

Fig. 2-5 Number of charge and discharge cycles as a function of charge time. The charge and discharge depth was 1 mAh/100mg.

The XPS spectra of the lithium 1s 1/2 state and the carbon 1s 1/2 state were measured for the samples charged with a current density of 0.375 $mAcm^{-2}$ in the PC/DME = 50/50 solvent at various

lithium storage ranges. Figure 2-6 shows the spectra for the carbon fiber M46 electrode. In the shallow lithiated region of Li/C = 0.045, the Li 1s 1/2 peak (E = 54.80 eV) is close to that of metallic lithium (E = 54.70 eV). The peak shifts from 54.80 eV at Li/C = 0.045 to 55.12 eV at Li/C = 0.09, where the Li/carbon fiber couple showed good rechargeability. The peak at

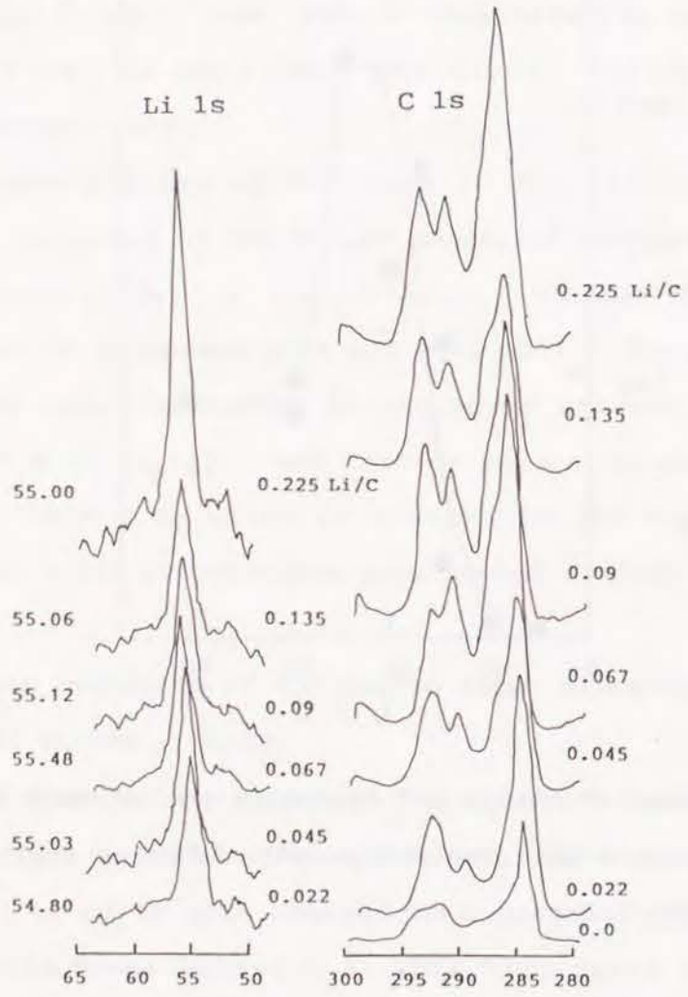

Fig. 2-6 XPS spectra of the carbon fiber M46 electrodes as a function of lithium storage level.

Li/C = 0.09 (E = 55.12 eV) may correspond to and intercalated lithium ion which participates in the reversible cell reaction. In a deeper lithiated range of Li/C = 0.225, the Li 1s peak shifts back to lower energy, corresponding to lithium metal deposition on the carbon fiber surface. The deep lithiated carbon fiber (0.067 < Li/C <0.225) shows a carbon 1s 1/2 spectra at E=286.3 eV, which is higher than the C 1s peak at E = 284.4 eV observed for the shallow lithiated carbon fiber (0 < Li/C < 0.045). The peak of E=286.3 eV corresponds to the carbon bound to lithium, which results from the reversible charge and discharge reaction.

The intercalation range of 0.067 < Li/C < 0.135 indicated by the X-ray data is consistent with the Li/C region of 0.04 - 0.135 where the different bonding states of the lithium and carbon were observed. This exactly corresponds to the highly reversible cell reaction region. The constancy in the c-axis parameter between Li/C = 0 and 0.067 indicates that a reaction occurs on the carbon fiber surface, because no lithium metal deposition was observed for 0 < Li/C < 0.135. For the region above Li/C = 0.135, the lithium metal is deposited on the carbon fiber surface, and no XRD peak shift was observed.

DTA-TG analyses were obtained on the carbon fiber electrodes charged with a current density of 0.375 $mAcm^{-2}$ in the solvent PC/DME = 50/50 in order to clarify the reaction mechanisms on heating which might reveal the charge products. Figure 2-7 shows the DTA-TG curves of the carbon fibers with different amounts of lithium stored. It is apparent from the curves that the reaction

mechanisms on heating the deep lithiated samples are different from those of the shallow lithiated samples; the weight loss with temperature, for example, is proceeded by two steps for the deep lithiated samples and by a single step for the shallow lithiated

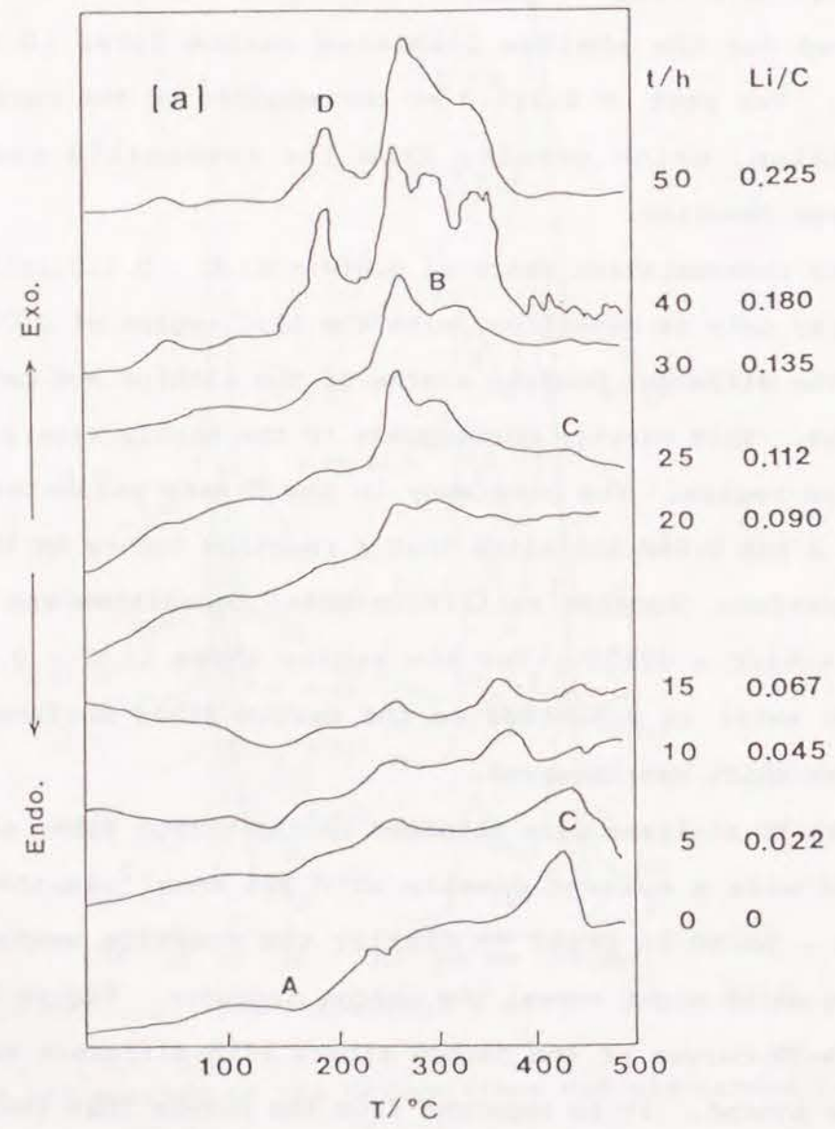

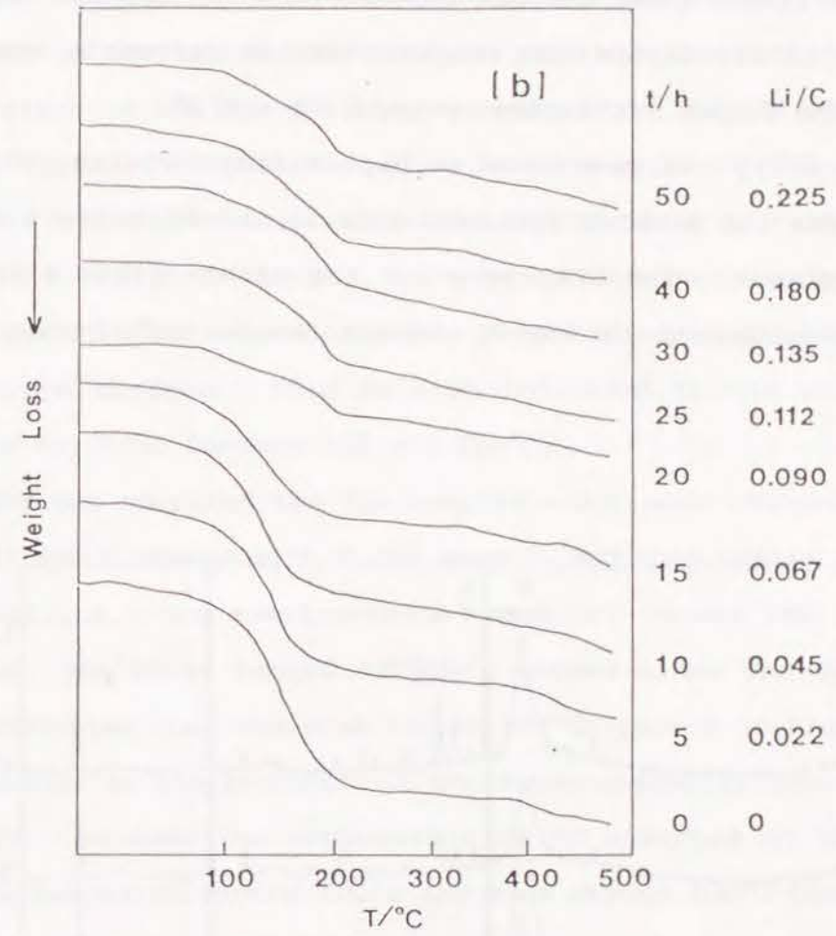

Fig. 2-7 DTA(a) and TG(b) curves for the carbon fiber M46 electrodes. The solvents were the mixture of PC/DME =50/50.

samples. The DTA curves are divided into three groups; Li/C < 0.067, 0.09 < Li/C < 0.135 and 0.18 < Li/C, which corresponds respectively to the surface reaction, the intercalation reaction, and lithium deposition ranges. Figure 2-8 shows XRD patterns of

the carbon fibers after the DTA-TG measurements; lithium fluoride was found in all lithiation ranges: lithium carbonate was only found in the deeper lithiation range, 0.09 < Li/C.

To clarify the reactions at higher temperatures, DTA was obtained for the samples immersed only in the PC solvent and in the DME solvent. The DTA curve for the carbon fiber electrode which was immersed in the PC shows a large endothermic peak

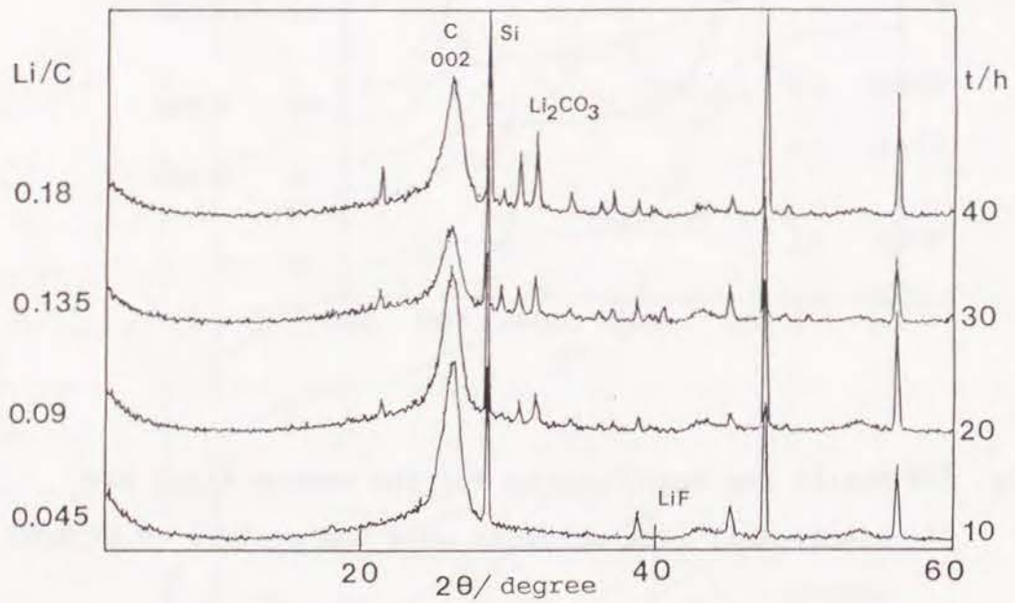

Fig. 2-8 XRD patterns of the carbon electrodes after DTA measurements.

between 150 and 250°C, corresponding to the evaporation of PC adsorbed on the carbon surface. No peak was observed due to the evaporation of DME for the sample immersed in the DME electrolyte by our method, because of the low boiling point of DME. The DTA curve of the sample immersed in the PC/DME 50/50 solvent is shown in Fig. 2-7(a)(0 h charge). The broad endothermic peak around 150°C(peak A) corresponds to the evaporation of PC adsorbed on the carbon surface. This is also indicated by the weight loss ion the TG curve between 100 and 200°C.

XRD was obtained for the samples which were charged to Li/C = 0.135 (30 h charge with 0.375 $mAcm^{-2}$) and then heated at higher temperatures. The samples heated at 170°C showed XRD lines due to LiOH, and those heated at 250°C showed lines due to Li_2CO_3. This indicates that the peak around 257°C (peak B in Fig. 2-7(a)) corresponds to the reaction of the intercalated lithium with the solvent. Because the evaporation of PC adsorbed on the carbon surface begins at around 100°C and ends around 200°C (see Fig. 2-7(a), 0 h charge), the lithium might react with the solvent evaporated from the surface or the solvent which is co-intercalated into the carbon layer. Lithium fluoride was formed only after the samples were heated at 500°C, indicating that the small peaks around 400°C (peak C in Fig. 2-7(a)) corresponds to the LiF formation from Teflon and lithium . The DTA curves for the deep lithiated samples 0.18 < Li/C show large peaks around 180°C (peak D in Fig. 2-7(a)), which might correspond to a reaction of the lithium deposited on the carbon surface and the electrolyte.

Consequently, the reactions on heating are summarized as follows.

1)For the shallow lithiated samples with 0< Li/C < 0.09, the solvent adsorbed on the carbon surface evaporates between 100 and 200°C, and lithium fluoride is formed above 400°C by a reaction of Teflon and lithium.

2)In addition to the above reaction, another reactions proceed for the samples with 0.09 < Li/C < 0.135. The intercalated lithium reacts with the solvent forming Li_2CO_3 around 250°C. The solvent adsorbed on the carbon fiber surface might not be the source of this reaction, because the evaporation proceeds between 100 and 200°C. This suggests that the solvent might co-intercalate with lithium into the carbon layer.

3)For the samples with 0.18 < Li/C, lithium deposited on the carbon surface reacts with the adsorbed solvent below 200°C forming Li_2CO_3.

The reaction mechanism has been determined by XRD, XPS and DTA-TG measurements for the carbon fiber electrodes in the PC/DME = 50/50 solvent. The results were well consistent with each other and are summarized as follows.

1) 0 < Li/C < 0.067: The lithium reacts with carbon fiber surface forming a surface layer compound.

2) 0.067 < Li/C < 0.135: Lithium intercalates into the carbon fiber layer and forms the intercalation compound. This reaction is highly reversible.

3) 0.135 < Li/C: Metallic lithium deposits on the surface of the carbon fiber.

We have previously reported the reversible lithium-storage of carbons such as the thermal decomposition products of PPCA[9, 10]. Cycling behavior was examined in the Li/decomposition products of PPCA ad different Li/C values with a charge-discharge cycle depth of ΔLi/C = 0.004. Efficient rechargeability was obtained within a narrow range of 0.157 < Li/C < 0.161, whereas in both shallower and deeper ranges, the rechargeability was extremely poor. These results are similar to those observed for the Li/carbon fiber cells. The X-ray data on the thermal decomposition products of PPCA showed no evidence of whether the reaction proceeded by the intercalation process or by other mechanisms, because the thermal decomposition products of PPCA gave very broad X-ray diffraction peaks. However, the reaction mechanism could be considered by the XPS data of both the carbon fiber M46 and the thermal decomposition products of PPCA. The XPS data obtained for the thermal decomposition products of PPCA are as follows[10]:

1) the binding energy of Li 1s 1/2 peak (E = 54.89 eV) at shallow lithiation range is close to that of metallic lithium,

2) the peak shifts to higher energies with lithiation, and the highest energy (E = 55.49 eV) was observed around Li/C = 0.21, where the Li/decomposition products of PPCA showed good reversibility,

3) the lithium 1s peak shifts back to a lower energy in the deeper lithiated range, suggesting lithium metal deposition.

The XPS data observed for the decomposition products of PPCA are quite consistent with those for the carbon fiber M46. This

indicates that the reversible cell reaction of the Li/thermal decomposition of PPCA proceeds by the lithium intercalation mechanism.

2.3.3 Lithium-Carbon fiber composite anode

The Li/carbon fiber M46 cells show good reversibility due to the lithium intercalation mechanism. However, the low lithium storage capacity of the cell might be a disadvantage if the carbon fiber is used for the anodes of practical lithium secondary cells. To rectify the disadvantage, we tried to use anodes which consist of both lithium metal and the carbon fiber. In the "composite anode", lithium metal might be used as lithium source and the carbon fiber might improve the charge and discharge property. Cells of this type were examined with chromium oxide cathodes, which have excellent cathodic properties[19]. The charge curves at a current density of 0.375 $mAcm^{-2}$ indicated no difference in curves between the cells with a lithium metal anode and those with a lithium-carbon composite anode. Although the carbon fiber electrode was placed between the lithium source and the separator, the lithium diffusion through the cell was not blocked by the carbon fiber layer.

The charge-discharge properties were examined both for the Li/Cr_3O_8 and the composite-anode/Cr_3O_8 cells. It is apparent in Fig. 2-9 that the composite anode cell showed more than 170 cycles; twice as many as in the Li/Cr_3O_8 cell. Although the anode of the Li/Cr_3O_8 cell was fully covered with the lithium dendrites, only a small amount of dendrites was formed in the

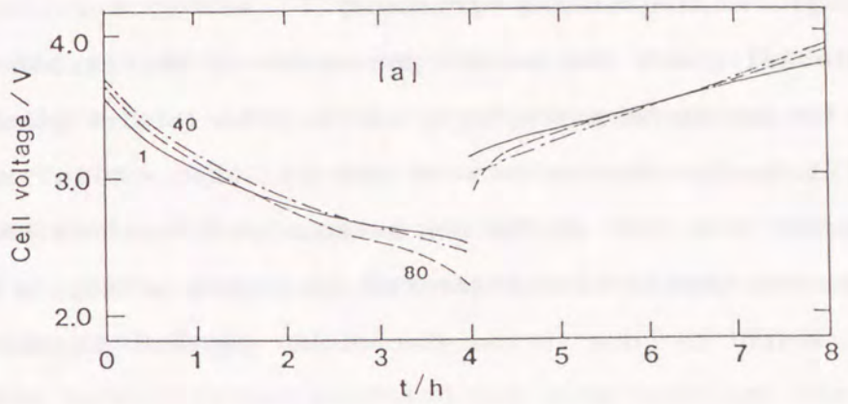

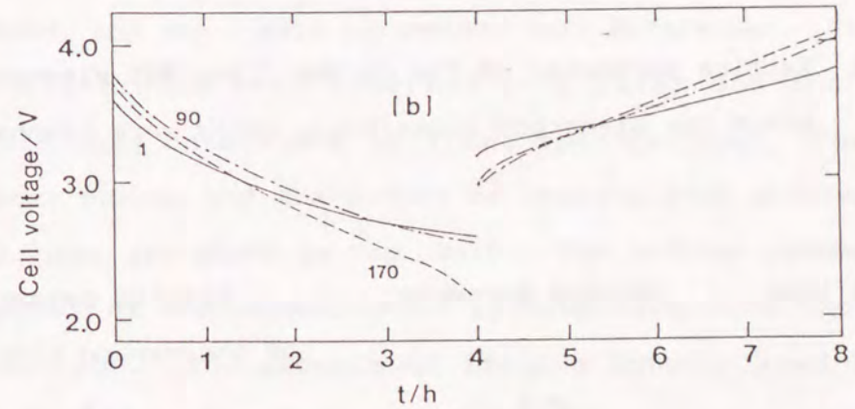

Fig. 2-9 Charge and discharge curves for the cells, Li/Cr_3O_8 (a) and Li-M46/Cr_3O_8(b).

composite-anode/Cr_3O_8 cell after the cycle test. The lithium-carbon composite anode reduced the dendrite formation, and thereby improved the cycling efficiency.

Table 2-1 shows the c-axis parameter of the carbon fiber used for the composite anode/Cr_3O_8 cells. The lattice parameters measured just after the cells were made (at Li/C = 0 in Table 2-1) are larger than that of the non-intercalated carbon fiber M46. This indicates that lithium intercalation occurs without a charge process, which is due to the electrical contact between the

Table 2-1 Lattice parameter of the carbon fiber M46 electrodes after the Li-carbon fiber/Cr_3O_8 cells were discharged.

Discharge time	Lattice parameter	Lattice parameter of the carbon fiber M46
t/h	c/A	c/A
0	7.067	
10	7.078	
15	7.050	6.842
20	7.050	
50	7.045	

carbon fiber and the lithium metal. The c-axis parameter decreases slightly as the cells were discharged from 0 to 50 hr, indicating a gradual lithium deintercalation. The lattice parameter was measured after the second charge and discharge cycle; the c-axis value of 7.134 A is in good agreement with that of the carbon fiber where the maximum amount of lithium is intercalated. This suggests therefore that the intercalation reaction participates in the charge-discharge process of the composite anode/Cr_3O_8 cells.

The intercalation reaction was also examined for the Li-carbon fiber/Cr_3O_8 cells using various PC/DME ratios. The cells were left for at least 24 h at room temperature after being assembled, and the c-axis parameters were determined. The carbon fiber electrodes were immersed into water and the lithium contents were determined by flame spectroscopy. The c-axis parameter change and the amount of intercalated lithium in the carbon fiber are shown in Fig. 2-10. The lattice parameters and the amount of the intercalated lithium vary with the solvent compositions. The amounts of lithium intercalated into the carbon in the 0/100, 25/75, and 100/0 solvents were smaller than those observed in the 50/50 and 75/25 solvents. However, the c-axis expansion vary little with the solvent composition except for the PC/DME = 75/25 solvent. This suggests that the size of the intercalated species is larger in the 0/100, 25/75, and 100/0 solvents than in the 50/50 solvent. The co-intercalation of the solvent with lithium has been previously reported for the highly oriented pyrographite and carbon fiber[30-32]; the solvated

lithium intercalates into the carbon layer and forms $Li(DME)_yC_{18}$, for example, by an electrochemical reduction in the DME

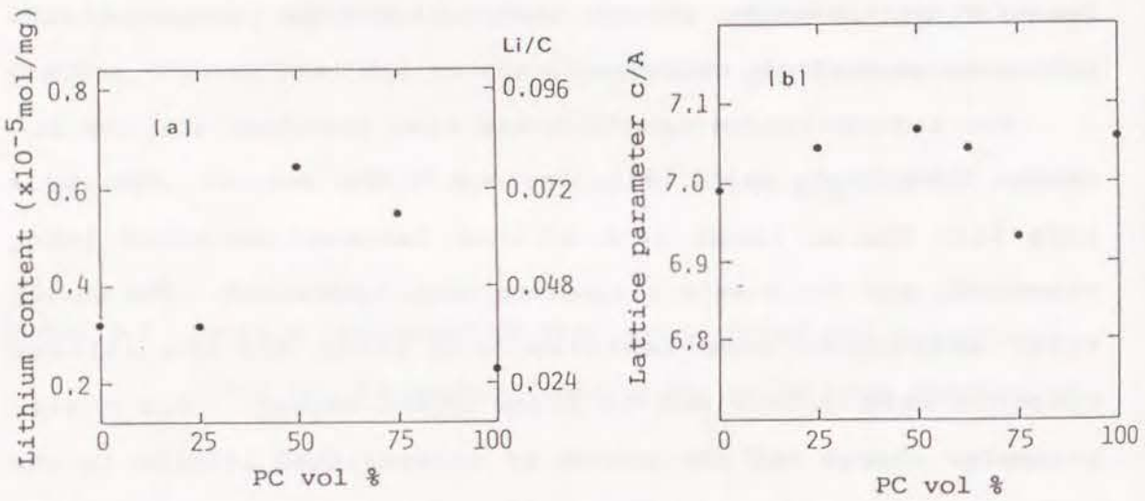

Fig. 2-10 (a) Total amount of lithium in the carbon fiber M46 electrodes as a function of PC:DME volume ratio. The amount of lithium per 1 mg carbon fiber is indicated.

(b) Lattice parameter change of the carbon fiber as a function of PC:DME volume ratio.

solvent[31]. The alkaline metals also co-intercalated in DME and DMSO (dimethyl sulfoxide) solvents[30]. The lithium intercalation in the mixed solvent such as PC and DME has not been reported previously. However, the results obtained here suggests the solvent co-intercalation for the 0/100, 25/75, and 100/0 solvents.

The charge and discharge mechanism of the composite anode cells is summarized as follows: 1) before discharge, lithium intercalates into the carbon fiber, 2) on discharge, the lithium in the carbon fiber deintercalates gradually, 3) on charge, the lithium intercalates again into the carbon layer and the c-axis expands to its maximum value.

2.4 Conclusion

The following information has been obtained in this study; 1) lithium intercalates into the carbon fiber M46 after an irreversible capacity loss of the first charge. The intercalation reaction is highly reversible. The first charge mechanism, which has been attributed to the formation of a passivating film at the carbon surfaces, is quite complicated; the mechanism changes with the electrolyte compositions and with charge current densities. 2) Lithium-carbon fiber composite anodes reduce dendrite formation in lithium secondary cells. The reversible reaction of the composite anodes is attributed to lithium intercalation into the carbon fiber.

Recently, two battery companies, Moli Energy Ltd. and Sony Energytec Inc. have announced the commercialization of Li^+ ion rechargeable batteries using a carbon intercalation compound as the negative electrode[33-35]. Cathodes materials suitable for "rocking-chair" rechargeable batteries have also been reported[36-38]. Carbon now appears to be a promising material for lithium secondary batteries. The carbon fiber in the present study might have merit in battery processing because it is easier to make into sheets for anodes. The reaction mechanism during the first charge is quite complicated and depends on the electrolyte, charge current densities and also type of carbon fibers employed. The search for the best combination of the carbon fiber and the electrolyte is now being addressed.

References

1. A.N.Dey, J.Electrochem.Soc., 118, 1547(1971).
2. I.Epelboin, M.Forment, M.Garreau, J.Thevenin and D.Warin, J.Electrochem.Soc., 127, 2100(1980).
3. J.Rene van Beek and P.J.Rommers, J.Power Sources, 7, 595 (1978).
4. J.L.Goldman, R.M.Mank, J.H.Young and V.R.Koch, J.Electrochem. Soc., 127, 1461(1980).
5. D.W.Murphy and J.N.Carides, J.Electrochem.Soc., 126, 349(1979).
6. M.Lazzari and B.Scrosati, J.Electrochem.Soc., 127, 773(1980).

7. J.M.Tarascon, J.Electrochem.Soc., 132, 2089(1985).
8. J.J.Auborn and Y.L.Barberio, J.Electrochem.Soc., 134, 638 (1987).
9. O.Yamamoto, Y.Takeda, R.Kanno, K.Nakanishi and T.Ichikawa, Proc. J.Electrochem.Soc., 88, 754(1988).
10. R.Kanno, Y.Takeda, T.Ichikawa, K.Nakanishi and O.Yamamoto, J.Power Sources, 26, 535(1989).
11. M.Mohri, N.Yanagisawa, Y.Tajima, H.Tanaka, T.Mitate, S.Nakajima, M.Yoshida, Y.Yoshimoto, T.Suzuki, and H.Wada, J.Power Sources, 26, 545(1989).
12. R.Fong, U.von Sacken and J.R.Dahn, J.Electrochem.Soc., 137, 2009(1990).
13. A.Brenner, J.Electrochem.Soc., 118, 461(1971).
14. J.S.Dunning, W.H.Tiedemann, L.Hsueh and D.N.Bennion, J.Electrochem.Soc., 118, 1886(1971).
15. S.L.Deshpande and D.N.Bennion, J.Electrochem.Soc., 125, 687(1978).
16. H.Hayashi and T.Fujii, Japan Pat. 154763(1984).
17. M.Miyabayashi and A.Itsubo, Japan Pat. 147456(1986).
18. For example, R.C.Reynolds, Jr., in "Modern Powder Diffraction", eds. by D.L.Bish and J.E.Post, Mineralogical Society of America, p.145(1989).
19. Y.Takeda, R.Kanno, Y.Tsuji and O.Yamamoto, J.Electrochem. Soc., 131, 2006(1984).
20. T.Sato, H.Ikeda, Y.Matsuda, and H.Tamura, J.Appl. Electrochem., 6, 85(1976).
21. Y.Matsuda, Y.Ouchi, and H.Tamura, J.Appl.Electrochem., 4, 53

(1974).

22. W.R.Mckinnon and J.R.Dahn, J.Electrochem.Soc., 132, 364 (1985).

23. M.Arakawa and J.Yamaki, J.Electroanal.Chem., 219, 273(1987).

24. D.Guerard and A.Herold, Carbon, 13, 337(1975).

25. J.R.Dahn, R.Fong, and M.J.Spoon, Phys.Rev., B42, 6424(1990).

26. E.Peled, J.Electrochem.Soc., 126, 2047(1979).

27. D.Aurbach, M.L.Daroux, P.W.Faguy, and E.Yeager, J.Electrochem.Soc., 134, 1611(1987).

28. D.Aurbach, M.L.Daroux, P.W.Faguy, and E.Yeager, J.Electrochem.Soc., 135, 1863(1988).

29. D.Aurbach and Y.Gofer, J.Electrochem.Soc., 138, 3529(1991).

30. J.O.Besenhard, Carbon, 14, 111 (1976).

31. J.O.Besenhard, H.Mohwald and J.J.Nickl, Carbon, 18, 399 (1980).

32. J.O.Besenhard and H.P.Frits, Angew.Chem. Int.Ed. Dngl., 22, 950(1983).

33. J.R.Dahn, U.von Sacken, and R.Fong, Abstract 42, p.66, The electrochemical Society Extended Abstracts, Vol. 90-2, Seattle, WA, October 14-19(1990).

34. T.Nagaura, 4th International Rechargeable Battery Seminar, Deerfield Beach, Florida(1990).

35. Y.Nishi, H.Azuma, and A.Omaru, U.S.Pat. 4,959,281(1990).

36. J.R.Dahn, U.von Sacken, M.W.Juzkow, and H.Al-Janaby, J.Electrochem.Soc., 138, 2207(1991).

37. J.M.Tarascon and D.Guyomard, J.Electrochem.Soc., 138, 2864(1991).

38. D.Guyomard and J.M.Tarascon, J.Electrochem.Soc., 139, 937(1992).

Chapter 3. Effect of Microtextures of Carbon Materials on Charge-Discharge Characteristics for Mesophase-Pitch-Based Carbon Fiber

3.1 Introduction

During the 1970's, a substantial number of lithium primary cells have been commercialized. However, rechargeable lithium cells are still under development, because of difficulties in charging the lithium electrode. The difficulties come from the reaction of the as-plated lithium with the electrolytic solution. A protective insulating film is formed on the surface of lithium metal, and the morphology deteriorates and the plate-strip efficiency decreases on cycling[1,2]. Many approaches have been taken to improve the reversibility of the lithium anode. One of them is to use lithium alloy. The most serious problem of the alloy electrodes is concerned with volume changes during cycling[3]. Recently, a lithium electrode covered by carbon materials has been proposed as an attractive anode, because of relatively small volume changes and excellent cycling behavior[4,5,6]. A potential disadvantage of this type electrode, however, was low energy and power densities. Graphitic carbon forms a lithium insertion compound LiC_6 at its maximum composition, in which 0.16 mol% lithium per carbon intercalates into the interlayer spaces uniformly. This structure is the 1st

stage structure. The specific and volume charge densities of LiC_6 are 339 $mAhg^{-1}$ and 149 $mAhml^{-1}$, which are acceptable for practical applications if good reversibility on extended cycling is available.

Carbon materials have large variations in their structure and texture[7,8], depending on their preparation processes, precursor materials, etc. These structures and textures can be characterized by transmission electron microscopy, X-ray diffraction(XRD), scanning electron microscopy(SEM), Laser Raman scattering, and galvanomagnetic properties. It is, therefore, important to use well-characterized carbon materials for electrochemical studies and to select the most suitable carbon materials for the anode of lithium secondary batteries. In Table 3-1, coulomb densities for various types of carbon are summarized along with XRD data. The coulomb density depends on the d_{002} spacing, which is a measure of the crystallinity[9]. However, it can not be concluded from Table 3-1 that the crystallinity of carbon materials is the only important factor for the specific charge density. The macroscopic structure such as the texture is also an important factor. In this study, various types of mesophase-pitch-based carbon fibers which have different textures in cross-section were examined for use in lithium cells with organic electrolyte solutions. The effect of texture on lithium intercalation and deintercalation behavior is discussed.

Table 3-1. Coulomb densities and crystal parameters for various carbon materials.

Carbon Material	Crystal Parameter		Capacity	Ref.
	d_{002} / A	Lc / A	/mAhg^{-1}	
thermally decomposed carbon (PPCA*1)	(amorphous)		145	17
thermally decomposed carbon (benzene)	3.49	100	300	18
PAN-based carbon fiber (M46*2)	3.42		80	17
pitch-based carbon fiber*3	3.39	237	180	9
pitch-based carbon bead	3.36	635	250	19
thermally decomposed carbon (furfuryl alcohol resin)			320	20
artificial graphite	3.357	600	100	19
Kish graphite*4	3.354	>1000	0	9

*1 PPCA : Poly-2-chloro-1-phenylacethylene
*2 made by Toray Industries, Inc.
*3 made by Nippon Steel, Co.
*4 made by Toshiba Ceramics, Inc.

3.2 Experimental

Four types of mesophase-pitch-based carbon fibers heat-treated at 2600 or 2800°C were obtained from Hokkaido

University[10]. They are different in their orientation of the graphite layers, which can be controlled by changing the spinning temperature. The SEM micrographs of cross-section of the carbon fibers used are shown in Fig. 3-1. The cross-sections of the samples A, B, C and D can be expressed as radial texture with wedge, radial texture with fine zig-zag layers, double texture(the core part has an A-like texture and the edge part has a B-like one), and concentric(onion-like) texture, respectively. The diameters of the carbon fibers were about 10 μm. The lattice

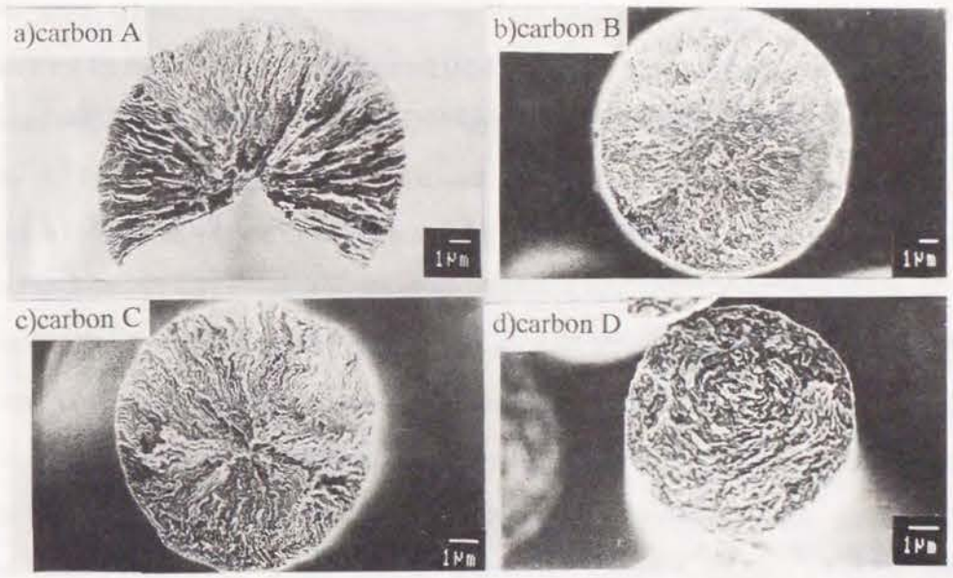

Fig. 3-1 SEM micrographs of cross-sections of carbon fibers A, B, C and D.

parameters of the fibers are compared with graphite in Table 3-2[11]. In this table, the graphitization degree, P1, was calculated from the measured d_{002} value according to the method derived by B.E.Warren[12]. A magnetoresistance($\Delta\rho/\rho$) effect means the change in the electrical resistivity of a conductor with magnetic field. In general, this value is positive for a graphitic structure but negative for a turbostratic one[11]. The c-spacing, P1 and $(\Delta\rho/\rho)_{cr}$ values of carbon fiber A show the highest degree of graphitization among four fibers. Type A was

Table 3-2. The texture and crystal parameters of mesophase-pitch-based carbon fibers.

	Texture	c / A	Lc(002) / A	P_1	$(\Delta\rho/\rho)$cr / %
Carbon Fiber A	Radial with wedge	6.74	350	0.35	2.99
Carbon Fiber B	Radial	6.83	170	0.26	-1.46
Carbon Fiber C	double	6.81	180	0.29	-1.15
Carbon Fiber D	concentric	6.83	180	0.25	-1.08
Graphite		6.70			

easily cleaved radially, as a result of the highly oriented two-dimensional texture. The other three fibers have a less graphitized structure than A and they all have very similar crystal parameters although their textures are very different.

A three electrode system was applied to measure charge-discharge behavior. Lithium sheets were used as reference and counter electrodes. Carbon fibers were cut into 15 mm lengths and their weights were carefully measured by a microbalance. One end of each fiber was held vertically between two nickel plates as a current collector. The other end of the fibers was soaked into the electrolyte, avoiding contact of the Ni plates by the electrolyte. The electrolyte was a solution of 1 M $LiClO_4$ dissolved in 1:1 PC-THF mixed solvent. Excess amounts of solvent were always used to get rid of the influence of compositional change of the electrolyte. All carbon fibers were well dried before use. Lattice parameter measurements were performed using an X-ray diffractometer(Rigaku Rotaflex RU-200B) with CuKα radiation. The data were collected at $1°min^{-1}$ in the range 3°-70°. The smoothing, background reduction and CuKα2 stripping were done with a computer program. X-ray photoelectron spectra(XPS) were measured with a Shimadzu ESCA750 spectrometer with a MgKα X-ray source(8kV, 30 mA) operated at a pressure of $1x10^{-8}$ torr. Au was used as a reference to correct for charging. The morphology of the carbon fibers was observed by means of a scanning electron microscope(Hitachi S-2300S). The construction of the cell, preparation of samples for XRD measurement and all other procedures were performed in an Ar atmosphere dry box. Relative

humidity of Ar gas in the dry box was kept less than 0.8 %.

3.3 Results and Discussion

It is well known that the catalytic activity of edge surfaces of carbon materials may play an important role in some cases[13,14], because there are special functional groups associated with the edges. These groups may influence lithium intercalation into carbon fibers. In order to characterize these groups, XPS spectra of carbon fibers A, B, C and D were measured. As shown in Fig. 3-2, there is no significant difference among four spectra. Only the C1s and a small O1s peak are observed. The binding energy of the C1s orbital is 284.4, 284.2, 284.3, and 284.3 eV for carbon fibers A, B, C and D, respectively when referenced to the Au peak. These binding energies are in good agreement with that of graphite, 284.3 eV[15]. The oxygen peak in these spectra is thought to be due to adsorbed oxygen. Consequently, these XPS spectra show that the surface of the four kinds of carbon fibers are very similar.

Electrochemical characteristics of the carbon fibers were surveyed by cyclic voltammetry. Figure 3-3 shows the initial cyclic voltammograms at carbon fibers A, B, C and D where the scanning speed was 600 $mVmin^{-1}$. Carbon fiber A shows a cathodic peak at around 0.5 V. This cathodic reaction is irreversible because no anodic peak is observed. Moreover, this peak disappeared on the second cycle. Fibers B, C and D show the

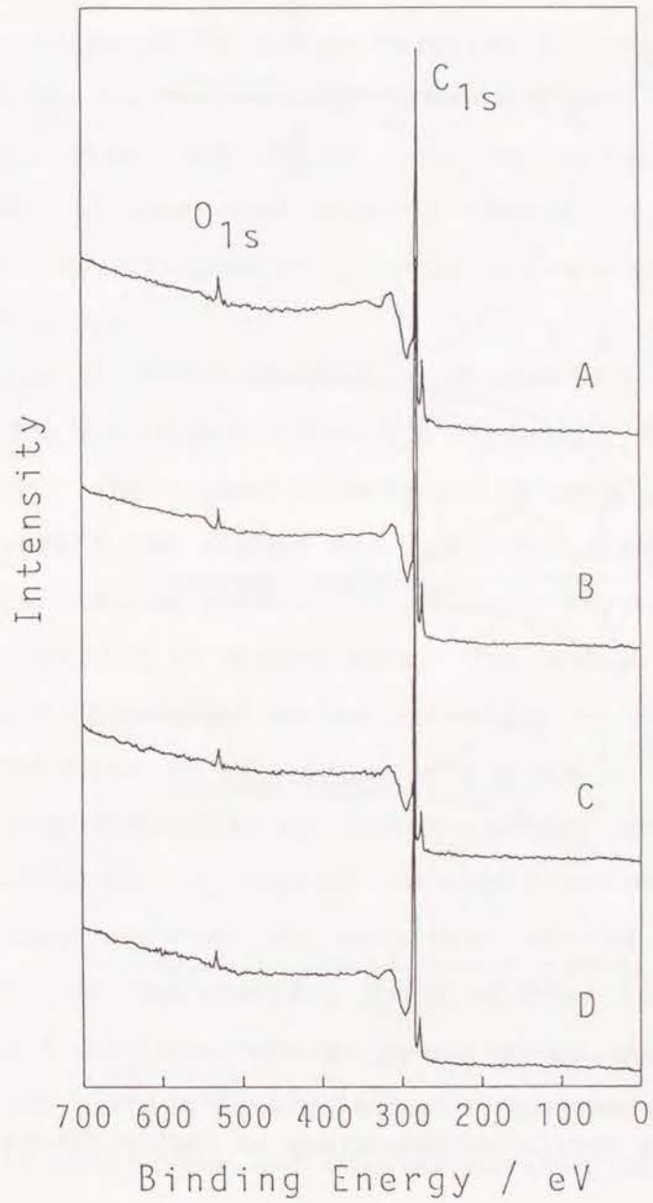

Fig. 3-2 XPS spectra of carbon fibers A, B, C and D before charge process.

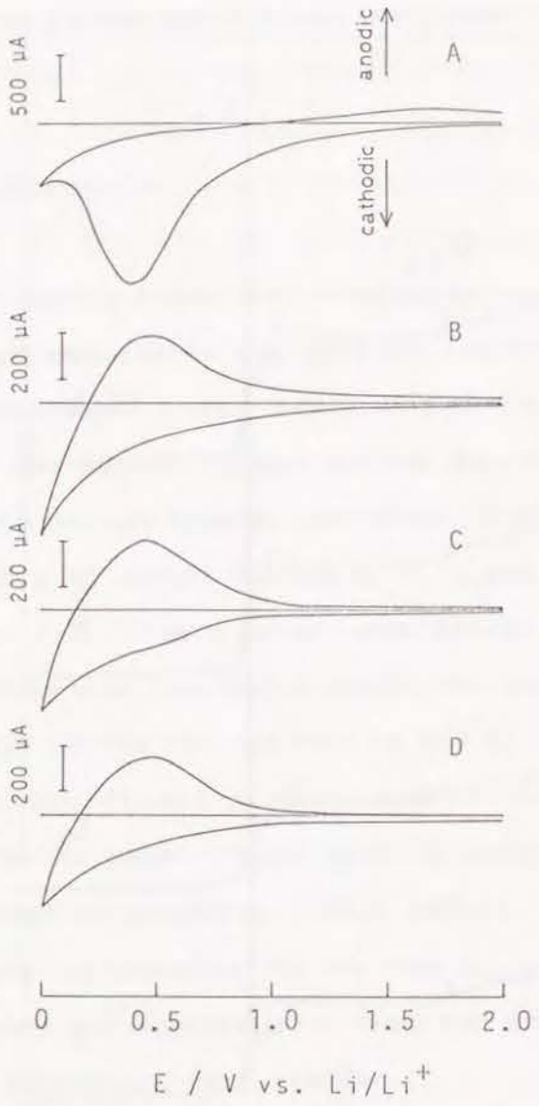

Fig. 3-3 The 1st cyclic voltammograms of carbon fibers A, B, C and D.

cathodic peak at 0 V and a broad anodic peak at 0.5 V, and they all have similar profiles. Lithium intercalation and deintercalation occurs reversibly at these two potentials. In a

rapid potential sweep such as during the cyclic voltammogram, only the surface of the active material is utilized for charge-discharge. So the differences between A and the other carbon fibers are probably because of their texture on the edge of the fiber. This is consistent with the observation that only carbon A has highly crystallized and sharply oriented surface texture as shown in Fig. 3-1.

The charge (intercalation) - discharge (deintercalation) behaviors for the carbon fibers are shown in Fig. 3-4(a), (b), (c), and (d). The current density was 30 μAmg^{-1} and the cut off voltages were 0 for charge and 3.5 V for discharge. Fiber A shows a long charge potential plateau at around 0.8 V, but the discharge capacity is almost zero. The charge capacity of 650 $mAhg^{-1}$ would correspond to the formation of the compound LiC_3 which is not known as an intermediate phase of the Li-C system. The high charge potential and excess capacity more than 339 $mAhg^{-1}$ corresponding to LiC_6 suggest the occurrence of an irreversible side-reaction such as decomposition of the electrolyte on carbon[16]. At the starting point of this study, the radial texture of this fiber was believed to be the most suitable structure for lithium intercalation. The poor reversibility of lithium intercalation and deintercalation on fiber A may be explained by the SEM observations in Fig. 3-5. Figure 3-5(a) shows electron micrographs of fiber A before and after charging. Apparently the fiber after charge no longer keeps its original structure. As mentioned in the experimental section, this carbon fiber is easily cleaved like graphite owing to its highly

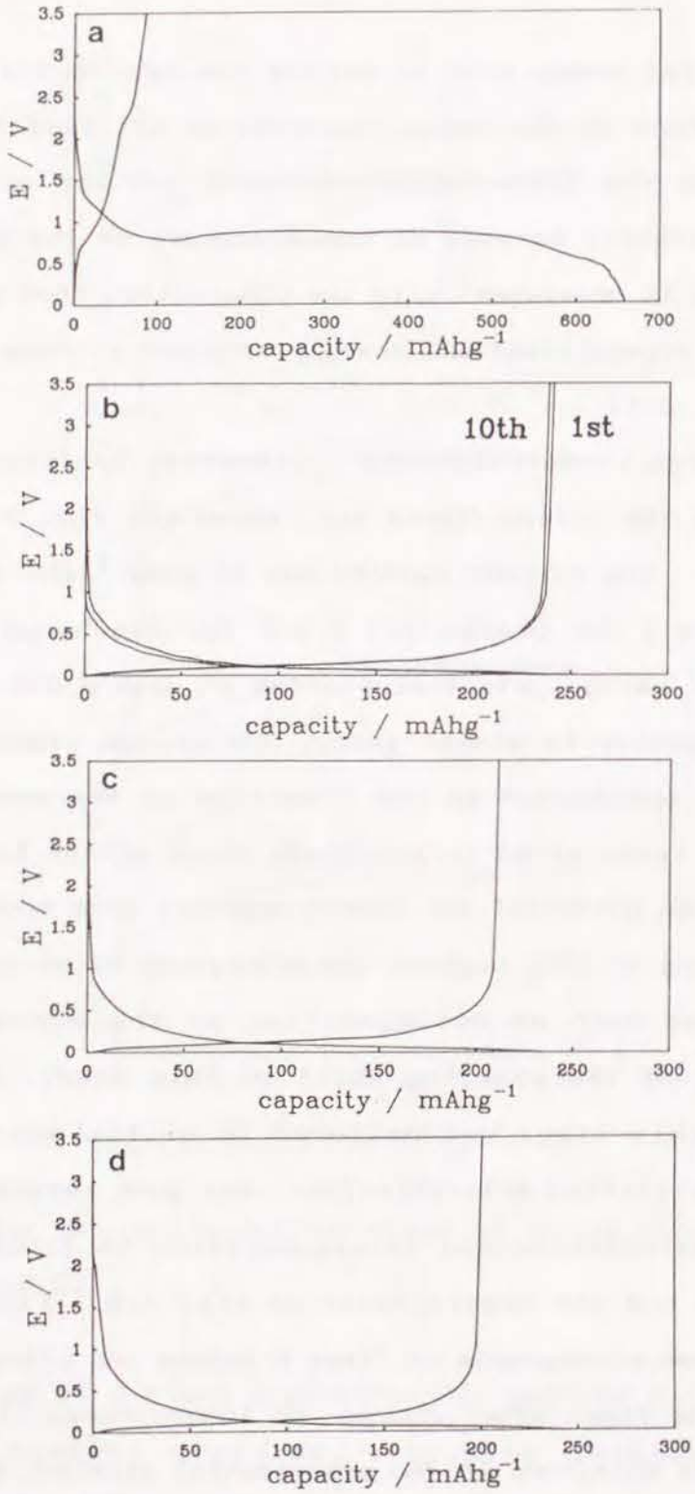

Fig. 3-4 The charge-discharge behaviors of carbon fibers A, B, C and D at a current density of 30 μAmg^{-1}.

a) before charge

after charge

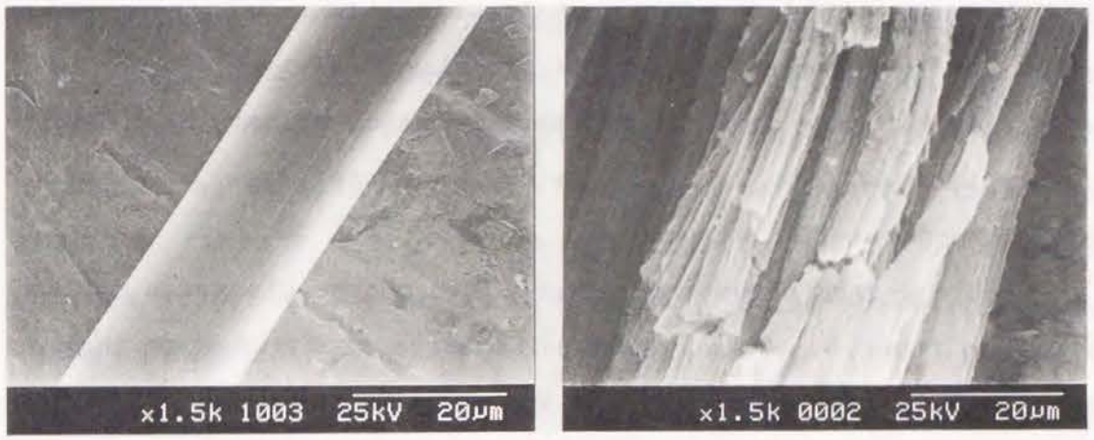

b) before charge

after charge

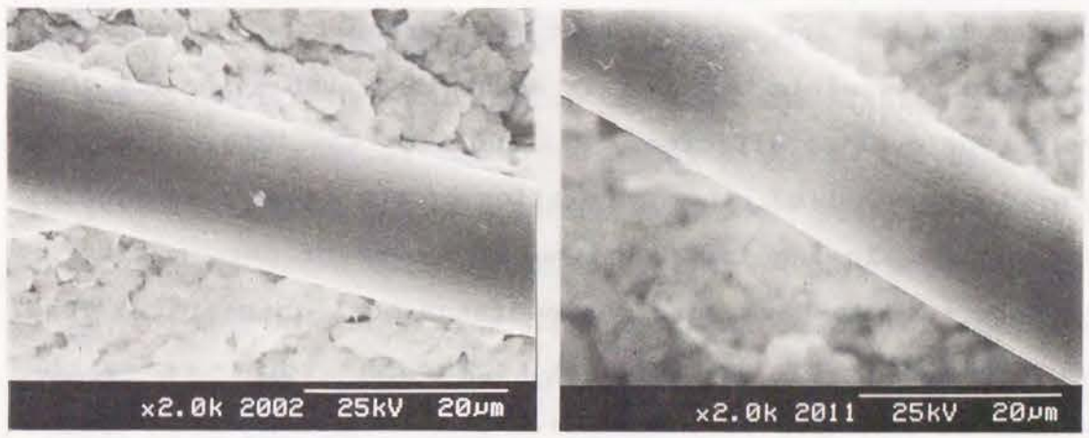

Fig. 3-5 SEM micrographs of carbon fibers A, and B before and after charge process.

oriented radial texture. It is possible to explain that this cleavage results from solvent co-intercalation which generally causes the large expansion of the interlayer space. However, it is difficult to say from our XRD study whether or not the solvent co-intercalates into it because the products after the charge had an amorphous-like structure.

Figure 3-4(b) shows the 1st and 10th charge-discharge cycles of carbon fiber B. These charge-discharge profiles show that a reversible lithium intercalation and deintercalation occurs. The charge-discharge cycling efficiency, which was defined as the ratio of the charge and discharge capacity, was 96 % for the 1st cycle. The capacity was about 240 $mAhg^{-1}$ which corresponds to about 70 % of the theoretical value, supposing the formation of LiC_6 as 100 %. The cycling test for carbon fiber B indicates that good reversible behavior is maintained even after the 10th cycle; the cycling efficiency was 100 % on the 10th cycle. As shown in Fig. 3-1(b), the orientation of the fiber B was radial with a fine zig-zag layer so the structure of carbon fiber B could be said to have some three-dimensional character. This characteristic of the texture is thought to increase the mechanical strength of the fiber. The SEM observation of the charge products of fiber B is shown in Fig. 3-5(b). No differences are observed before and after charge, which is a striking contrast to carbon fiber A. The cleavage of the fiber is prevented by the three-dimensional network which acts as a bridge between carbon layers. This carbon fiber may become a candidate for an anode for a lithium secondary battery.

Figures 3-4(c) and (d) show the charge-discharge behaviors of carbon fibers C and D, respectively. The voltage profiles are similar to that of carbon fiber B. The cycling capacities for fibers C and D were a little lower than that for carbon B. The cycling efficiency of the 1st cycle is 90% for fiber C and 83% for fiber D. The SEM observations show no significant change of structure before and after the 1st charging, as the same as carbon fiber B.

From these results, it can be said that the lithium cycling behavior of these carbon fibers depends on two factors. One is the mechanical strength of the fibers. SEM observations show fiber A has a texture which can easily be broken. Fiber C also has the possibility of being destroyed after many cycles because the core part of fiber C is the A-like texture. The other factor is the crystal orientation which controls the lithium diffusion into the inner part of the fiber. For example, the concentric texture (type D) has the disadvantages that lithium cannot be easily transferred from the surface. The results of carbon D does not show a much worse charge-discharge performance than carbon B. This implies that the crystallite size is not large enough to effect the lithium diffusion.

The change in c-spacing during the charge-discharge process was studied by XRD. Samples were charged and discharged galvanostaticaly, and then the circuit was opened for one day. The XRD measurements were carried out under an Ar atmosphere. Figure 3-6 shows the variation of the (002) peak of fiber B in the 1st cycle on various lithium intercalation levels. The 002

peak at ca. 26.1° moves to lower angles as intercalation increases. This behavior results from the expansion of the interlayer space along the c-axis, which proves that lithium is

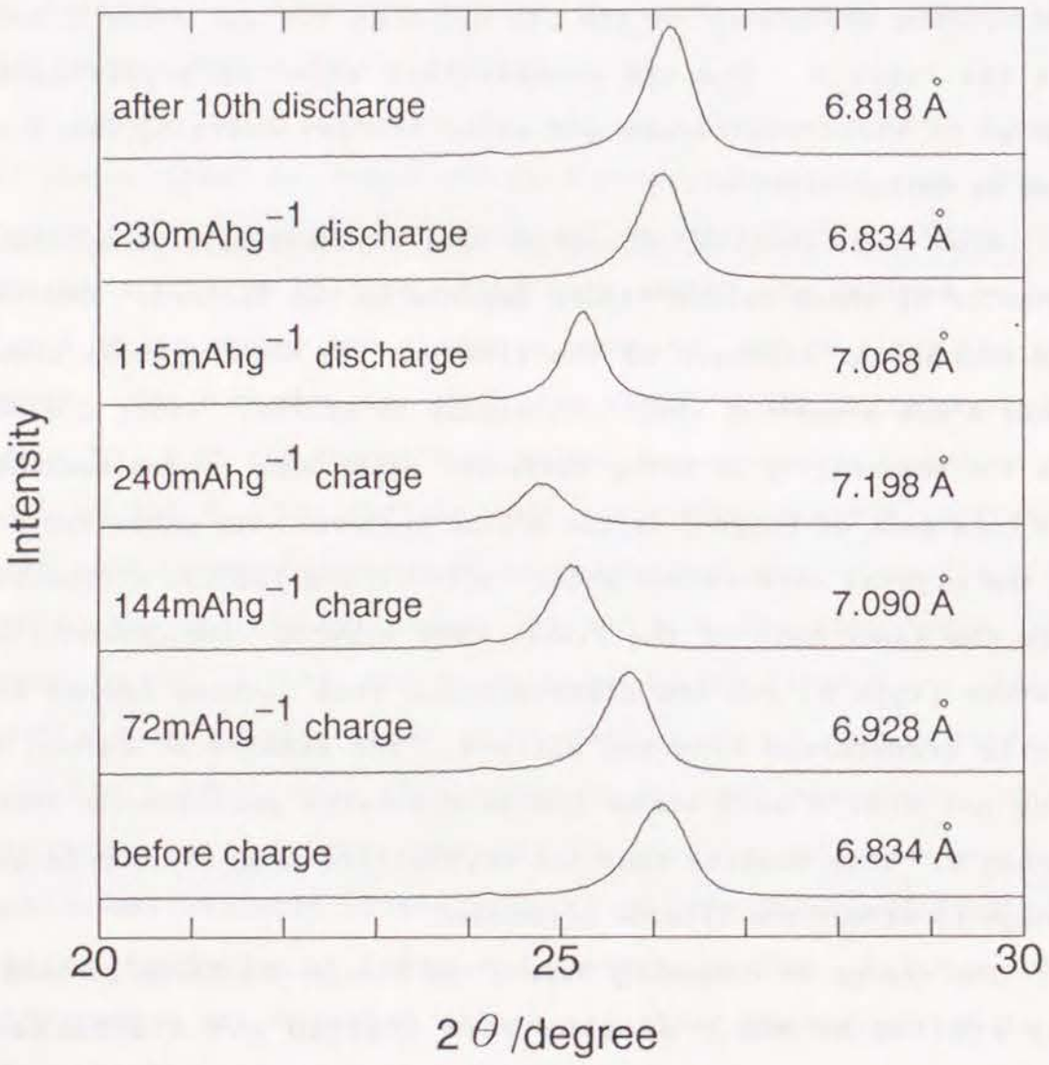

Fig. 3-6 XRD patterns of carbon fiber B during the 1st charge-discharge cycle.

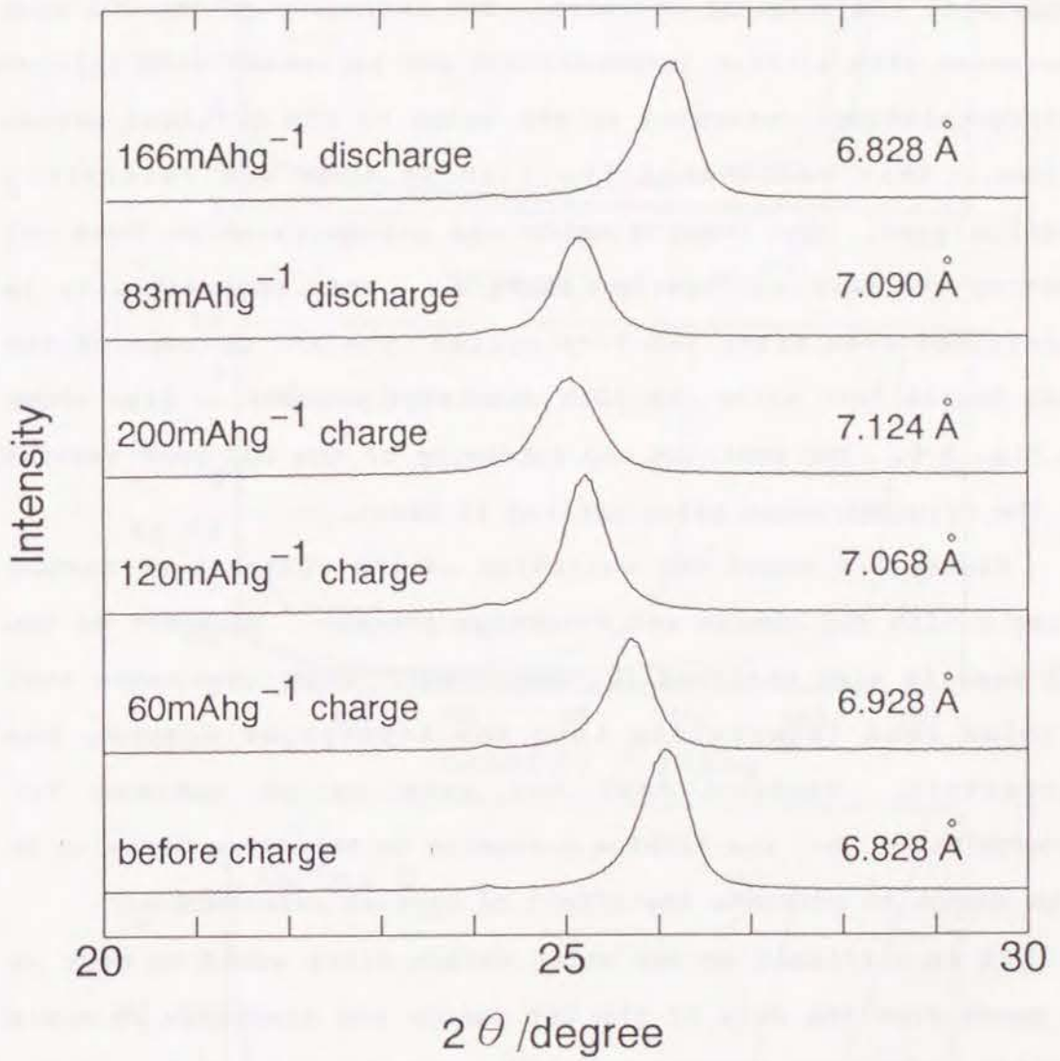

Fig. 3-7 XRD patterns of carbon fiber D during the 1st charge-discharge cycle.

really intercalated into the interlayers of the carbon fiber. Upon deintercalation, the 002 peak moves to higher angles and returns to its original position. The intensity of the 002 peak decreases with lithium intercalation and increases with lithium deintercalation, returning to the value of the original carbon fiber. This means that the lithium ions are reversibly intercalated. The intercalation and deintercalation does not destroy the matrix of carbon fiber B. This reversibility is maintained even after the 10th cycle. The XRD pattern of the same sample just after the 10th discharge process is also shown in Fig. 3-6. The position and intensity of the 002 peak returns to the original value after cycling 10 times.

Figure 3-7 shows the variation of the 002 peak of carbon fiber D with the charge and discharge process. Movement of the 002 peak is also observed in this case. This indicates that lithium ions intercalate into the interlayer spaces. The concentric texture does not seem to be optimum for intercalation, but the lithium diffusion in the fiber seems to be high enough to overcome the effect of crystal orientation.

It is difficult to say which carbon fiber would be best as an anode from the data of the 1st charge and discharge so cycle testing under more severe conditions was carried out for carbon fibers B, C and D. Figure 3-8 compares the 1st and 30th charge-discharge cycles for each carbon fiber at the current density of 300 μAmg^{-1} which is 10 times larger than that in Fig. 3-4. No large difference is observed among the 1st cycling capacities in three kinds of carbon fibers, which is about 150 $mAhg^{-1}$.

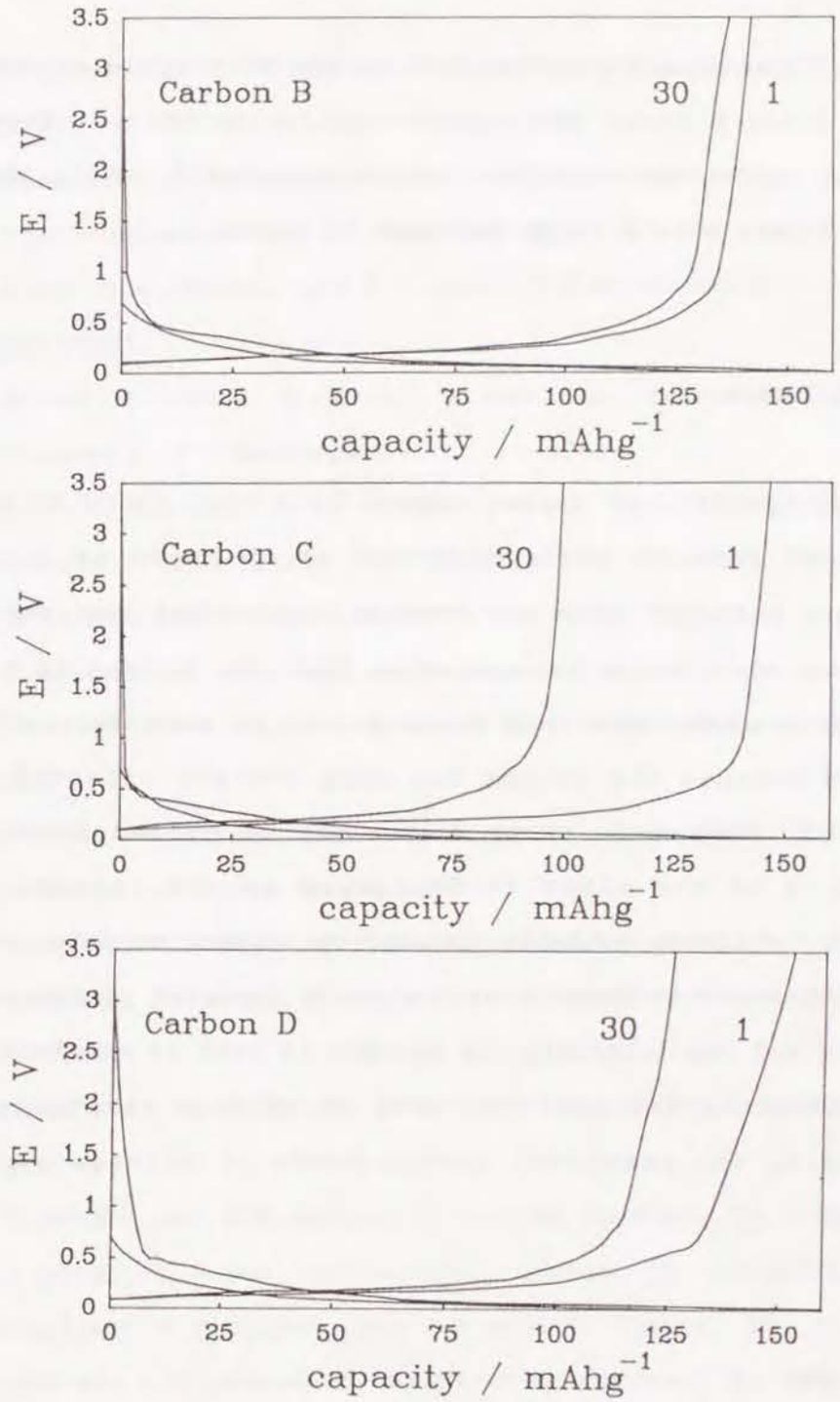

Fig. 3-8 The charge-discharge behaviors of carbon fibers B, C and D at a current density of 300 μAmg^{-1}.

However, the capacity difference by the 30th cycle is apparent. Carbon fiber B shows the highest cycling capacity. Even after the 30th cycle, its capacity loss is only 3.4 %, while the other carbon fibers show a large decrease in capacity.

3.4 Conclusion

The textures of carbon fibers have been found to play an important role in their behavior as an anode of a lithium secondary battery. From our results, the radial texture is more favorable for lithium intercalation than the concentric texture. This makes us believe that fiber A must be more favorable than fiber B because the former has more sharply oriented radial texture. However, fiber A can not be cycled because the structure of the fiber is destroyed in the initial charge process, which is probably induced by solvent co-intercalation. This suggests that fiber A will show an improved performance, if a stable and non-intercalating solvent is used as an electrolyte. It will become important to find an optimal electrolyte for developing the practical carbon anode of lithium secondary battery.

References

1. R.Selim and P.Bro, J.Electrochem.Soc., 121, 1467(1974).

2. F.W.Dampier and S.B.Brummer, Electrochimica Acta, 22, 75 (1977).
3. K.M.Abraham, D.M.Pasquariello, and E.B.Willstaedt, J.Electrochem.Soc., 137, 743(1990).
4. R.Fong, U.v.Sacken, and J.R.Dahn, J.Electrochem.Soc., 137, 2009(1990).
5. R.Kanno, Y.Takeda, S.Ohashi, N.Imanishi, Y.Kawamoto, and O.Yamamoto, J.Electrochem.Soc., in press
6. J.R.Dahn, R.Fong, and M.J.Spoon, Phys. Rev. B, 42,6424(1990).
7. A.Oberlin, "Chemistry and Physics of Carbon", Vol.22, P.A.Thrower Ed., Marcel Dekker, Inc. (1989) p.1.
8. Y.Hishiyama, Y.Kaburagi and M.Inagaki, "Chemistry and Physics of Carbon", Vol.23, P.A.Thrower Ed., Marcel Dekker,Inc. (1991) p.1.
9. T.Iijima, K.Suzuki, and M.Sato, Proc. the 31st Battery Symposium in Japan, Osaka 1990, p.273.
10. M.Inagaki, N.Iwashita, Y.Hishiyama, Y.Kaburagi, A.Yoshida, A.Oberlin, K.Lafdi, S.Bonnamy and Y.Yamada, Tanso, 147, 57(1991).
11. N.Iwashita, Ph.D.Thesis. Hokkaido University, Hokkaido, Japan 1992.
12. C.R.Houska and B.E.Warren, J.Applied Physics, 25, 1503(1954).
13. E.Papirer, E.Guyon, and N.Perol, Carbon, 16, 133(1978).
14. E.Papirer, V.T.Nguyen, and J.B.Donnet, Carbon, 16, 141(1978).
15. M.Oku and K.Hirokawa, J. Electron Spectrosc., 8, 475(1976).
16. M.Arakawa and J.Yamaki, J.Electroanal. Chem., 219, 273(1987).
17. R.Kanno, Y.Takeda, T.Ichikawa, K.Nakanishi, and

O.Yamamoto, J.Power Sources, 26, 535(1989).

18. M.Mohri, N.Yanagisawa, Y.Tajima, H.Tanaka, T.Mitate, S.Nakajima, M.Yoshida, Y.Yoshimoto, T.Suzuki, and H.Wada, J.Power Sources, 26, 545(1989).
19. M.Ide, M.Mizutani, and M.Yamachi, Proc. the 32nd Battery Symposium in Japan, Kyoto 1991, p.147.
20. H.Azuma, A.Omaru, and Y.Nishi, Proc. the 51st Electrochemical Society of Japan Fall Meeting, Nagoya 1991, p.132.

General Conclusion

In this study, the electrochemistry of lithium intercalation compounds as an electrode material for lithium secondary battery has been discussed. Intercalation as a chemical reaction has been well-known in the field of the inorganic chemistry. However, the compounds produced by the electrochemical intercalation are not always the same as those by the chemical reaction. A fundamental study on the mechanism of electrochemical intercalation is very important not only for the development of lithium secondary battery, but also for creating new inorganic compounds.

The results in this study are summarized as follows.

In Chapter 1 of Part I, a lithium diffusion behavior in MoS_2 has been described. A c-axis oriented MoS_2 thin film prepared from CVD method was used to measure a lithium diffusion rate. The diffusion coefficients were calculated from the relation between current and transient time during a potentiostatic discharge. The calculation results are $5.8 \times 10^{-13} cm^2 s^{-1}$ in the range of $3.6 > V > 1.5$ and $5.0 \times 10^{-12} cm^2 s^{-1}$ in the range of $1.2 > V > 0.9$. A drastic change nearly more than 10 times in the diffusion coefficients is observed at around 1.1 V. It has been commonly said that the structure of MoS_2 transforms from 2H to 1T symmetry when more than 0.2 mole% lithium is intercalated. This change in diffusion coefficients is possibly due to the structural transformation. The 1T phase with high diffusivity is more suitable for the cathode than the original 2H phase.

In Chapter 2 of Part I, the structural change of MoS_2 by lithium intercalation has been described. The behavior of the phase transformation of MoS_2 in a reduction process has been compared in three systems; the chemical intercalation system, the electrochemical intercalation systems in PC-DME mixed solvent and in DME solvent. The product from 2H-MoS_2 and n-butyllithium shows 1T-$LiMoS_2$ structure. On the other hand, the products by electrochemical reduction show a largely expanded c-axis by a solvent co-intercalation. The co-intercalated PC molecule decomposes during the reduction process, while the DME molecule is stable and deintercalated with lithium in the charge process. Much lower cycle efficiency in PC-DME than in DME is due to the low stability of a co-intercalated solvent PC.

In Chapter 3 of Part I, FeOCl modified by organic compounds has been discussed as a cathode material. A lot of organic compounds can be easily intercalated into the interlayer space of FeOCl. These modified FeOCl compounds show reversible lithium intercalation, while the bare FeOCl decomposes by the lithium intercalation. The charge-discharge behavior of the modified FeOCl depends on the kind of the used organic solvents. It is indicated that the stability of the modified FeOCl depends on the basicity of the intercalated organic compound. 4-aminopyridine, pyridine, and 2-vinylpyridine are sufficiently basic to stabilize its structure during discharge.

In Chapter 4 of Part I, the defect thiospinel compounds, $Cu_xM_2S_4$(M=Ti, Cr) have been discussed. $Cu_{0.18}Ti_2S_4$ prepared by the oxidation of $CuTi_2S_4$, shows a good reversibility with the

smooth lithium intercalation. Under the cycling at the current density of 1 $mAcm^{-2}$, the discharge capacity of the 1st cycle is about 170 $mAhg^{-1}$, which corresponds to $Li_{1.5}Cu_{0.18}Ti_2S_4$. On the other hand, the defect $Cu_xCr_2S_4$ can not be prepared by the chemical oxidation method. Then $Li_xCu_{1-y}Cr_2S_4$ is prepared by the reaction of $CuCr_2S_4$ and n-butyllithium. In this case, the reduced copper metal deposits on the surface of the compound. This material does not show the reversible electrode reaction. The XRD measurements indicates that the copper metal returns to the 8a sites of the spinel framework in the charge process. This copper atom prevents from the lithium diffusion via 16c and 8a sites. New methods to remove copper ions are required in order to discuss other thiospinel compounds.

In Chapter 5 of Part I, structural characteristics and electrochemical behavior of the brannerite-type $CuV_{2-x}Mo_xO_6$ ($0<x<1$) have been studied. These compounds incorporate Li^+ by expelling copper metal from the lattice on discharge. The good rechargeability of lithium ions in copper brannerite electrodes is due to the tendency of the copper ions in the structure to be easily deintercalated and intercalated. Li/$CuV_{2-x}Mo_xO_6$ cell could be cycled over 50 times at 0.8 $mAcm^{-2}$ between 2.0 and 3.5 V. However, after many cycles, the cathode material can no longer intercalate copper easily, the deposited copper may possibly slowly cause serious problems for the practical use as the electrode for lithium battery.

In Chapter 1 of Part II, various carbon materials as anode have been studied. Among them the carbon fiber M46 shows the

highest rechargeable intercalation and restrains the occurrence of lithium dendrites. Over 170 cycles are possible when the M46 carbon-lithium composite anode is used in a coin type cell. Whereas with a bare lithium metal anode, only 80 cycles are observed. However, carbon materials including M46 commonly show irreversible capacity at the initial cycle, which depends on the specific surface area. Electrolyte solvents possibly decompose on the surface of the carbon materials during the first charge process.

In Chapter 2 of Part II, the detailed mechanism lithium intercalation into M46 carbon fiber has been described. The intercalation is highly reversible, but in the first charge, the formation of a passivating film is found on the carbon surfaces. The c-axis expansion varies with the solvent composition, and which suggests the solvent co-intercalation. The reaction mechanism during the first discharge is quite complicated and depends on the electrolyte, discharge current densities and also type of carbon fibers employed.

In Chapter 3 of Part II, the effect of carbon-texture in pitch-based carbon fiber has been described. The carbon fiber having the radial texture shows good reversibility under a high current density. The concentric texture shows less reversibility than the radial texture. However, the most strongly oriented radial texture shows an irreversible behavior because electrolyte solvents decompose on the edge of the carbon crystal. The sub-product by the decomposition induces the destruction of the carbon texture. It is important to select the best combination

of less reactive solvent and carbon materials with high mechanical strength.

From all the results, it is concluded that some layered materials have a possibility of being used as an electrode material for lithium secondary battery. The diffusion rate of intercalated species are generally high compared to the diffusion in a fixed framework structure. However, at the same time, layered materials have a tendency to be destructed after many cycles as shown in MoS_2, FeOCl, brannerite, and carbon fibers. This is due to the large structural change induced by the lithium or solvent intercalation. Thus, in future, it will become important to design the electrode system being prevented from the solvent co-intercalation and/or find compounds having three dimensional framework structure with high lithium diffusivity.

Acknowledgement

This thesis deals with the research on the lithium insertion compounds as electrode materials of lithium secondary battery. The work has been carried out at Kyoto University under the direction of Professor Zen-ichiro Takehara, and at Mie University under the direction of Professor Osamu Yamamoto.

The author is especially indebted to Professor Zen-ichiro Takehara and Professor Osamu Yamamoto for their valuable suggestions and continuing supervising throughout this work.

The author also wishes to express his thanks to Professor Naohiro Soga, Professor Zempachi Ogumi and Associate Professor Yasuo Takeda for their helpful comments and discussions.

Thanks are also expressed to Assistant Professor Kiyoshi Kanamura and Assistant Professor Yoshiharu Uchimoto for their kind direction and encouragement in accomplishing this work.

I am also grateful to Associate Professor Ryoji Kanno who helped me especially to start the study on the carbon anode at Mie University and to Professor Michio Inagaki at Hokkaido University who kindly offered me unique carbon materials and, in addition, useful informations on carbon chemistry.

Finally, the author would like to appreciate all the members of Professor Takehara's Laboratory and Professor Yamamoto's Laboratory for their excellent contributions to this work.

Tsu, October 1992

Nobuyuki Imanishi

Department of Chemistry
Faculty of Engineering
Mie University